POLITECNICO
MILANO 1863

SCUOLA DI INGEGNERIA INDUSTRIALE
E DELL'INFORMAZIONE

Design of Trajectories from Low Lunar Orbits to Halo: The LUMIO Case

Tesi di Laurea Magistrale in
Space Engineering - Ingegneria Spaziale

Author: **Mattia Piraccini**

Student ID: 244717
Advisor: Prof. Francesco Topputo
Co-advisors: Dr. Carmine Giordano, Alessandro Martinelli
Academic Year: 2024-25

Abstract

In recent years there has been a renewed interest in developing manned and unmanned missions targeting the cislunar region. To ensure the safety of those operation, it is essential to develop more accurate models of the flux of material constantly entering the Earth–Moon system. Within this context, the LUMIO CubeSat mission aims to detect the impacts of meteoroids on the lunar far side to refine the existing models constructed on Earth based observations, thus increasing lunar situational awareness. To gather these data, the spacecraft is going to be injected into a quasi–halo orbit about the L_2 point in the Earth–Moon system, where the science observations will take place. In this thesis a transfer trajectory is designed for the LUMIO mission from an highly elliptical lunar parking orbit to the selected operational orbit. Due to the CubeSat limited Δv budget and thrust authority, an extensive trajectory optimization is performed to minimize the cost of the deterministic maneuvers. This problem is transcribed into a multiple–burn multiple–shooting formulation, assuming impulsive maneuvers at the boundary of each arc. To remove the singularities in the derivatives of a fuel–optimal problem, a set of regularized variables are introduced based on the Kustaanheimo–Stiefel transformation, reducing unnecessary impulses to negligible values. Initially, these trajectories are sought in the Circular Restricted Three Body Problem (CRTBP) to leverage the existence of stable manifold structures and periodic orbits. These transfers are transitioned in the Restricted n–Body Problem defined in the Earth–Moon Roto–Pulsating Frame (RnBP–RPF) by gradually increasing the model complexity through a series of refinement steps. A total of 40 solutions have been computed, with three meeting the mission requirements, demonstrating the feasibility of this transfer design. The total cost of the compliant trajectories is a small percentage of the overall budget ($25.62-41\%$), leaving large margins for Station Keeping (SK) and Navigation Maneuvers. These solutions are then validated outside the solver environment applying only impulses above a minimum threshold of 5 mm/s. Additionally, an eclipse analysis combined with a conjunction and opposition detection is carried out to assess the feasibility of the most promising transfers.

Keywords: LUMIO, Trajectory Optimization, Regularized Variables, High–Fidelity Models, RnBP–RPF, Lunar Parking Orbit, Quasi–Halo Orbit

Sommario

In tempi recenti si è rinnovato l'interesse nello sviluppo di missioni spaziali con e senza equipaggio dirette verso la regione cislunare. Diventa essenziale sviluppare modelli accurati sul flusso di materiali che entrano costantemente nel sistema Terra–Luna per assicurare la sicurezza di tali operazioni. In questo contesto la missione CubeSat LUMIO si pone l'obbiettivo di osservare impatti di meteoroidi sul lato nascosto della Luna per rifinire modelli esistenti basati su osservazioni condotte a terra, incrementando il lunar situational awareness. Per ottenere queste misurazioni il satellite sarà posizionato in un'orbita quasi–halo attorno il punto L_2 del sistema Terra–Luna, dove le ricerche scientifiche verranno condotte. Nel corso di questa tesi le traiettorie di trasferimento della missione LUMIO sono progettate a partire da orbite di parcheggio lunari altamente ellittitiche fino all'orbita operativa. A causa del limitato budget in termini di Δv e della ridotta capacità propulsiva del CubeSat, viene condotta una robusta campagna di ottimizzazione della traiettoria per minimizzare il costo delle manovre deterministiche. Il problema viene transcritto in una formulazione multiple–burn multiple–shooting, assumendo manovre impulsive al termine di ciascun arco. Per rimuovere le singolarità presenti nelle derivate di una ottimizzazione del propellente, sono introdotte delle variabili regolarizzate basate sulla transformazione di Kustaanheimo–Stiefel, riducendo gli impulsi non necessari a valori trascurabili. Intiazialmente, le traiettorie sono ricercate nel Problema dei Tre Corpi Circolare Ristretto per sfruttare l'esistenza di manifold e orbite periodiche. Questi trasferimenti sono riportati nel Problema Ristretto degli n–Corpi definito nel sistema di riferimento Roto–Pulsante Terra–Luna, aumentado gradualmente la complessità del problema tramite una serie di step intermedi. Un totale di 40 soluzioni è stato determinato, di cui tre rispettano i vincoli di missione, dimostrando la possibilità di attuare questo trasferimento. Il costo complessivo delle triettorie conformi è una piccola frazione del budget $(25.62 - 41\%)$, lasciando ampi margini per manovre di mantenimento orbitale e di navigazione. Una successiva validazione è attuata su queste soluzioni al di fuori del solver, applicando solo manovre al di sopra di un limite minimo di 5 mm/s. Infine, le condizioni di eclisse, congiunzione e opposizione sono analizzate per verificare la fattibilità dei trasferimenti.

Parole chiave: LUMIO, Ottimizzazione di Traiettorie, Variabili Regolarizzate, Modelli ad Alta Fedeltà, RnBP–RPF, Orbita di Parcheggio Lunare , Orbita Quasi–Halo

Contents

1 | Introduction

1.1. Context

Throughout the recorded history, the night sky has always captured the imagination of men and it has inspired many great minds to pursue studies to unravel the laws ruling the motion of those objects. Gradually, as the technical means of observation advanced through the development of optics and lenses, knowledge improved and the mysticism surrounding those distant worlds faded. This is especially the case for Earth's natural satellite. Nonetheless, the Moon retained part of its symbolic significance, still being perceived as an unreachable and distant world.

This idea helped making space into one of the last frontiers of exploration in the twentieth century. As a result, the Apollo program brought humans onto the surface of the Moon for the first time with the Apollo 11 on July 20^{th} 1969. What was considered to be just a dream few decades earlier became a series of successful missions, bringing a total of twelve astronauts to the lunar surface. However, this golden age of human exploration on the Moon quickly came to an end with the Apollo 17 in 1972.

Recently, there has been a renewed interest in the possibility of reviving a manned program to the lunar surface. Thus, the Artemis program [9] was born with the purpose of bringing back humans on the Moon for the first time since the Apollo program and building long–term infrastructure both in orbit and on the surface. Moreover, the idea of placing a space station orbiting the Moon and providing logistic benefits for future missions led to the development of the Lunar Gateway project [17].

Consequently, the allocation of considerable funding to these large programs made both dedicated and non–dedicated launch opportunities to the cislunar region more affordable, particularly for missions dealing with limited resources. The Artemis program and the Gateway project acted as catalysts sparking interest in the cislunar space, thus increasing the number of planned and launched missions targeting the region. A similar trend holds true even for CubeSat missions, that have demonstrated the capability to operate successfully far from Earth in complex dynamical environments [18, 19].

As the number of manned and unmanned missions directed to the Moon is going to increase in the near future, it becomes important to refine the current meteoroid models in the cislunar environment and to initiate a lunar situation awareness program. Within this context, the LUMIO mission [8] aims to detect impacts of meteoroids on the far side of the Moon to couple these data with the currently available Earth–based lunar observations. This CubeSat mission has already entered Phase C in the design process and it will perform measurements that were not achievable in the past, thus helping to refine the estimates of the flux of material constantly bombarding the Earth–Moon system. In addition, it will demonstrate capabilities of autonomous operations in the highly–nonlinear cislunar environment.

Like other CubeSats, LUMIO has limited thrust authority coupled with a strict Δv budget. Therefore, it becomes essential to perform an extensive trajectory optimization campaign to minimize the fuel cost in the different phases of the mission. This is achieved by leveraging the sensitivity to initial conditions in high–fidelity models. In particular, the majority of the cost in terms of Δv depends on the transfer trajectory design. During this phase, the CubeSat shall reach the target operational orbit, which is a quasi–halo about the L_2 point in the Earth–Moon system. After the CubeSat is released by the mothercraft, a series of Deep Space Maneuvers are exploited to steer its trajectory.

1.2. Research question

The subject of this thesis fits into the context of trajectory optimization, which is vastly discussed in literature. The aim is to determine an alternative fuel–optimal transfer for the LUMIO mission, considering a set of different initial condition from the latest development phase [21].

In this thesis, the possibility to determine the transfer from a lunar parking orbit is reconsidered. This was a concept studied in earlier stages of the mission development [7]. With respect to previous studies, more elongated parking orbits are considered coupled with high–fidelity models, leading to a potential reduction in terms of required Δv.

The optimization of the transfer trajectory is transcribed in a Nonlinear Programming (NLP) problem [4], which is solved with numerical techniques exploiting the analytical form of Jacobian matrices related to the objective function and to the constraints. Initially, free transport mechanisms offered by the stable invariant manifold are exploited to determine trajectories in the CRTBP. Then a successive refinement approach is adopted to determine solutions in high–fidelity models.

Moreover, this research is important to determine possible variations in the transfer design, which could provide greater flexibility in case the nominal solution cannot be actuated due to external factors.

Therefore, the research question can be summarized as:

> To what extent can transfer trajectories from lunar parking orbits to the LUMIO quasi–halo orbit be designed within the Δv budget allocated in Phase C?

1.3. Thesis overview

In the following, a brief overview on the thesis structure is reported.

- Chapter 1: The first chapters serves as an introduction to the thesis and introduces the research question which guides the entire thesis work.
- Chapter 2: This chapter is dedicated to the introduction of the LUMIO mission and its design. An overview on the current mission analysis is reported to draw similarities with the work carried out in the following chapters. Additionally, a few notable mission constraint are presented and justified.
- Chapter 3: In this chapter the dynamical models adopted in the trajectory optimization are described. The variational equations complete the set of the equations of motion, thus introducing an analytic method to compute the State Transition Matrix (STM). Moreover, periodic solutions in the CRTBP are introduced along with a technique to evaluate their counterparts in higher fidelity models.
- Chapter 4: This chapter introduces the methodology required to define the trajectory optimization problem in the CRTBP. Moreover, the determination of good initial candidates is presented.
- Chapter 5: Within this chapter a successive refinement process is introduced to determine optimized transfer trajectories in higher–fidelity models.
- Chapter 6: In this chapter the results are analyzed and the solutions compliant to the mission requirements are presented.
- Chapter 7: The last chapter serves as the conclusion of the thesis. It contains a brief summary of the work carried out in the previous chapters with suggestions to possible future developments.

2 | Overview of the LUMIO mission

The Lunar Meteoroid Impact Observer (LUMIO) is a CubeSat mission, currently in Phase C of the design process. This mission concept was submitted to Esa's SynNova Competition and then awarded funding by different ESA programs.

LUMIO aims to detect flashes in the visible spectrum produced by impacts of meteoroids on the far side of the Moon, with an optical payload named LUMIO–Cam. This becomes essential to better characterize this flux of material in the cislunar environment to ensure the safety of manned and unmanned missions. Currently, the best estimates are provided by Earth–based observations of the Lunar surface, which are limited by geometrical conditions determining the illumination of the near side facing the Earth. Moreover, the atmosphere interferes with the detection, thus limiting the energy range of the observable events. Within this context, the LUMIO mission offers the opportunity to detect impacts on the far side of the Moon, thus completing the Earth–based observation.

In the current mission design [21], LUMIO is going to be launched in a rideshare configuration with a mothercraft to reduce the expenses and due to the limited propulsion capabilities of CubeSats. The carrier will inject LUMIO into a Weak Stability Boundary (WSB) transfer towards the Moon. Afterwards, the CubeSat is going to be released, starting the commissioning phase of all subsystems. A series of Deep Space Maneuvers (DSM) will take place to determine a transfer trajectory towards the operational orbit. The latter is selected to be a halo orbit about the L_2 point in the Earth–Moon system. The operative phase is expected to last 1 year divided in alternating Science and Navigation&Engineering cycles. Lastly, the CubeSat will be decommissioned by performing a maneuver that will inject the spacecraft in a collision course with the Moon. A graphical representation of the mission phases is reported in Figure 2.1.

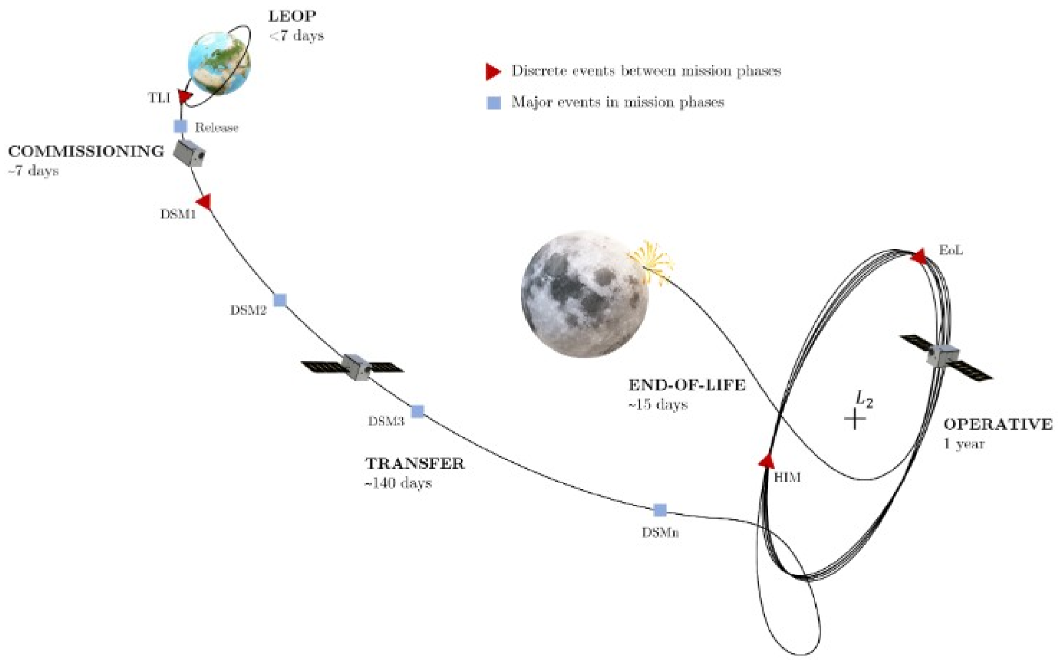

Figure 2.1: LUMIO reference mission reported in [21]

2.1. Mission Analysis

2.1.1. Operational Orbit

LUMIO's target orbit is a halo about the L_2 point in Earth–Moon system, characterized by a Jacobi constant $C_j = 3.09$. This periodic solution was selected after a careful trade off process in Phase 0 [8]. The halo orbit is part of the southern family and it is fully defined by the Jacobi constant and the the out–of–plane amplitude A_z:

	C_j [-]	A_z [km]
Target halo	3.09	28418.41

Table 2.1: Parameters of the operational orbit

A spacecraft located on this operational orbit is able to constantly monitor the far side of the Moon without losing direct sight of Earth for communication purposes. Moreover, this periodic orbit was determined to be accessible with a moderate Δv from an eventual lunar parking orbit. This was an initial concept for the transfer trajectory investigated in Phase A [7], which is expanded upon in the course of this thesis.

2.1.2. Transfer Design

In Phase B the transfer trajectory was computed as a 2 layer problem [21]. The first layer determines the trajectory of the mothercraft which is assumed to be injected into a WSB transfer towards a Low Lunar Orbit (LLO), as a CLPS[1] mission. The second layer models the trajectory of the CubeSat, which detaches from the carrier and performs a series of DSMs to reach the target quasi–halo. These steps are solved with a direct optimization process with a fuel optimal formulation.

It is worth noting the successive refinement steps utilized to determine the second layer. In particular, the Restricted n–Body Problem expressed in a Roto–Pulsating Reference Frame (RnBP–RPF) was employed to propagate the transfer trajectories in the following steps [13]:

- A first trajectory is optimized considering the target halo in the CRTBP.
- A quasi–halo is determined based on the optimized insertion point determined at the previous step.
- A final optimization is carried out using the solution at step 1 as initial guess and considering the quasi–halo as final target.

A similar approach is adopted in this thesis during the refinement process in higher fidelity models, as described in Chapter 5. However, some assumptions differ from this transfer design starting from the release conditions. In fact, the spacecraft is assumed to be injected into an elliptical lunar orbit, as investigated in Phase A. A more comprehensive description is reported in Chapter 4 and 5, where the methodology adopted to model the transfer is introduced in greater detail.

2.1.3. Key Requirements

In this section the mission requirements included in the trajectory optimization are introduced. The compliance to the limitations imposed on the Δv budget are going to be verified a posteriori. Whereas, the minimum time of flight related to different phases of the trajectory is employed as an active constraint in the optimization problem. In the following table a few notable requirements are listed along with a simplified rationale:

[1]The Commercial Lunar Payload Services (CLPS) initiative offers the opportunity to acquire delivery services from private contractors to send payloads towards the Moon.

Title	Rationale	Value
Δv Budget	This budget was defined in the Mission Analysis Report (MAR) written at the end of Phase B	80 m/s
Max impulsive maneuver	This limit is imposed to ease a finite impulse mapping that shall be considered in a future refinement	30 m/s
Min impulsive maneuver	This limit derives from the propulsion system which is able to provide this minimum velocity variation	5 mm/s
Min time between maneuvers	This constraint is imposed to allocate the time slot necessary to conduct an Orbit Determination phase and a potential Trajectory Correction Maneuver	3 d
Min duration of the parking orbit	This limit is imposed to allow the commissioning of all subsystems, assuming LUMIO to be directly released into a lunar parking orbit	7 d

Table 2.2: Mission constraints and rationale

3 | Dynamical Models

This chapter will serve as an introduction to the dynamical models adopted in this thesis. The selection of a suitable model is essential to achieve an accurate representation of the physical problem. As the research question requires to determine a transfer trajectory in the cislunar environment, the Two Body Problem in not sufficient to precisely compute the motion of a spacecraft. Therefore, it is necessary to investigate more complex frameworks, thus introducing a larger number of primary bodies and additional forces. Since the mass of the spacecraft is several orders of magnitude lower compared to the other celestial bodies, it is sufficient to adopt restricted formulations. The motion of all the main bodies of the solar system is described by the ephemerides, retrieved using the SPICE toolkit [1, 2].

A logical next step in the refinement of the model is to introduce a third body, as in the Circular Restricted Three Body Problem (CRTBP). This formulation can be further expanded considering an arbitrary number of gravitational sources and by dropping other assumptions, as in the RnBP–RPF. Lastly, a variation of the RnBP is obtained by shifting the origin of the system from the SSB to the center of one massive body, obtaining an inertial planeto–centered version [3]. In the following sections, these three models are presented.

3.1. Circular Restricted Three–Body Problem

The Circular Restricted Three–Body Problem (CRTBP) is a well–known model in astrodynamics, with its first formulation dating back to Euler. It has been extensively investigated over the past century, leading to the development of innovative mission designs exploiting the dynamics near the equilibrium points admitted by such formulation. Several missions leveraged the observational benefits offered by the periodic solutions about these points: ISEE–3 [15] was the first one to exploit a halo orbit, since then many others followed like SOHO [22] and LISA–Pathfinder [29].

The CRTPB was developed to model the motion of a third body, having negligible mass, subject to the gravitational field generated by two massive bodies, called primaries. The primaries, labeled as P_1 and P_2 and of mass m_1 and m_2, are assumed to move on coplanar circular orbits about a common center of mass under the influence of their mutual attraction. Within this frame, the main bodies are located at a fixed distance d, revolving with a constant mean motion n with respect to the centroid.

In fact, the mass of the third object m is considered so small that it does not affect the dynamics of the primaries. Therefore, the restricted problem provides a suitable approximation of the motion of a satellite in the Earth–Moon system.

The equation of motion are often expressed in the synodic reference frame to obtain an autonomous system and to infer the qualitative features of the model. The origin is set to be coincident with the system's barycenter. The x–axis is directed from the larger primary towards the smaller one and the z–axis is aligned with the angular velocity vector $\boldsymbol{\omega}$. Consequently, the y–axis is defined as the missing unit vector required to complete the right–handed frame.

Then, the equations of motion of the third body in the rotating frame are [31]:

$$\ddot{\mathbf{R}} + 2\boldsymbol{\omega} \times \dot{\mathbf{R}} + \boldsymbol{\omega} \times (\boldsymbol{\omega} \times \dot{\mathbf{R}}) = -G\frac{\mathbf{R} - \mathbf{R_1}}{||\mathbf{R} - \mathbf{R_1}||} - G\frac{\mathbf{R} - \mathbf{R_2}}{||\mathbf{R} - \mathbf{R_2}||} \tag{3.1}$$

where $\mathbf{R}$ is the position of the massless particle, $\mathbf{R_1}$ and $\mathbf{R_2}$ are the positions of the primaries assumed as point masses. Moreover, Newton's notation is adopted to represent the derivatives with respect to dimensional time.

3.1.1. Nondimensional CRTBP

The equations can be simplified introducing a mass parameter defined as:

$$\mu = \frac{m}{m_1 + m_2} \tag{3.2}$$

Additionally, the distance between the primaries, their angular speed and the sum of their masses are set to a unitary value. In the rotating frame, the position and mass of the primaries can be expressed as a function of μ, as reported in Eq. (3.3).

$$\begin{aligned} \mathbf{P}_1 &= [-\mu, 0, 0]^T \qquad & m_1 &= 1 - \mu \\ \mathbf{P}_2 &= [1 - \mu, 0, 0]^T \qquad & m_2 &= \mu \end{aligned} \tag{3.3}$$

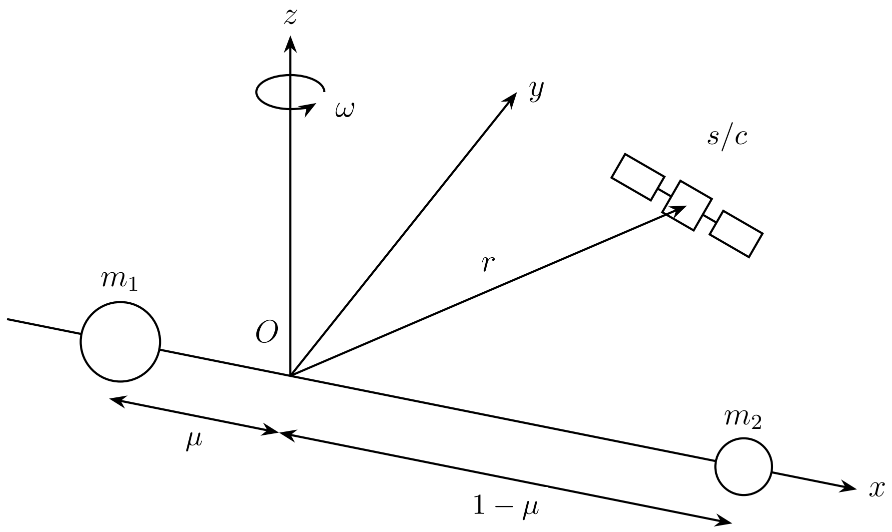

Figure 3.1: CRTBP in the nondimensional rotating frame

Therefore, the final nondimensional form of the equations can be derived as a function depending only on the mass parameter [31]:

$$\ddot{x} = +2\dot{y} + \frac{\partial \Omega}{\partial x} \tag{3.4a}$$

$$\ddot{y} = -2\dot{x} + \frac{\partial \Omega}{\partial y} \tag{3.4b}$$

$$\ddot{z} = +\frac{\partial \Omega}{\partial z} \tag{3.4c}$$

where Ω is the pseudo–potential expressed as:

$$\Omega(x,y,z) = \frac{1}{2}(x^2+y^2) + \frac{1-\mu}{r_1} + \frac{\mu}{r_2} + \frac{1}{2}\mu(1-\mu) \tag{3.5}$$

with r_1 and r_2 being the distance of the third body from the primaries:

$$\begin{aligned} r_1 &= \sqrt{(x+\mu)^2+y^2+z^2} \\ r_2 &= \sqrt{(x+\mu-1)^2+y^2+z^2} \end{aligned} \tag{3.6}$$

The set of nondimensional Equations (3.4) can be written as a system of first order ODE by simply expressing the accelerations as the time derivative of the velocity components. These, in turn, are defined as the time derivative of the position coordinates of the third body, highlighting the dependence on the state vector $\mathbf{x} = [x, y, z, v_x, v_y, v_z]^T$.

Then, the canonical form of the equation of motion expressed in the synodic frame is obtained:

$$\begin{cases} \dot{x} = v_x \\ \dot{y} = v_y \\ \dot{z} = v_z \\ \dot{v}_x = 2v_y + x - (1-\mu)\,\dfrac{x+\mu}{r_1^3} - \mu\,\dfrac{x+\mu-1}{r_2^3} \\ \dot{v}_y = -2v_x + y - (1-\mu)\,\dfrac{y}{r_1^3} - \mu\,\dfrac{y}{r_2^3} \\ \dot{v}_z = -(1-\mu)\,\dfrac{z}{r_1^3} - \mu\,\dfrac{z}{r_2^3} \end{cases} \tag{3.7}$$

or expressed in a more compact form

$$\dot{\mathbf{x}} = \boldsymbol{f}(\mathbf{x}) \tag{3.8}$$

It is worth noting that Eq. (3.7) represents an autonomous system, since it has no explicit time dependence.

3.1.2. State Transition Matrix of the CRTBP

The State Transition Matrix (STM) is commonly used in direct optimization methods to estimate the response of the system at variations in the initial conditions and to increase computational efficiency. This method relies on the linearization of the flow φ to compute possible trajectories close to the reference one. Given the importance of this mathematical tool, a brief background is considered to be necessary to understand its role in the next chapters.

Let $\mathbf{x}$ be the solution of the equation of motion at a given time t:

$$\mathbf{x} = \varphi(\mathbf{x_0}, t_0; t) \tag{3.9}$$

where φ is the flow, an operator mapping the initial state space vector into its counterpart at time t. Since the CRTPB has no closed form solution, φ is computed with numerical integrators. Then, it is possible to define a perturbed solution generated by an initial displacement $\delta\mathbf{x_0}$ as:

$$\mathbf{x} + \delta\mathbf{x} = \varphi(\mathbf{x_0} + \delta\mathbf{x_0}, t_0; t) \tag{3.10}$$

By considering the first–order Taylor expansion of the flow with respect to the initial displacement $\delta\mathbf{x_0}$ about the reference state $\mathbf{x_0}$, the following relation can be derived:

$$\varphi(\mathbf{x_0} + \delta\mathbf{x_0}, t_0; t) = \varphi(\mathbf{x_0}, t_0; t) + \frac{\partial\varphi}{\partial\mathbf{x_0}}(\mathbf{x_0}, t_0; t)\delta\mathbf{x_0} + o(\delta\mathbf{x_0}) \tag{3.11}$$

This equation can be simplified by substituting terms from Eqs. (3.9) and (3.10), and by neglecting higher order terms $o(\delta\mathbf{x_0})$:

$$\delta\mathbf{x} = \frac{\partial\varphi}{\partial\mathbf{x_0}}(\mathbf{x_0}, t_0; t)\delta\mathbf{x_0} \tag{3.12}$$

However, this is still an approximation of the displacement at time t, affected by an error. This can be contained by avoiding large initial displacements, long term propagation and highly non–linear dynamics. Within this formulation, the STM Φ is defined as:

$$\Phi(\mathbf{x_0}, t_0; t) \equiv \frac{\partial\varphi}{\partial\mathbf{x_0}}(\mathbf{x_0}, t_0; t) \tag{3.13}$$

At this point, the problem is to compute an accurate STM. It can be determined with finite differences or exploiting the variational approach. The latter will be used in this thesis, as it reduces significantly the computation time while increasing the precision, being an analytic method.

The processes involved in finding the variational equations is similar to the one applied to define the STM. A first order Taylor Series Expansion (TSE) of the equation of motion $\boldsymbol{f}(\mathbf{x})$ is computed about the reference trajectory. After some intermediate steps, it is possible to write the dynamics of the STM according to the following system of equations, known as variational equations:

$$\begin{cases} \dot{\Phi}(t_0, t) = A(t)\Phi(t_0, t) \\ \Phi(t_0, t_0) = \mathbb{I}_{6x6} \end{cases} \tag{3.14}$$

where $\mathbb{I}_{6x6}$ is the 6×6 identity matrix and A is the Jacobian of the dynamics about the reference trajectory $\mathbf{x}^*$

$$A(t) = \left.\frac{\partial\boldsymbol{f}(\mathbf{x}, t)}{\partial\mathbf{x}}\right|_{\mathbf{x}=\mathbf{x}^*} \tag{3.15}$$

In the case of the CRTBP, the matrix A is:

$$A(t) = \begin{bmatrix} A_{rr} & A_{rv} \\ A_{vr} & A_{vv} \end{bmatrix} \tag{3.16}$$

with

$$A_{rr} = \mathbf{0}_{3x3}, \quad A_{rv} = \mathbb{I}_{3x3}, \quad A_{vr} = \begin{bmatrix} \Omega_{/xx} & \Omega_{/xy} & \Omega_{/xz} \\ \Omega_{/yx} & \Omega_{/yy} & \Omega_{/yz} \\ \Omega_{/zx} & \Omega_{/zy} & \Omega_{/zz} \end{bmatrix}, \quad A_{vv} = \begin{bmatrix} 0 & 2 & 0 \\ -2 & 0 & 0 \\ 0 & 0 & 0 \end{bmatrix} \tag{3.17}$$

The resulting variational equations have to be integrated along with Eq. (3.7), creating a system of 42 first order ODEs.

3.1.3. Integral of Motion and Solutions

The CRTPB expressed in the synodic frame admits an integral of motion, known as Jacobi constant C_j:

$$C_j(x, y, z, v_x, x_y, v_z) = 2\Omega(x, y, z) - v^2 \tag{3.18}$$

where v is norm of the velocity vector. As a result, an important inequality condition can be stated:

$$\Omega(x, y, z) \geq C_j/2 \quad \text{since} \quad v^2 \geq 0 \tag{3.19}$$

This inequality can be used to differentiate between the allowed regions, where Eq. (3.19) is satisfied, and forbidden regions, where it is not. In fact, the integral of motion is directly proportional to the mechanical energy of the system per unit mass E, under the assumption of no external action. The larger the C_j the lower the energy associated with the third body.

$$E = -2C_j \tag{3.20}$$

In absence of maneuvers and other external perturbations, the mechanical energy is conserved and, as a result, the Jacobi constant. This property can be utilized in a differential correction scheme aimed at finding periodic and non–periodic solutions about the equilibrium points.

Equilibrium points

The CRTPB admits five equilibrium points, also denoted as Lagrange points or Libration points of the system. The Lagrange points L_i are determined by solving a zero–finding problem applied to the set of nondimensional equations of motion, expressed in canonical form in the rotating reference frame (Eq. 3.8). The only condition which satisfies the last equation is $z = 0$. Therefore, all the equilibrium points are located on the xy–plane of the synodic frame. They are split in two groups: the Collinear points and the Triangular points.

The collinear points (L_1, L_2, L_3) are located on the x–axis and they can be computed reducing the zero–finding problem to a simplified scalar form, as reported in Eq. (3.21).

$$g(x) = x - (1-\mu)\frac{x+\mu}{|x+\mu|^3} - \mu\frac{x+\mu-1}{|x+\mu-1|^3} = 0 \tag{3.21}$$

The triangular points (L_4, L_5) can be computed geometrically at the intersection of two circles of unitary radius centered in the primaries.

$$\mathbf{L}_4 = \left[0.5-\mu, \frac{\sqrt{3}}{2}, 0\right]^T \qquad \mathbf{L}_5 = \left[0.5-\mu, -\frac{\sqrt{3}}{2}, 0\right]^T \tag{3.22}$$

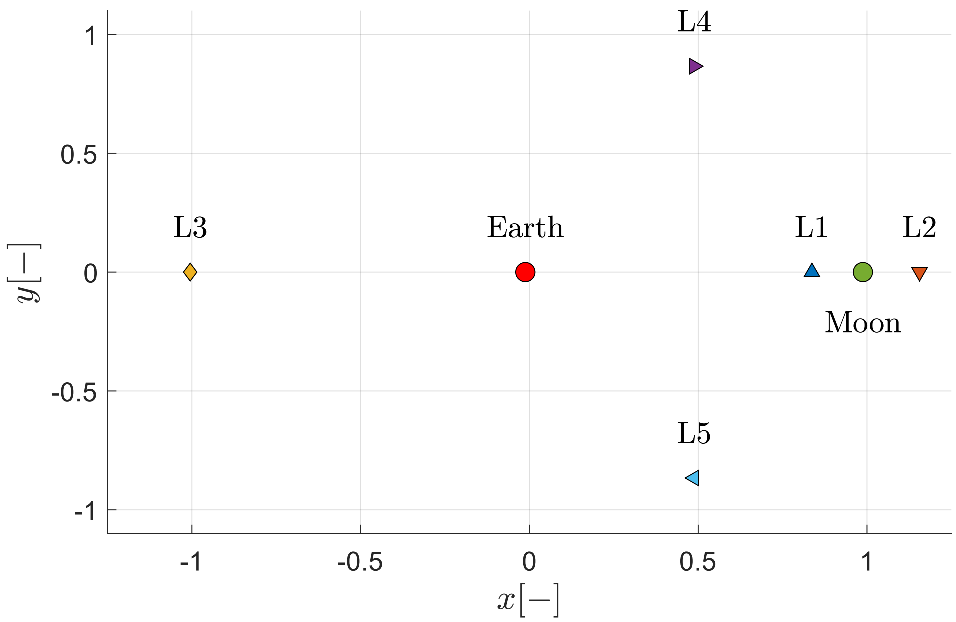

Figure 3.2: Graphical representation of the Lagrange points in the Earth–Moon system

Solutions about the Collinear points

The solutions of the equation of motion near the Lagrange points can be introduced through the stability analysis of the equilibrium points. In particular, an equilibrium point is considered stable if the trajectory of a small body with no initial velocity remains bounded in a region near the libration point, after a small initial displacement is applied.

In practical terms, the stability is determined by analyzing the linearized set of equations of motion about the Lagrange points, neglecting the higher order terms [31]:

$$\ddot{x}' - 2\dot{y}' - x'\Omega_{xx} - y'\Omega_{xy} = 0 \tag{3.23a}$$

$$\ddot{y}' + 2\dot{x}' - x'\Omega_{xy} - y'\Omega_{yy} = 0 \tag{3.23b}$$

$$\ddot{z}' - z'\Omega_{zz} = 0 \tag{3.23c}$$

where the notation ($'$) is used to denote the displacement of such coordinate from the corresponding value at the libration point. Equation (3.23c) is uncoupled from the other two and it describes an undamped harmonic motion along the z direction. Therefore, the motion along the z direction is always stable for all libration points.

Thus, the overall stability depends on the Eqs. (3.23a) and (3.23b). The obtained characteristic equation (Eq. 3.24) admits four complex roots, corresponding to the eigenvalues of the linearized reduced system.

$$\lambda^4 + (4 - \Omega_{/xx} - \Omega_{/yy})\lambda^2 + \Omega_{/xx}\Omega_{/yy} - \Omega^2_{/xy} = 0 \tag{3.24}$$

Regarding the collinear points, it is possible to prove that one of the characteristic roots has a positive real part, leading to an unstable equilibrium condition. Whereas, the triangular points are stable, if the mass coefficient is $\mu < 0.03852$. This is valid in the case of the Earth–Moon system.

Based on the linearized solution of Eq. (3.23), it is possible to determine families of periodic and quasi–periodic orbits about the collinear points [23]:

- Lyapunov orbits are planar orbits contained in the synodic plane or in a vertical plane. They describe an elliptic motion around the libration points, which is progressively deformed as the dimension of the orbit increases.
- Lissajous orbits are tridimensional quasi–periodic orbits which do not repeat after each revolution. This trajectories can be explained as the superposition of the

motion on xy–plane and z–direction having different frequencies [24].

- Halo orbits are spatial periodic solutions which bifurcate from the planar Lyapunov orbits. This family can be obtained by introducing higher order terms in the approximation of the dynamics to achieve matching frequencies of the in plane and out of plane motion [30].

As mentioned in Chapter 2, the operational orbit of the LUMIO mission is a halo around Earth–Moon L_2 point. Therefore, a simple differential method is developed to compute precisely the target orbit.

Differential correction scheme

A differential correction scheme is developed to determine a halo orbit with an assigned Jacobi constant C_j^*. The flow φ and the Jacobi constant C_j are computed as first–order TSE in the system's states and time (Eq. 3.25), exploiting the definition of the STM matrix obtained by integrating the variational equation.

$$\begin{aligned} \mathbf{x} + \delta\mathbf{x} &= \varphi(\mathbf{x_0} + \delta\mathbf{x_0}, t_0; t + \delta t) = \varphi(\mathbf{x_0}, t_0; t) + \Phi(t_0, t)\delta\mathbf{x_0} + \frac{\partial \varphi}{\partial t}(\mathbf{x_0}, t_0; t)\delta t \\ C_j + \delta C_j &= C_j(\mathbf{x_0} + \delta\mathbf{x_0}, t + \delta t) = C_j(\mathbf{x_0}, t) + \frac{\partial C_j}{\partial \mathbf{x}}(\mathbf{x_0}, t)\delta\mathbf{x_0} + \frac{\partial C_j}{\partial t}(\mathbf{x_0}, t)\delta t \end{aligned} \tag{3.25}$$

The partial derivative of the flow with respect to the final time is equal to the right hand side of the dynamics $\boldsymbol{f}(\mathbf{x}, t)$ (Eq. 3.7). In addition, the Jacobi constant does not vary in time, if no perturbations nor maneuver are applied. Therefore, this relations can be simplified obtaining the following square linear system:

$$\begin{gathered} \begin{bmatrix} \delta\mathbf{x} \\ \delta C_j \end{bmatrix} = \begin{bmatrix} \Phi(t_0, t) & \boldsymbol{f}(\mathbf{x}, t) \\ \dfrac{\partial C_j}{\partial \mathbf{x}}(\mathbf{x_0}, t) & 0 \end{bmatrix} \begin{bmatrix} \delta\mathbf{x_0} \\ \delta t \end{bmatrix} \\ \text{where} \quad \Phi \in \mathbb{R}^{6\times6}, \quad \boldsymbol{f} \in \mathbb{R}^{6\times1}, \quad \frac{\partial C_j}{\partial \mathbf{x}} \in \mathbb{R}^{1\times6}, \quad 0 \in \mathbb{R}^{1\times1} \end{gathered} \tag{3.26}$$

or simply denoted as:

$$\mathbf{a} = \mathbf{B}\mathbf{c} \tag{3.27}$$

Therefore, the vector $\mathbf{c}$ is simply obtained as:

$$\mathbf{c} = \mathbf{B}^{-1}\mathbf{a} \tag{3.28}$$

Eq. (3.28) is used to determine the differential correction $\delta\mathbf{x}_{0,i}$, required to satisfy a set of constraints ($\mathbf{a}$). In this case, they can be expressed as the difference between a set of target conditions and the values of the initial states propagated until a final time t:

$$\mathbf{a} = \begin{bmatrix} \delta\mathbf{x}_i \\ \delta C_j \end{bmatrix} = \begin{bmatrix} \mathbf{x}_{target} - \mathbf{x}_i(t) \\ C_j^* - C_{j,i}(t) \end{bmatrix} \tag{3.29}$$

These target values are determined based on the symmetry of the solutions of the CRTBP:

$$\mathcal{S} : (x, y, z, \dot{x}, \dot{y}, \dot{z}, t) \rightarrow (x, -y, z, -\dot{x}, \dot{y}, -\dot{z}, -t) \tag{3.30}$$

Therefore, the trajectory has to cross the xz–plane with a velocity vector perpendicular to the plane itself. It is possible to exploit this symmetry to determine periodic solutions. In fact, the initial guess in the differential correction is set to be located on the xz–plane.

$$\mathbf{x_0} = \begin{bmatrix} x_0, & 0, & z_0, & 0, & v_{y,0}, & 0 \end{bmatrix}^T \tag{3.31}$$

The variation has to preserve the symmetry in the solution of the problem, therefore the correction will act only on part of the initial state, as presented in Eq. (3.32).

$$\hat{\mathbf{c}} = \begin{bmatrix} \delta x_{0,i}, & \delta z_{0,i}, & \delta v_{y0,i}, & \delta t_i \end{bmatrix}^T \tag{3.32}$$

The ($\hat{}$) notation is used to denote the reduced vectors and matrices. In order to solve the previous system, the initial conditions are propagated until an event function detects the crossing of the xz–plane, then the value of the states and the Jacobi constant are retrieved. If the orbit was already periodic this would happen after half a period ($T/2$).

$$\mathbf{x}_i(t) = \begin{bmatrix} x_i(t), & 0, & z_i(t), & v_{x,i}(t), & v_{y,i}(t), & v_{z,i}(t) \end{bmatrix}^T \tag{3.33}$$

Those quantities are required to compute $\mathbf{a}$. In fact, this vector can be expressed as the difference between the target states and the ones obtained as a result of the integration process. This set of constraints are imposed only on part of the state, to avoid introducing limitations on values which are not bounded by the problem's requirements.

$$\hat{\mathbf{a}} = \begin{bmatrix} y_{targ} - y_i \\ v_{x,targ} - v_{x,i} \\ v_{z,targ} - v_{z,i} \\ C_j^* - C_{j,i} \end{bmatrix} = \begin{bmatrix} 0 - 0 \\ 0 - v_{x,i}(t) \\ 0 - v_{z,i}(t) \\ C_j^* - C_{j,i} \end{bmatrix} \tag{3.34}$$

As a result, the linear system described in Eq. (3.28) can be written as:

$$\hat{\mathbf{c}} = \begin{bmatrix} \Phi_{21} & \Phi_{23} & \Phi_{25} & f_2 \\ \Phi_{41} & \Phi_{43} & \Phi_{45} & f_4 \\ \Phi_{61} & \Phi_{63} & \Phi_{65} & f_6 \\ C_{j/x} & C_{j/z} & C_{j/v_y} & 0 \end{bmatrix}^{-1} \hat{\mathbf{a}} \tag{3.35}$$

This algorithm is repeated to determine the differential correction $\delta\mathbf{x}_{0,i}$, until the errors committed with respect to the target values are lower than a set tolerance.

As a result, families of halo orbits can be determined exploiting a numerical continuation based on the Jacobi constant. The solution found at a previews step becomes the initial guess for a new differential correction scheme where the value of C_j is slightly modified. If the difference in the Jacobi constant is small enough, the algorithm converges in a few iterations.

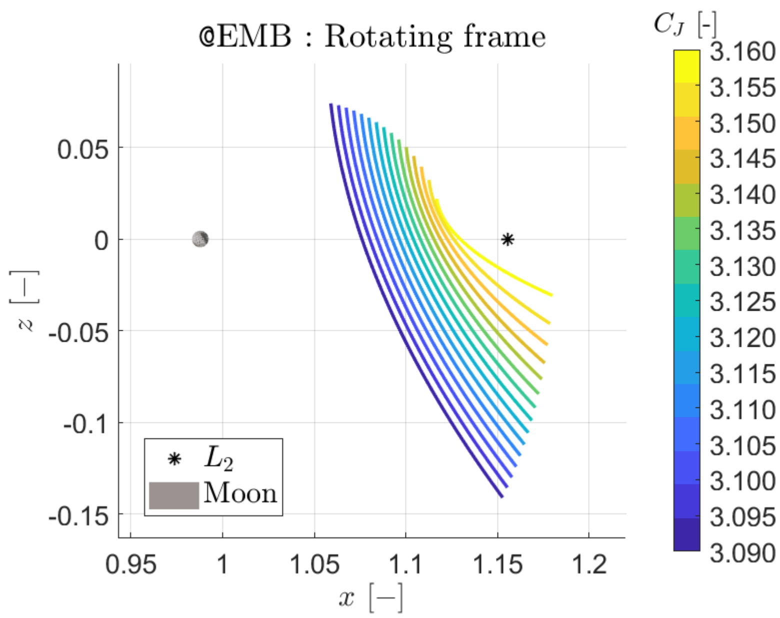

Figure 3.3: Family of southern halo orbits about L_2 in the EM system, xz–plane

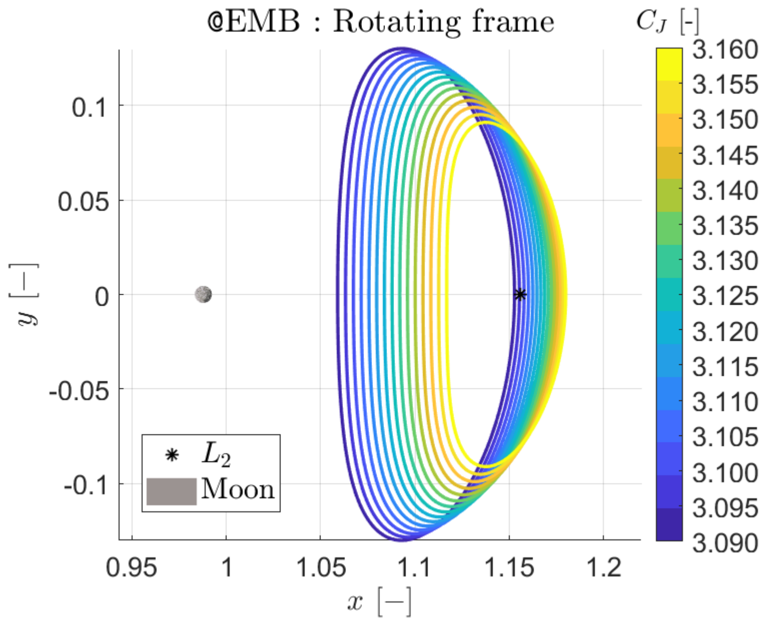

Figure 3.4: Family of southern halo orbits about L_2 in the EM system, xy–plane

3.1.4. Invariant Manifolds

In the CRTBP it is possible to leverage the natural dynamics to compute transfer trajectories targeting periodic solutions about the collinear points [25]. These orbits are unstable due to the presence of the saddle part in the linearized solution, which determines an hyperbolic behavior. However, this instability is not entirely a problem, as it can be used to design an asymptotic trajectory with an injection maneuver of negligible cost.

In fact, stable and unstable invariant manifolds emerge from periodic orbits around L_1, L_2 and L_3. In general, an invariant manifold is a m–dimensional surface defined in $\mathbb{R}^n$. A point on this surface is bound to it under the the assumption of natural motion, without a possibility to leave this subspace.

In the six–dimensional space of the CRTBP, a periodic orbit is considered to be a one–dimensional solution, dependent only on a time coordinate:

$$\mathbf{x} = \varphi(\mathbf{x}_0; t_{po}) \quad \text{where} \quad t_{po} \in [0, T] \tag{3.36}$$

where T is the period. Instead, a manifold is a two–dimensional tubular structure, dependent on an additional time variable t_m. To compute this surface, a perturbed initial condition about a periodic orbit is propagated along the asymptotic directions of motion. This directions are determined by introducing the monodromy matrix M, which is defined as the STM evaluated after a full period:

$$M = \Phi(\mathbf{x}_0, t_0; t_0 + T) \tag{3.37}$$

where t_0 can be arbitrarily assumed to be zero, since the CRTPB is an autonomous system. This matrix is used to assess the stability in the proximity of a periodic solution, as it maps an initial displacement to its value after a full period. Therefore, the stable and unstable directions are computed, respectively, as the stable and unstable eigenvectors ($\boldsymbol{\nu}_s$, $\boldsymbol{\nu}_u$) of the monodromy matrix M.

In principle, the eigenvalue problem should be solved for each point belonging to the periodic solution to determine the local value of $\boldsymbol{\nu}_s(t_{po})$, $\boldsymbol{\nu}_u(t_{po})$. To reduce the computational effort, the stable and unstable directions are propagated to the required time t_{po} using the STM, as proposed in [32].

$$\boldsymbol{\nu}(t_{po}) = \Phi(\mathbf{x}_0, t_{po})\boldsymbol{\nu}_0 \tag{3.38}$$

In this way, the eigenvalue problem is solved only once. To determine the initial condition along the manifold, a small displacement ε is applied to a state vector belonging to the periodic orbit along these directions. The validity of the linear assumption deteriorates rapidly as the distance from the periodic solution increases. Thus, a small ε in the order of 10^{-6} in nodimensional units is often adopted.

Accordingly, a generic point on the stable and unstable manifolds is defined as:

$$\begin{aligned} \mathbf{x}_s(t_{po}, t_m) &= \varphi(\mathbf{x}(t_{po}) \pm \varepsilon\boldsymbol{\nu}_s(t_{po}), -t_m) \\ \mathbf{x}_u(t_{po}, t_m) &= \varphi(\mathbf{x}(t_{po}) \pm \varepsilon\boldsymbol{\nu}_u(t_{po}), t_m) \end{aligned} \qquad \text{where} \quad t_m > 0 \tag{3.39}$$

The sign applied to the displacement determines whether the inner or the outer branch is generated. In particular, trajectories belonging to the stable manifold tend to the periodic solution with an asymptotical motion. Therefore they are computed by propagating the displaced initial conditions back in time. Whereas, the unstable manifold is integrated forward in time, as it rapidly escapes the region about the collinear point.

Given the target orbit of the LUMIO mission, this method is applied in this thesis to determine the stable manifolds about L_2 point. In particular, the inner brach will be used to compute possible transfer trajectories, as it intersects a region of space where the elliptical lunar orbits are located.

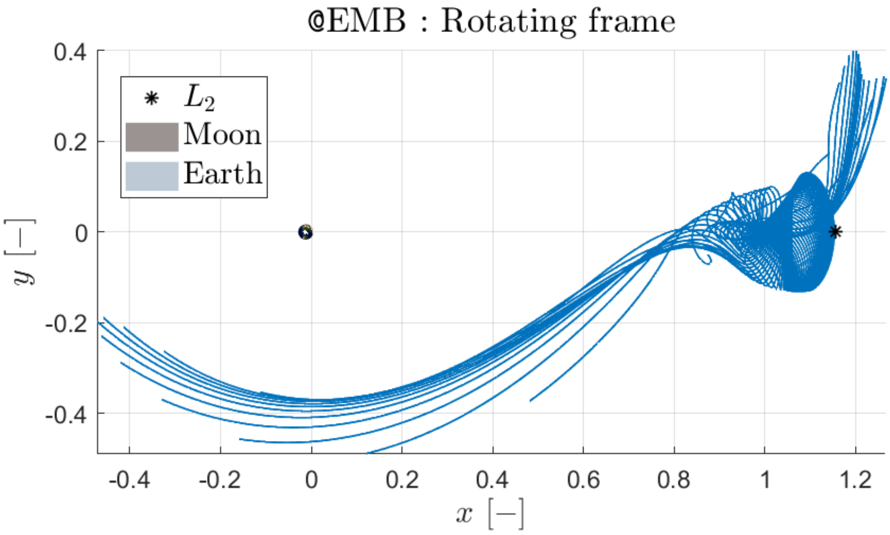

Figure 3.5: Stable inner manifold emerging from the target orbit

3.2. Restricted n–Body Problem in a Roto–Pulsating Reference Frame

As the constraints applied to recent mission designs become more demanding, the CRTBP is not sufficient to model the behavior of a spacecraft in highly nonlinear environments with the required precision. Therefore, this model is used mostly in early stages of the mission analysis to determine periodic solutions and to exploit the invariant manifolds. After a preliminary trajectory optimization is completed, a successive refinement takes place to account for other disturbances present in the real environment. According to multiple studies [11, 12], a hierarchical approach has proven to be successful in computing solutions in an higher fidelity models.

This process becomes crucial for spacecrafts flying in regions of space where two major bodies are not sufficient to determine the dynamics. Consequently, the Restricted n–Body Problem in a Roto–Pulsating Reference Frame is introduced to expand on the CRTBP formulation, by adding an arbitrary number of attractors. The position of these major bodies is retrieved directly from JPL ephemerides DE432 to achieve a greater fidelity. Additionally, the model takes into account the effect of the solar radiation pressure (SRP) as well as the J_2 term associated with spherical harmonics of the Moon gravitational field, which significantly affects the trajectory of low lunar orbits (LLO). In this thesis, the transfer trajectories depart from an elliptic lunar orbit with a low pericenter, therefore the J_2 perturbing term cannot be neglected to accurately model the dynamics.

Initially, the equations of motion of the n–body problem are derived in an inertial frame centered at the Solar System Barycenter (SSB) according to Lagrangian formalism. In a successive step, the equations are transformed into the Roto–Pulsating Frame (RPF), which provides several benefits.

Inertial RnBP centered at the SSB

A brief introduction to the nomenclature is provided to define the following notation. Let's consider a particle of negligible mass with a position vector $\mathbf{R} = [X, Y, Z]^T$ subject to the attraction of a set of primaries S. This set is formed by all the planets of the solar system, the Sun, the Moon and Pluto. These bodies are characterized by the gravitational parameter μ_j and by their position vector labeled as $\mathbf{R}_j$. Within this notation, the potential per unit mass can be expressed as stated in [13], with minor variations of the frame in which the J_2 acceleration is defined. Then, the gradient takes the following form:

$$\nabla V = \nabla\Omega_1 + \nabla\Omega_2 + \nabla\Omega_3 \tag{3.40a}$$

$$\nabla\Omega_1 = \sum_{j\in S} \mu_j \left[\frac{\mathbf{R}-\mathbf{R}_j}{\|\mathbf{R}-\mathbf{R}_j\|^3}\right] \tag{3.40b}$$

$$\nabla\Omega_2 = B^T \left(\frac{3}{2} J_{2,m}\mu_m R_{B_m}^2 \left(\frac{I + 2I_z}{\|\mathbf{R}-\mathbf{R}_m\|^5}\right) B(\mathbf{R}-\mathbf{R}_m)\right) \tag{3.40c}$$

$$\nabla\Omega_3 = B^T \left(\frac{3}{2} J_{2,m}\mu_m R_{B_m}^2 \left(-\frac{5\,(\mathbf{R}-\mathbf{R}_m)^T B^T I_z B(\mathbf{R}-\mathbf{R}_m)}{\|\mathbf{R}-\mathbf{R}_m\|^7}\right) B(\mathbf{R}-\mathbf{R}_m)\right) \tag{3.40d}$$

$$\text{with} \quad B = R_{J2000\rightarrow Moon\_PA}(et)$$

where $\mathbf{R}_m$ and R_{B_m} are, respectively, the position of the Moon in the SSB and its equatorial radius; $J_{2,m}$ is the second order term of the spherical harmonics describing the Moon's gravity; I is a 3-by-3 identity matrix and I_z is a null matrix except for the last element on the diagonal, which is equal to 1.

Moreover, the second and last term of the gradient feature a rotation matrix, denoted as B to shorten the notation. This transformation is required to convert the relative distance of the massless particle to the Moon in a body–fixed frame (MOON_PA), where the J_2 acceleration term is defined[1]. Subsequently, the acceleration has to be transformed back into the inertial frame compatible with the rest of the equations (J2000). The rotation matrix is computed with the SPICE routine `pxform` at a specific epoch time, defined as

[1]The table of the SHA coefficients is retrieved from https://pgda.gsfc.nasa.gov/products/50

the number of seconds past J2000.

A part from the gravitational interactions, this formulation accounts for the presence of a non conservative term, modeled as an acceleration caused by the SRP ($\mathbf{a}_{\mathrm{SRP}}$). The force exerted by the electromagnetic radiation is considerably smaller than other terms featured in ∇V, however it's contribution it treated as a perturbation. The influence of this term is more prominent is case of long trajectories and for the stability of quasi–periodic solutions. This non conservative acceleration is evaluated based on the cannonball model, assuming the solar flux to be inversely proportional to the square of the distance of the spacecraft from the Sun. According to this model, $\mathbf{a}_{\mathrm{SRP}}$ is computed as:

$$\mathbf{a}_{\mathrm{SRP}} = SP_0 \frac{\mathbf{R} - \mathbf{R}_s}{\|\mathbf{R} - \mathbf{R}_s\|^3} \tag{3.41}$$

where SP_0 is the SRP parameter defined as:

$$SP_0 = (1 + c_r)\,\frac{A_{\mathrm{SRP}}}{m}\,\frac{\Psi_0 d_0^2}{c}. \tag{3.42}$$

and d_0 is the distance equal to 1 AU at which the reference radiation pressure Ψ_0 is defined; c is the speed of light; $\mathbf{R}_S$ is the position vector of the Sun.

The rest of the parameters depend on physical properties and dimensions of the spacecraft. For the purpose of this thesis, the following values can be assumed as good approximations for the LUMIO Cubesat. The illuminated surface area is estimated to be $A_{\mathrm{SRP}} = 0.23\,\mathrm{m}^2$ with a reflective coefficient $c_r = 0.3$ and a mass of $m = 28.7$ kg.

According to Lagrangian formalism, the equations of motion in the inertial frame are :

$$\ddot{\mathbf{R}} + \nabla V = \mathbf{a}_{SRP} \tag{3.43}$$

However, this model presents some limitations. As the reference frame in centered it the SSB, the position vector describing the motion about the Earth–Moon system is considerably large. It would be difficult and computationally expensive to achieve strict integration tolerances, as the variation in the state coordinates is several times smaller than the states themselves. This effect can be reduced significantly by shifting the center in the Earth–Moon barycenter (EMB) and by introducing a rotating frame, which is better able at representing the natural dynamics of such system. By introducing this new frame, it is also possible to determine a nondimesional set of equations, making the problem more efficient to be solved numerically. In the next section, a model in the RPF is derived, based on the generalization of the CRTBP.

3.2.1. Nondimensional RnBP–RPF

In this thesis the RnBP is expressed in the Roto–Pulsating frame (RPF) to model the motion of a spacecraft in the Earth–Moon system with precision. This frame is defined in analogy with the model adopted for the CRTBP. As a result, the two main bodies acting on the massless particle are selected as primaries, denoted as P_1 and P_2 with mass m_1 and m_2. The barycenter of the primaries becomes the center of the new frame. The directions of the unit vectors follow a similar definition to their counterpart in the CRTBP. The x–axis is directed from the more massive primary towards the other and the z–axis is pointing in the direction of the angular momentum of the system. Lastly, the y–axis is defined in order to complete the right–handed frame.

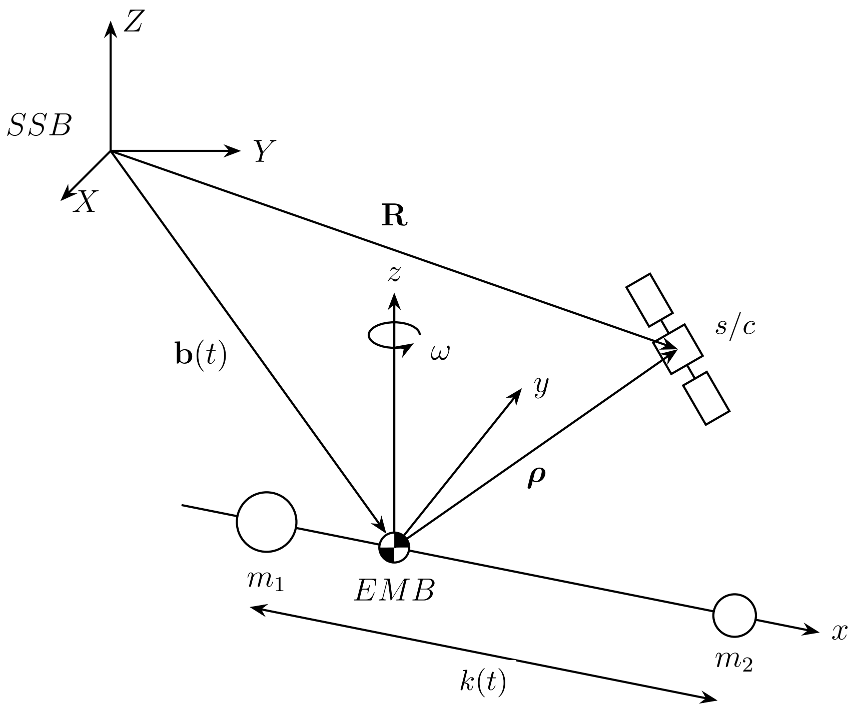

Figure 3.6: Conversion between inertial frame (X, Y, Z) and roto-pulsating frame (x, y, z)

In this new model the position of the celestial bodies is retrieved from the ephemerides. Consequently, the RnBP–RPF is not an autonomous system due to the direct dependence on time. Moreover, the relative position of the primaries varies with time, thus explaining the pulsating term introduced in the name of the model.

In order to state the equations of motion in the RPF, it is necessary to introduce a conversion between the two reference frames. This process involves a translation of the origin from the SSB to the barycenter of the primaries ($\mathbf{b}$). Then, the translated position vector is rotated by an orthogonal cosine angle matrix C, assembled according to Eq. (3.46).

$$\mathbf{b}(t) = \frac{m_1\mathbf{R}_1 + m_2\mathbf{R}_2}{m_1 + m_2} \tag{3.44}$$

$$k(t) = \|\mathbf{R}_2 - \mathbf{R}_1\| \tag{3.45}$$

$$C(t) = [\mathbf{e}_1,\ \mathbf{e}_2,\ \mathbf{e}_3] \tag{3.46}$$

where $\mathbf{b}$ is the position of the barycenter expressed in the inertial frame centered at the SSB; $k(t)$ is the distance between the primaries used as the scale length; $\mathbf{e}_1$, $\mathbf{e}_2$, $\mathbf{e}_3$ are the unit vectors forming the basis of the RPF expressed in the inertial coordinates to define the rotation matrix:

$$\mathbf{e}_1 = \frac{\mathbf{R}_2 - \mathbf{R}_1}{\|\mathbf{R}_2 - \mathbf{R}_1\|} \tag{3.47}$$

$$\mathbf{e}_2 = \mathbf{e}_3 \times \mathbf{e}_1 \tag{3.48}$$

$$\mathbf{e}_3 = \frac{(\mathbf{V}_2 - \mathbf{V}_1) \times (\mathbf{R}_2 - \mathbf{R}_1)}{\|(\mathbf{V}_2 - \mathbf{V}_1) \times (\mathbf{R}_2 - \mathbf{R}_1)\|} \tag{3.49}$$

The mapping is completed by a nondimensionalization process, introduced to properly scale the problem. Therefore, the time, position and velocity $(t, \mathbf{R}, \mathbf{V})$ are transformed in their adimensional counterpart $(\tau, \boldsymbol{\rho}, \boldsymbol{\eta})$ in the RPF. In particular, the normalization of time is based on the mean motion of the primaries, assuming a mean distance $\overline{a}$, averaged over a long period of time [12]:

$$\omega = \sqrt{\frac{\mu_1 + \mu_2}{\overline{a}^3}} \tag{3.50}$$

The scaling is essential to define a model where the coordinates have roughly the same order of magnitude to ease the trajectory optimization as well as to improve the computation time of variable step numerical integrators. As a result, this mapping process can be summed up by the following equations:

$$\mathbf{R}(t) = \mathbf{b}(t) + k(t)\, C(t)\, \boldsymbol{\rho}(\tau) \tag{3.51}$$

$$\mathbf{V}(t) = \dot{\mathbf{b}}(t) + \dot{k}(t)\, C(t)\, \boldsymbol{\rho}(\tau) + k(t)\, \dot{C}(t)\, \boldsymbol{\rho}(\tau) + k(t)\, C(t)\, \dot{\boldsymbol{\rho}}(\tau)\, \dot{\tau} \tag{3.52}$$

$$\tau = \omega(t - t_0) \tag{3.53}$$

where t_0 is a reference epoch set to be ”2029-Jan-01 00:00:00”.

To conclude this section, the equations of motion in the RFP are determined by applying the inverse mapping process to the inertial form of the equations (Eq. 3.43). The complete equation is reported hereafter:

$$\boldsymbol{\rho}'' + \frac{1}{\omega}\left(\frac{2\dot{k}}{k}I + 2C^T\dot{C}\right)\boldsymbol{\rho}' + \frac{1}{\omega^2}\left(\frac{\ddot{k}}{k}I + 2\frac{\dot{k}}{k}C^T\dot{C} + C^T\ddot{C}\right)\boldsymbol{\rho}$$
$$+ \frac{C^T\ddot{\boldsymbol{b}}}{k\omega^2} = \nabla\Omega + \frac{SP_0}{k\omega^2}\frac{\boldsymbol{\delta}_s}{\delta_s^3} \tag{3.54}$$

where the notation $(\,'\,)$ denotes the derivatives with respect to the adimensional time and the nondimensional pseudopotential Ω is defined as:

$$\Omega = \sum_{j\in S}\frac{\hat{\mu}_j}{\delta_j} + \frac{J_{2,m}\hat{\mu}_m R_{B_m}^2}{2k^2}\left(\frac{1}{\delta_m^3} - \frac{3\boldsymbol{\delta}_m^T M\boldsymbol{\delta}_m}{\delta_m^5}\right) \tag{3.55}$$

$$\nabla\Omega = \sum_{j\in S} -\frac{\hat{\mu}_j}{\delta_j^3}\boldsymbol{\delta}_j + \frac{3J_{2,m}\hat{\mu}_m R_{B_m}^2}{2k^2}\left(-\frac{\boldsymbol{\delta}_m}{\delta_m^5} + \frac{5\boldsymbol{\delta}_m^T M\boldsymbol{\delta}_m}{\delta_m^7}\boldsymbol{\delta}_m - \frac{2M\boldsymbol{\delta}_m}{\delta_m^5}\right) \tag{3.56}$$

$$M = C^T\, B^T\, I_z\, B\, C \tag{3.57}$$

where $\boldsymbol{\delta}_j = \boldsymbol{\rho} - \boldsymbol{\rho}_j$ is the relative distance from the j–th body expressed in nondimensional coordinates and δ_j is the corresponding magnitude and $\hat{\mu}_j = m_j/(m_1+m_2)$. The subscripts m and s are used to denote quantities expressed with respect to the Moon and Sun. More details on the derivation process of this formulation, along with the definition of the time derivatives of some terms, can be found in the master thesis developed by Veruari [34] based on the foundations introduced by Dei Tos [10].

3.2.2. State Transition Matrix of the RnBP–RPF

The state transition matrix is determined once more by solving the variational equations, as previously introduced in Section 3.1.2.

For the RnBP–RPF, the Jacobian of the dynamics is derived following [13] and it is reported hereafter for completeness:

$$A(t) = \begin{bmatrix} \mathbf{0} & I \\ \dfrac{\partial \boldsymbol{f}_\eta}{\partial \boldsymbol{\rho}} & \dfrac{\partial \boldsymbol{f}_\eta}{\partial \boldsymbol{\eta}} \end{bmatrix} \tag{3.58}$$

where

$$\frac{\partial \boldsymbol{f}_\eta}{\partial \boldsymbol{\rho}} = -\frac{1}{\omega^2}\left(\frac{\dot{k}}{k}I + 2\frac{\dot{k}}{k}C^T\dot{C} + C^T\ddot{C}\right) - \sum_{j\in S}\hat{\mu}_j\left[\frac{I}{\delta_j^3} - \frac{3\boldsymbol{\delta}_j\boldsymbol{\delta}_j^T}{\delta_j^5}\right]$$
$$- \frac{3J_{2,m}\hat{\mu}_m R_{B_m}^2}{2k^2}\left(\frac{I+2M}{\delta_m^5} - \frac{(5I+10M)\,\boldsymbol{\delta}_m\boldsymbol{\delta}_m^T + 5\boldsymbol{\delta}_m^T M\boldsymbol{\delta}_m I + 10\boldsymbol{\delta}_m\boldsymbol{\delta}_m^T M}{\delta_m^7}\right. \tag{3.59}$$
$$\left. + 35\boldsymbol{\delta}_m^T M\boldsymbol{\delta}_m\frac{\boldsymbol{\delta}_m\boldsymbol{\delta}_m^T}{\delta_m^9}\right) + \frac{\mathrm{SP}_0}{\omega^2 k^3}\left[\frac{I}{\delta_s^3} - \frac{3\boldsymbol{\delta}_s\boldsymbol{\delta}_s^T}{\delta_s^5}\right]$$

$$\frac{\partial \boldsymbol{f}_\eta}{\partial \boldsymbol{\eta}} = -\frac{2}{\omega}\left(\frac{\dot{k}}{k}I + C^T\dot{C}\right)$$

3.2.3. Quasi–Halo orbits

The RnBP–RPF does not admit periodic solutions about the collinear points in a strict sense, as the equilibrium points are not stationary either. Therefore, existing periodic solutions determined in the CRTBP loose this property in higher fidelity models, due to the additional forces being considered. These extra terms act as perturbations, making the solution deviate from the trajectory designed in the simpler model.

Nevertheless, this periodic solutions can be used in a successive refinement process to determine quasi–periodic counterparts in the RnBP–RPF. This method has already been explored and proven successful in [11].

The process adopted in this thesis to determine the target quasi–halo is identical to the one investigated in the article. Initially, a periodic solution in the CRTBP is discretised over m points equally spaced in time $\mathbf{s}_k = \mathbf{x}(t_k)$. These points become the initial guesses for the nodes in a modified multiple–shooting problem, solved in the RnBP–RPF. This can be formulated as an NLP problem with an objective function J defined as a quadratic form of the continuity constraints, dependent on the vector of unknowns $\mathbf{s} = (\mathbf{s}_1, \mathbf{s}_2, ..., \mathbf{s}_k, ..., \mathbf{s}_m)$.

$$\min_{\mathbf{s}} J(\mathbf{s}) = \frac{1}{2}\mathbf{c}^T\mathbf{c} \qquad \text{subject to} \qquad \mathbf{c}(\mathbf{s}) = \begin{bmatrix} \zeta_1 \\ \zeta_2 \\ \dots \\ \zeta_{m-1} \end{bmatrix} = \mathbf{0}, \tag{3.60}$$

where the constraint vector $\mathbf{c}(\mathbf{s})$ contains the following equality relations $\boldsymbol{\zeta}_k$:

$$\zeta_k = \varphi(\mathbf{s}_k, t_k; t_{k+1}) - \mathbf{s}_{k+1}, \qquad \text{with} \quad k = 1, ..., m-1 \tag{3.61}$$

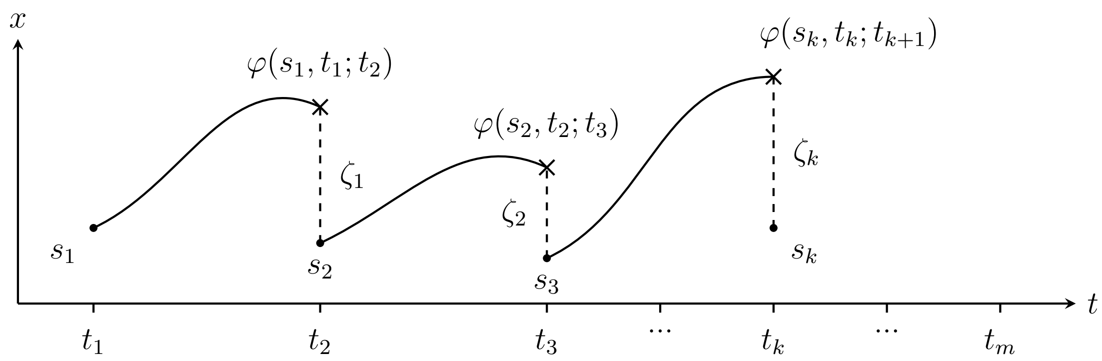

Figure 3.7: Multiple shooting strategy to determine quasi–halo orbits

The problem is solved by determining the set of nodes such that $\boldsymbol{\zeta}_k = 0$ for each value of $k = 1, ..., m-1$. By imposing an optimization function shaped like a quadratic form of the constraints, the deviation between the final trajectory and the reference one is minimized. It is worth noting that the problem has free–free boundary conditions, therefore the "head" and "tail" tend to deviate more than other nodes from a quasi–periodic solution. This can be explained by the reduced number of constraints imposed at the boundaries, since only one neighboring node is present. To alleviate the problem, it is sufficient to overextend the time window of interest and to remove the head and tail of the solution afterwards. This regions could contain one or multiple nodes depending on the case, requiring a dedicated post–process.

This NLP problem is solved numerically with MATLAB `fmincon`, using the interior point algorithm. To improve the efficiency and convergence, the Jacobian of the constraints ($\mathcal{G}_{eq}$) is evaluated using the STM computed with the variational equations.

$$\mathcal{G}_{eq}(\mathbf{s}) = \begin{bmatrix} \Phi_1 & -I_6 & 0 & & 0 \\ 0 & \Phi_2 & -I_6 & \ddots & \\ & \ddots & \ddots & \ddots & 0 \\ 0 & & 0 & \Phi_{m-1} & -I_6 \end{bmatrix}, \tag{3.62}$$

This method will be used as an intermediate step of the refinement process described in Chapter 5. Hereafter, an example of the quasi–halo about the L_2 point of the Earth–Moon system is reported:

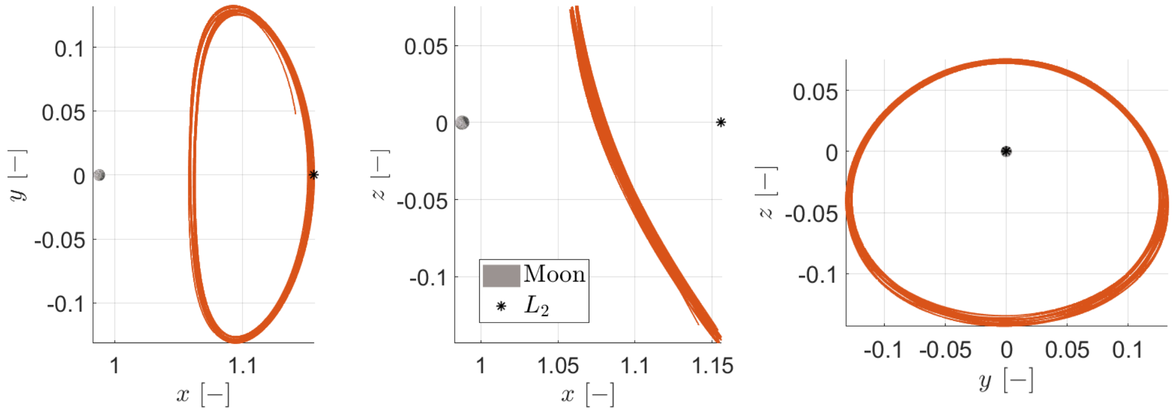

Figure 3.8: LUMIO's quasi–halo orbit determined in the RPF over a period of 270 days starting on 1 January, 2029

3.3. Restricted n–Body Problem in a planeto–centric frame

An additional model is introduced to alleviate the computational burden of determining a solution orbiting close to one of the primaries. This problem emerges in the optimization process carried out in the RnBP, especially when computing the first arc close to the Moon. In this case, the relative distance of the spacecraft to the primary ($\boldsymbol{\delta}_m$) is considerably small compared to other terms involved in the equation of motion (Eq. 3.54). This, in turn, leads to a significant increase in the number of steps required by the variable–step numerical integrator to meet the imposed tolerances.

To reduce this effect, the inertial RnBP introduced in Eq. (3.43) is modified by shifting the origin of the reference frame from the SSB to the center of the Moon. This approach is not a novelty in the literature, as it has been largely investigated to model the Restricted Two Body Problem (RTBP) subject to gravitational attraction of other bodies [3, 33]. These gravitational terms are treated as perturbations, therefore the assumption is most effective if the motion of a spacecraft is well approximated by a conic or Keplerian orbit. The resulting equation of motion can be formulated as:

$$\ddot{\mathbf{r}} = -\mu_m \frac{\mathbf{r}}{r^3} - \sum_{j \in S^*} \mu_j \left(\frac{\mathbf{d}_j}{d_j^3} + \frac{\boldsymbol{\rho}_j}{\rho_j^3} \right) + \mathbf{a}_{J_2} + \mathbf{a}_{SRP} \tag{3.63}$$

where

$$\mathbf{r} = \mathbf{r}_{sc} - \mathbf{r}_m \tag{3.64}$$

$$\mathbf{d}_j = \mathbf{r}_{sc} - \mathbf{r}_j \tag{3.65}$$

$$\boldsymbol{\rho}_j = \mathbf{r}_j - \mathbf{r}_m \tag{3.66}$$

$$\mathbf{a}_{SRP} = SP_0 \left(\frac{\mathbf{d}_s}{d_s^3}\right) = (1 + c_r)\frac{A_{SRP}}{m}\left(\frac{\Psi_0 d_0^2}{c}\right)\frac{\mathbf{d}_s}{d_s^3} \tag{3.67}$$

$$\mathbf{a}_{J_2} = -B^T \left(\frac{3J_{2,m}\,\mu_m\,R_{B,m}^2}{2}\right)\left[\frac{I + 2I_z}{r_{PA}^5}\mathbf{r}_{PA} - \frac{5(\mathbf{r}_{PA}^T\,I_z\,\mathbf{r}_{PA})}{r_{PA}^7}\mathbf{r}_{PA}\right] \tag{3.68}$$

$$\mathbf{r}_{PA} = B(et)\,\mathbf{r} = R_{J2000\rightarrow Moon\_PA}(et)\,\mathbf{r} \tag{3.69}$$

S^* is the set of the primaries used in the RnBP–RPF except for the Moon; $\mathbf{r}_{sc}$ is the position of the spacecraft with respect to the SSB; $\mathbf{r}_m$ and $\mathbf{r}_j$ are, respectively, the position vector of the Moon and of the other celestial bodies with respect to the SSB; $\mathbf{r}_{PA}$ is the relative position of the spacecraft with respect to the Moon expressed in the principal axis reference frame in which the J_2 term is defined.

To alleviate the problems associated with computing the quotients in the right–hand side (RHS), the equations can be rewritten in the following form, as reported in [3].

$$\ddot{\mathbf{r}} = -\mu_m \frac{\mathbf{r}}{r^3} - \sum_{j \in S^*} \frac{\mu_j}{d_j^3}\left(\mathbf{r} - \boldsymbol{\rho}_j\, f(q_j)\right) + \mathbf{a}_{J_2} + \mathbf{a}_{SRP} \tag{3.70}$$

$$f = \frac{q_j(3 + 3q_j + q_j^2)}{1 + (1 + q_j)^{3/2}} \tag{3.71}$$

$$q_j = \frac{\mathbf{r} \cdot (\mathbf{r} - 2\boldsymbol{\rho}_j)}{\boldsymbol{\rho}_j \cdot \boldsymbol{\rho}_j} \tag{3.72}$$

3.3.1. Nondimensional nBP–Shift

In addition, the previous set of equations is transformed in a nondimensional form to reduce the computation time and to improve the numerical stability.

The scale length (DU) is set to be equal to the equatorial radius of the Moon and the time unit (TU) is defined in order to have a unitary angular velocity on a orbit having a semi major axis equal to DU. To complete the process, the velocity unit is computed as the ratio of the scale length and time unit.

$$DU = R_{R,m} \qquad VU = DU/TU \qquad TU = \sqrt{DU^3/\mu_m}$$

In the following equations, adimensional quantities are simply denoted with an asterisk:

$$\ddot{\mathbf{r}}^*(t^*) = -\frac{\mathbf{r}^*}{(r^*)^3} - \sum_{j\in S^*} \frac{\mu_j}{\mu_m\,(d_j^*)^3}\left(\mathbf{r}^* - \boldsymbol{\rho}_j^*\,f(q_j^*)\right) + \mathbf{a}_{J_2}^* + \mathbf{a}_{SRP}^* \tag{3.73}$$

$$f = \frac{q_j^*\left[3 + 3q_j^* + (q_j^*)^2\right]}{1 + (1+q_j^*)^{3/2}} \tag{3.74}$$

$$q_j^* = \frac{\mathbf{r}^* \cdot (\mathbf{r}^* - 2\boldsymbol{\rho}_j^*)}{\boldsymbol{\rho}_j^* \cdot \boldsymbol{\rho}_j^*} \tag{3.75}$$

To scale the position vectors, it is sufficient to divide by the scale length DU. The same can be said for the velocity components utilizing VU instead. Additionally, the following relations can be derived to scale the epoch time in continuity with the RnBP–RPF:

$$et = et_0 + TU\;t^* \qquad \text{and} \qquad t^* = \frac{1}{TU}(et - et_0) \tag{3.76}$$

3.3.2. State Transition Matrix of the normalized nBP

To complete the planetocentric RnBP, the variational equations are determined to propagate numerically the STM. The adimensional form of the Jacobian of the dynamics can be written as:

$$A(t) = \begin{bmatrix} \mathbf{0}_{3x3} & I_{3x3} \\ \dfrac{\partial \boldsymbol{f}_v}{\partial \mathbf{r}} & \mathbf{0}_{3x3} \end{bmatrix} \tag{3.77}$$

where

$$\begin{aligned} \frac{\partial \boldsymbol{f}_v}{\partial \mathbf{r}^*} &= \frac{3}{(r^*)^5}\mathbf{r}^*\,(\mathbf{r}^*)^T - \frac{I}{(r^*)^3} - \sum_{j\in S^*}\left[-\frac{3\mu_j}{\mu_m (d_j^*)^5}\left(\mathbf{r}^* + \boldsymbol{\rho}^* f(q_j^*)\right)(\mathbf{d}_j^*)^T\right] \\ &- \sum_{j\in S^*}\left[\frac{\mu_j}{\mu_m (d_j^*)^3}\left(I + \boldsymbol{\rho}_j^* \frac{\partial f}{\partial \mathbf{r}^*}\right)\right] + \frac{\partial \mathbf{a}_{J_2}^*}{\partial \mathbf{r}^*} \end{aligned} \tag{3.78}$$

The other terms featured in this notation are reported hereafter:

$$\frac{\partial \boldsymbol{f}_v}{\partial \mathbf{r}^*} = \frac{3}{(r^*)^5}\mathbf{r}^*\left(\mathbf{r}^*\right)^T - \frac{I}{(r^*)^3} - \sum_{j\in S^*}\left[-\frac{3\mu_j}{\mu_m (d_j^*)^5}\left(\mathbf{r}^* + \boldsymbol{\rho}^* f(q_j^*)\right)(\mathbf{d}_j^*)^T\right]$$

$$- \sum_{j\in S^*}\left[\frac{\mu_j}{\mu_m (d_j^*)^3}\left(I + \boldsymbol{\rho}_j^*\frac{\partial f}{\partial \mathbf{r}^*}\right)\right] + \frac{\partial \mathbf{a}_{J_2}^*}{\partial \mathbf{r}^*} + \frac{\partial \mathbf{a}_{SRP}^*}{\partial \mathbf{r}^*} \tag{3.79}$$

$$\frac{\partial \mathbf{a}_{J_2}^*}{\partial \mathbf{r}^*} = B^T\left(-\frac{3J_{2,m}}{2}\right)\Bigg\{ -\frac{5}{(r_{PA}^*)^7}(\mathbf{r}_{PA}^* + 2I_z\mathbf{r}_{PA}^*)(\mathbf{r}_{PA}^*)^T + \frac{I+2I_z}{(r_{PA}^*)^5}$$

$$+ \frac{35}{(r_{PA}^*)^9}\left[(\mathbf{r}_{PA}^* + 2I_z\mathbf{r}_{PA}^*)(\mathbf{r}_{PA}^*)^T\right] - \frac{10}{(r_{PA}^*)^7}\mathbf{r}_{PA}^*(I_z\mathbf{r}_{PA}^*)^T$$

$$- \frac{5}{(r_{PA}^*)^7}\left[(\mathbf{r}_{PA}^*)^T I \mathbf{r}_{PA}^*\right] I \Bigg\} \tag{3.80}$$

$$\frac{\partial \mathbf{a}_{SRP}^*}{\partial \mathbf{r}^*} = \frac{SP_0}{\mu_m}\left(-\frac{3}{(d_s^*)^5}\mathbf{d}_s^*(\mathbf{d}_s^*)^T + \frac{I}{(d_s^*)^3}\right) \tag{3.81}$$

$$\frac{\partial f}{\partial \mathbf{r}^*} = \frac{\partial f}{\partial q_j^*}\frac{\partial q_j^*}{\partial \mathbf{r}^*} \tag{3.82}$$

$$\frac{\partial f}{\partial q_j^*} = \frac{\left[3 + 3q_j^* + (q_j^*)^2 + q_j^*(3+2q_j^*)\right]\left[1 + (1+q_j^*)^{3/2}\right]}{\left[1+(1+q_j^*)^{3/2}\right]^2}$$

$$+ \frac{-\frac{3}{2}(1+q_j^*)^{1/2}q_j^*(3 + 3q_j^* + (q_j^*)^2)}{\left[1+(1+q_j^*)^{3/2}\right]^2} \tag{3.83}$$

$$\frac{\partial q_j^*}{\partial \mathbf{r}^*} = \left(\frac{2\mathbf{r}^* - \boldsymbol{\rho}_j^*}{(\rho_j^*)^2}\right) \tag{3.84}$$

4 | Impulsive Trajectory Optimization in the CRTBP

In this thesis, the aim is to design a transfer trajectory from an elliptical lunar orbit to the target halo of the LUMIO mission. The following chapter develops the methodology required by the first step in the trajectory optimization. The equations of motion are modeled according to the CRTBP, to exploit the presence of periodic solutions about the Lagrange points as well as to leverage free transport mechanisms offered by the invariant manifolds. Different articles have already investigated the possibility to achieve transfers in the Earth–Moon system by placing a spacecraft on the stable manifolds emerging from the target periodic orbits [25, 35]. With this approach, the insertion cost in the final orbit is theoretically zero, as the trajectories tend to the periodic solution asymptotically.

To leverage this property, the stable inner manifold is computed numerically and sampled in a discrete number of trajectories. This allows to determine which solutions intersect the region surrounding the Moon, where the spacecraft is located on a parking orbit. Then, the samples satisfying constraints on relative position and velocity are considered good candidates to set up a NLP formulation. They are employed to evaluate the initial guess of the optimization vector in a multiple shooting problem with multiple maneuvers. As the number of admissible candidates is very large, a selection process is implemented to determine the most representative initial guesses spanning the vector space with a k–medoids method [26]. Lastly, the optimization method is applied to the selected initial conditions to compute solutions that are going to be successively refined in more complex dynamical models.

4.1. Initial guesses determination

The quality of the initial guesses is essential to ensure the convergence and the performance of a NLP problem. To retrieve good candidates, the inner stable manifold is computed numerically based on a periodic solution, which has to be evaluated.

The target orbit is a halo about the L_2 point of the Earth–Moon system. It is possible to determine this orbit with a differential correction scheme described in Section 3.1.3. This method exploits the symmetry of the solutions in the CRTPB along with the conservation of the integral of motion, which is set to be $C_j = 3.09$. In the case of the LUMIO mission, the operational orbit and the related Jacobi constant were selected after a careful tradeoff process, documented in previous phases of the mission design (Phase 0) [8].

The initial conditions provided to the differential correction method are located on the xz–plane, to take advantage of the symmetry. In this way, the size of the problem is scaled down to only four unknowns (x_0, z_0, $v_{y,0}$, T), as described in more detail in Section 3.1.3. This iterative correction scheme is able to converge in a few steps achieving a periodic solution with the intended Jacobi constant. The stopping criterion is based on the maximum allowed error in the constraint vector. Once all terms are below a threshold of 10^{-10}, the algorithm stops and the following initial condition $\mathbf{x}_0$ is retrieved:

	Initial Guess	Solution
x_0	1.068792441776	1.059040207683
y_0	0	0
z_0	0.071093328515	0.073927737791
v_{x0}	0	0
v_{y0}	0.319422926485	0.346924570876
v_{z0}	0	0
T	4	3.215746906267

Table 4.1: Seed of the target halo orbit

The updated state vector is then propagated forward to evaluate the entire halo orbit. Given the periodic properties of this orbit, it is sufficient to integrate over one period T to determine the whole trajectory. A graphical representation of the halo is reported in Figure 4.1. The result is consistent with the contents of previous mission analyses [8, 21]. This orbit is then used to determine the emerging inner stable manifold.

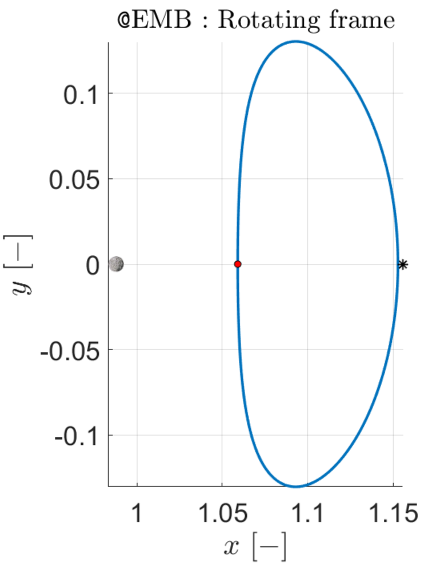

(a) View on the xy–plane.

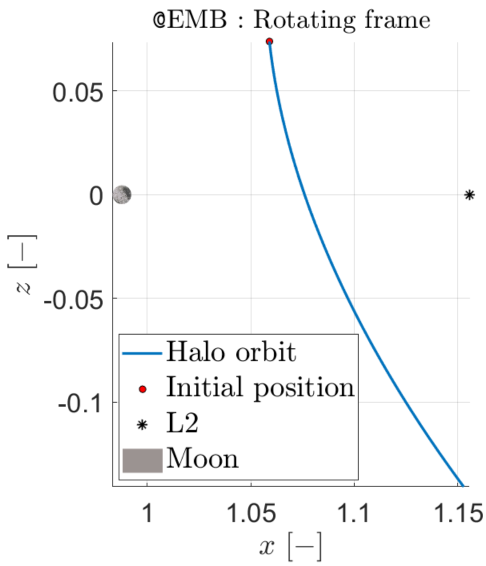

(b) View on the xz–plane.

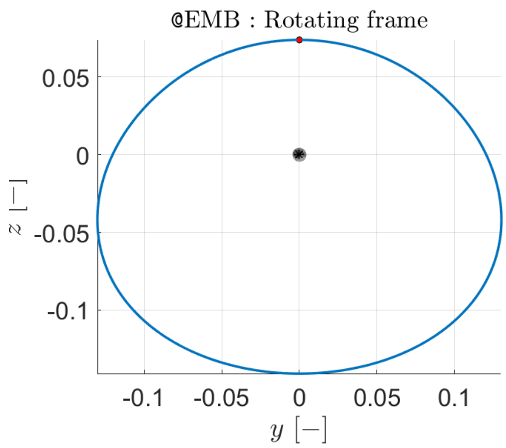

(c) View on the yz–plane.

Figure 4.1: Target halo with $C_j = 3.09$

4.1.1. Manifold Sampling

The manifold is computed with a fully numerical method, as described in Section 3.1.4. Initially, the monodromy matrix M associated with the halo orbit is evaluated to determine the stable eigenvectors. This matrix is equivalent to the STM determined over one period of the orbit. To reduce the computational effort, the monodromy matrix is computed only once in correspondence of the initial point $\mathbf{x}_0$:

$$M(\mathbf{x}_0) = \Phi(\mathbf{x}_0, 0; T)$$

The relative eigenvalue problem is solved and the stable direction $\boldsymbol{\nu}_{s,0}$ is retrieved. The latter is then propagated to any point along the orbit exploiting the STM, which is obtained solving the variational equations.

To begin the manifold sampling process, the halo orbit is divided into 200 points equally spaced in time. In correspondence of these samples, a small displacement $\varepsilon = 10^{-6}$ along the stable direction is applied. This perturbed condition is propagated backwards in time to determine this structure, as the trajectories laying on the stable branch tend asymptotically to the periodic solution. Thus, the stable manifold can be expressed as:

$$\mathbf{x}_{sm}(t_{po}, t_{sm}) = \varphi(\, \mathbf{x}_{po}(t_{po}) \pm \varepsilon\, \boldsymbol{\nu}_s,\, 0;\, -t_{sm}\,) \tag{4.1}$$

$$\text{with} \qquad \mathbf{x}_{po}(t_{po}) = \varphi(\, \mathbf{x}_0,\, 0;\, t_{po}\,) \qquad \text{and} \qquad \{\varepsilon, t_{sm}\} > 0$$

where the subscripts *po* and *sm* indicate quantities related to the periodic orbit and the corresponding stable manifold. In particular, two branches of this manifold emerge from the halo depending on the sign applied to the displacement. The inner part of the manifold is retrieved considering a negative sign in front of the perturbation ($-\varepsilon$), whereas the positive direction generates the outer one.

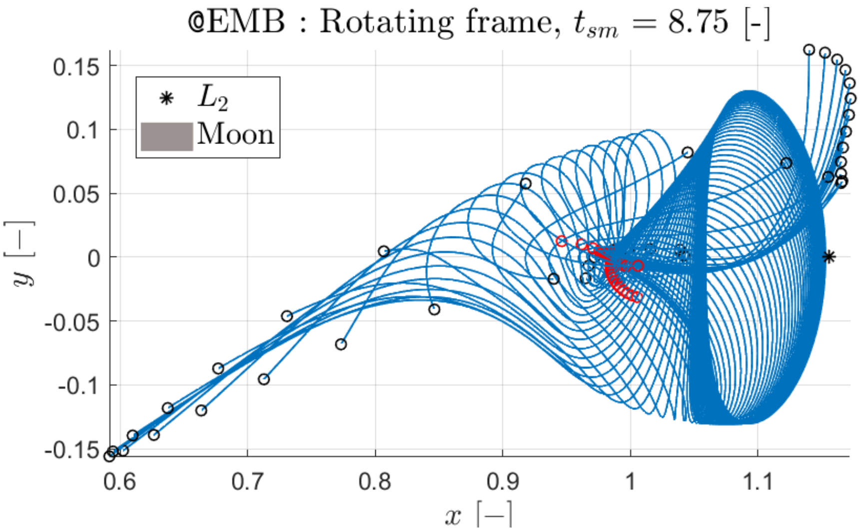

Figure 4.2: Stable inner manifold: the red points mark close encounters or impacts with the Moon' surface while the black points indicate the position at time t_{sm}

In this representation the manifold is composed only by 50 trajectories to improve readability. It can be noted that many trajectories approach the Moon and some of them even collide with its surface. To exploit the Obert effect, an impulsive maneuver would have to take place close to the pericenter of the parking orbit. Therefore, the points along the stable manifold, where the relative distance to the Moon is a local minima, are retained as possible initial guesses forming a dataset of close encounters. To determine those samples, an event function is used to precisely evaluate the point of minimum distance during the integration process without interrupting the solver. The condition is formulated as:

$$(\mathbf{r} - \mathbf{r}_m) \cdot (\mathbf{v} - \mathbf{v}_m) = 0 \tag{4.2}$$

where all these vectors are expressed in the synodic reference frame and the subscript m denotes quantities related to the Moon. This notation if further simplified noting that the primaries are at rest with respect to the synodic frame by definition. Using this event function, potential gravitational assists are considered if the trajectory exhibits multiple close encounters, as the integral continues after an event is detected.

A further stopping criterion is set to detect the crossing of a virtual sphere concentric with the Moon. This artificial structure is located at an altitude of 100 km above the equatorial radius $R_{B,m}$. The aim of this event function is to avoid continuing the numerical integration after an impact. Moreover, this points would be located in proximity of the pericenter of a possible parking orbit, where a more efficient maneuver could be achieved from the energetic stand point. This threshold is set based on the mean value of the admissible height at pericenter. This range and additional constraints on the parking orbit are introduced in the next section, where a second dataset is defined.

Manifold Interpolation

An approximation can be introduced to avoid computing the analytical stable inner manifold in each iteration step of the optimization problem. This structure can be described as a 2D surface dependent on two time coordinates (t_{po}, t_{sm}), as described in Eq. (4.1). Therefore, it is possible to determine a two–dimensional cubic convolution interpolation in these coordinates, following the methodology presented in [32]. Once the third order interpolation is computed, a non–linear correction step is applied to enforce a target energy level represented by the Jacobi constant of the original periodic orbit. In this case, the two time coordinates are defined on the intervals $t_{po} \in [0, T]$ and $t_{sm} \in [0, 10]$ and discretized into 400 equally spaced elements.

However, the maximum error of this interpolation is too high to be considered a feasible option for rapid evaluation of the manifold within the optimization problem, as reported in Figure 4.3. As expected, the errors achieve large values where the manifold separates into different branches after a close approach with the Moon, as shown in Figure 4.2. Therefore, this approach was later discarded.

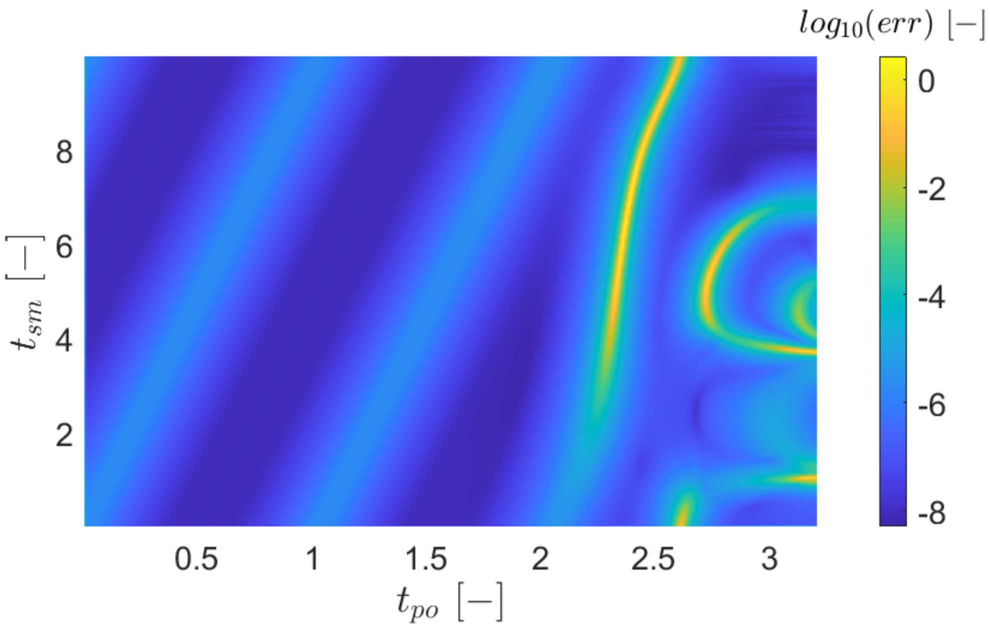

Figure 4.3: Maximum error committed by performing the manifold interpolation

4.1.2. Parking Orbit Sampling

The spacecraft is assumed to be injected on a selenocentric orbit by a mothercraft. The keplerian parameters used to define this conic are given in the Moon–Centered Moon–Equatorial frame (MCME2000). As the name suggests, this frame is centered at the Moon's barycenter. The z–axis is aligned the the Moon' spin axis on January 01, 2000, and the x–axis is aligned with the Earth mean equinox (γ–line). Then, the y–axis is defined to complete the right–handed frame. The admissible orbits are constrained by the upper and lower bounds displayed in Table 4.2 and 4.3, where h_p and h_a are the height from the Moon' surface measured at the pericenter and apocenter.

	h_p [km]	h_a [km]	i_0 [deg]	θ_0 [deg]
Lower bound	50	8000	85	0
Upper bound	150	80000	95	360

Table 4.2: Constraints on the orbital parameters in the MCME2000

Part of the orbital elements are defined on disjoint intervals, as reported in Table 4.3. For this reason, the optimization problem is going to be solved on 4 possible permutation of the upper and lower bounds.

	Interval 1	Interval 2
Ω_0 [deg]	$[80, 100]$	$[170, 190]$
ω_0 [deg]	$[140, 150]$	$[320, 330]$

Table 4.3: Constraints on the orbital parameters on disjoint intervals

The orbital parameters are then transformed into cartesian coordinates ($\mathbf{R}_{in}$, $\mathbf{V}_{in}$) according to the following equations:

$$\mathbf{R}_{in} = R_z(\Omega_0)R_x(i_0)R_z(\omega_0)\mathbf{R}_{perifocal} \tag{4.3}$$

$$\mathbf{V}_{in} = R_z(\Omega_0)R_x(i_0)R_z(\omega_0)\mathbf{V}_{perifocal} \tag{4.4}$$

where:

$$\mathbf{R}_{perifocal} = \frac{a(1-e^2)}{1+e\,cos(\theta_0)}\begin{bmatrix} cos(\theta_0) \\ sin(\theta_0) \\ 0 \end{bmatrix} \tag{4.5}$$

$$\mathbf{V}_{perifocal} = \sqrt{\frac{\mu_m}{a(1-e^2)}}\begin{bmatrix} -sin(\theta_0) \\ e+cos(\theta_0) \\ 0 \end{bmatrix} \tag{4.6}$$

where a is the semi–major axis; e is the eccentricity; and R is rotation matrix about the axis denoted in the subscript of an angle reported between parentheses.

Given these upper and lower bounds, it is easier to consider the orbital parameters as part of the optimization vector. Therefore, it is necessary to introduce a transformation between inertial and rotating coordinates. A small approximation is introduced by considering the synodic plane to be coincident with the equatorial plane of the MCME2000. In reality, they are inclined by approximately 6.5 degrees [27], thus introducing an error that is accepted at this stage of the optimization.

Based on this simplification, the mapping between the two frames is expressed as the combination of a translation with a rotation about a single axis. The first term depends on the position of the Moon in the CRTBP. The second contribution consists in a simple rotation about the z–axis, described by the constant angular velocity ω of the primaries. Therefore, this last term is computed as follows:

$$R_{in\to rot} = R_z^T(\omega(t-t_0)+\alpha(t_0)) \tag{4.7}$$

where α is the angle formed by the projection of Earth–Moon direction on the xy–plane of the MCME2000, measured counterclockwise from its x–axis; t is the nondimesional time; t_0 is a reference epoch at which the angle $\alpha(t_0) = 0$ rad.

The time expressed in seconds past J2000 (et) is converted into nondimensional units and later wrapped to the interval $[0, 2\pi]$, to normalize its value compared to the other angular quantities. Once an initial guess t_0 is determined, it is sufficient to consider the interval $[t_0,\, t_0 + 2\pi]$ to account for all possible configurations. Moreover, as the angular velocity in the nondimensional CRTPB has a unitary value, Eq. (4.7) can be rewritten as:

$$R_{in \to rot} = R_z^T(t - t_0) \qquad t \in [t_0,\, t_0 + 2\pi] \tag{4.8}$$

The position and velocity vectors in the inertial frame are then mapped into the nondimensional rotating coordinates $(\mathbf{r}_{rot},\, \mathbf{v}_{rot})$, as reported in the following equations:

$$\begin{aligned}
\mathbf{r}_{rot} &= \mathbf{o}_{in}^{(rot)} + R_{in \to rot} \frac{\mathbf{R}_{in}}{DU} \\
&= \mathbf{r}_{Moon}^{(rot)} + R_{in \to rot} \frac{\mathbf{R}_{in}}{DU} \\
&= [(1 - \mu), 0, 0]^T + R_{in \to rot} \frac{\mathbf{R}_{in}}{DU}
\end{aligned} \tag{4.9}$$

$$\begin{aligned}
\mathbf{v}_{rot} &= \mathbf{v}_{o_{in}}^{(rot)} + S([0, 0, 1]^T) R_{in \to rot} \frac{\mathbf{R}_{in}}{DU} + R_{in \to rot} \frac{\mathbf{V}_{in}}{VU} \\
&= S([0, 0, 1]^T) R_{in \to rot} \frac{\mathbf{R}_{in}}{DU} + R_{in \to rot} \frac{\mathbf{V}_{in}}{VU}
\end{aligned} \tag{4.10}$$

where $\mathbf{o}_{in}^{(rot)}$ is the position of the center of the inertial frame described in the synodic frame; $\mathbf{v}_{o_{in}}^{(rot)}$ is the velocity of the center of the inertial frame described in synodic coordinates; S is the skew matrix used to model the cross product in matrix notation; DU and VU are the scale lenght and velocity of the CRTBP.

After the coordinate transformation is introduced, a second sampling process is performed to discretize the parking orbits. In more detail, the orbital parameters are sampled in a finite number of points equally spaced along the intervals admitted by the constraints reported in Table 4.2 and 4.3. The number of samples retained for each variable is reported for completeness. In the case of variables with 2 intervals of validity, half of the points are retrieved from each of them.

	h_p	h_a	i_0	Ω_0	ω_0	θ_0	t
Number of samples	3	13	3	6	6	6	10

Table 4.4: Sampling of the orbital coordinates

All possible permutations of these parameters are considered and transformed into cartesian coordinates in the MCME2000 frame with Eqs. (4.3) and (4.4).

Lastly, this samples are mapped into rotating coordinates with Eqs. (4.9) and (4.10), thus forming a second dataset of points located on admissible parking orbits.

4.1.3. Representative Selection

To determine a feasible number of initial conditions, a filtering process in applied on the candidates contained in the two datasets. In particular, each sample of the stable manifold is tested against each sample belonging to the feasible parking orbits. The following threshold are implemented to retain only the most promising initial conditions:

$$||\mathbf{r}_{sm}(t_{po}, t_{sm}) - \mathbf{r}_{park}(h_p, h_a, i, \Omega, \omega, \theta, t)|| < 10^3\,\mathrm{km} \tag{4.11}$$

$$||\mathbf{v}_{sm}(t_{po}, t_{sm}) - \mathbf{v}_{park}(h_p, h_a, i, \Omega, \omega, \theta, t)|| < 1\,\mathrm{km/s} \tag{4.12}$$

The pairs ($\mathbf{x}_{sm}$, $\mathbf{x}_{park}$) that satisfy these inequalities are considered as potential candidates to set up the first iteration of the multiple shooting process. This initial conditions are stored as vectors containing the orbital parameters, the time t, and the two coordinates necessary to locate a point on a manifold (t_{po}, t_{sm}).

However, the number of points is considerably large to be employed without a further refinement. Therefore, it is possible to apply a k–medoids[1] clustering method to find the most representative candidates. These medoids are points part of the dataset itself and they are selected in order to minimize the normalized euclidean distance to the neighboring points. To avoid over sampling, the search for medoids is truncated in correspondence of the elbow in the graph reporting the Sum of the Squared Errors (SSE) as a function of the number of clusters.

[1]The `kmedoids` MATLAB function is utilized, setting the distance metric to Standardized Euclidean distance

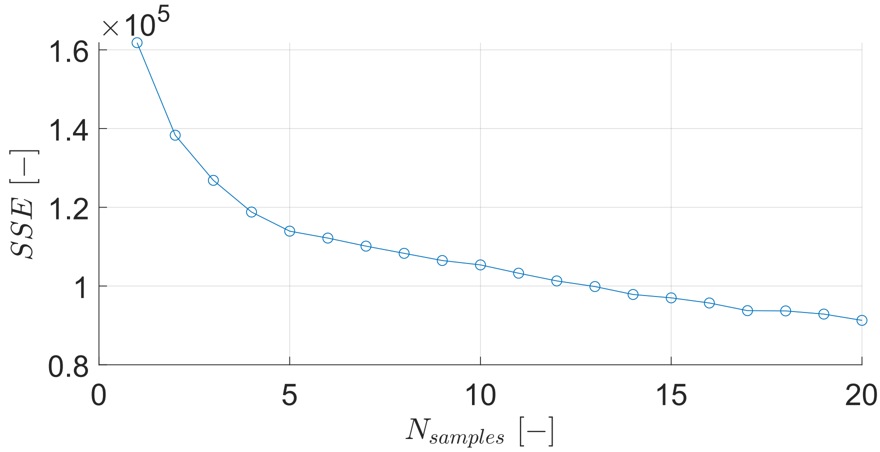

Figure 4.4: Sum of the Squared Errors in the k–medoids method

In the previous graph, the elbow is found in correspondence of 5 samples. However, 10 data–points are retained to create a larger dataset of initial conditions to find more potential candidates for the transfer trajectory. Based on this values, the initial conditions of the multiple shooting are retrieved by dividing the trajectory laying on the manifold in an arbitrary number of points equally spaced in time (t_{sm}). As the stable branch is computed with a back propagation, the order of the samples is then flipped to determine the structured optimization vector.

4.2. Problem statement

The transfer trajectory is determined with an optimization problem aimed at minimizing the fuel consumption. This problem is widely investigated in literature, given the substantial benefits introduced by lowering the necessary fuel mass carried onboard. In practical terms, this leads to a wider range of operational mission designs as well as extending the mass budget of other vital subsystems. To achieve this savings, a trajectory has to exploit the natural dynamics modeled by the equation of motion, especially in case of mission with limited Δv budgets like CubeSat based designs.

To solve the optimization problem, a direct method is adopted in this thesis for its stability and simplicity. It transforms the control law into discrete and impulsive maneuvers, thus mapping the problem into a nonlinear programming (NLP) framework.

In particular, the optimization problem is formulated as multiple–burn multiple–shooting. The trajectory has to satisfy a set of initial and final constraint ($\boldsymbol{\psi}_0$, $\boldsymbol{\psi}_f$), which enforce the departure and arrival conditions on certain orbits. The trajectory is divided in nodes subjected to a set of equality and inequality constraints. This nodes are then assigned into multiple arcs each divided in segments. An arc si defined as the portion of the trajectory delimited by two impulsive maneuvers, whereas a segment is a portion of an arc delimited by two nodes. The adopted multiple shooting is based on the formulation introduced in [13], where an high–fidelity optimization is developed in great detail.

In this case, the transfer is partitioned in n arcs formed by m nodes each. A generic nondimensional node is denoted as follows:

$$\mathbf{x}_k^{(j)} = \begin{bmatrix} \mathbf{r}_k^{(j)} \\ \mathbf{v}_k^{(j)} \end{bmatrix} \qquad \text{with} \qquad \begin{matrix} k = 1, ..., m \\ j = 1, ..., n \end{matrix} \tag{4.13}$$

where k is the index used to identify a node inside an arc; j is the index denoting a specific arc. Moreover, it is sufficient to introduce an initial and final time variable for each arc ($\tau_0^{(j)}$, $\tau_f^{(j)}$), as the times associated with the internal nodes are determined on an equally spaced grid of m points:

$$\tau_k^{(j)} = \tau_1^{(j)} + \frac{k-1}{m-1}(\tau_m^{(j)} - \tau_1^{(j)}) \qquad \text{with} \qquad \begin{matrix} k = 1, ..., m \\ j = 1, ..., n \end{matrix} \tag{4.14}$$

This values are expressed in nondimensional units starting from a reference time $\tau_1^{(1)} = 0$, that is not part of the optimization vector.

A total of n+1 maneuvers would be expected, instead the impulse between the last arc and the manifold itself is transformed into a full continuity constraint. This formulation leads to better–conditioned derivatives of the objective function J and to a smother convergence.

Additional variables are introduced to fully define the NLP formulation:

- time coordinates needed to identify a point along the manifold (t_{po}, t_{sm})
- normalized orbital parameters $\mathbf{y}_{park} = [r_p/DU,\ r_a/DU,\ i_0,\ \Omega_0,\ \omega_0,\ \theta_0]$, where DU is the scale length of the CRTPB and (r_p, r_a) are the radius of pericenter and apocenter of the parking orbit
- the departure time from the parking orbit (t_{park}) used to map the coordinates from the MCME2000 to the rotating frame
- a set of regularized variables ($\mathbf{U}_j$) based on Kustaanheimo–Stiefel transformation [28], three for each impulsive maneuver

As a result the optimization vector can be expressed as:

$$\mathbf{y} = (\mathbf{x}_k^{(j)},\, \mathbf{U}_j,\, \tau_f^{(1)},\, \tau_0^{(l)},\, \tau_f^{(l)},\, \mathbf{y}_{park},\, t_{park}, t_{po}, t_{sm}) \tag{4.15}$$

$$\text{with} \quad \begin{aligned} k &= 1, ..., m \\ j &= 1, ..., n \\ l &= 2, ..., n \end{aligned}$$

Thus, the trajectory optimization problem can be treated as a NLP in the variables $\mathbf{y}$, subject to a set of equality ($\mathbf{g}$) and inequality constraints ($\mathbf{h}$):

$$\min_{\mathbf{y}} J(\mathbf{y}) \qquad \text{s.t.} \quad \begin{cases} \mathbf{g}(\mathbf{y}) = \mathbf{0} \\ \mathbf{h}(\mathbf{y}) \leq \mathbf{0} \end{cases} \tag{4.16}$$

In practical terms, the problem is solved with MATLAB `fmincon` with the interior point algorithm [5], exploiting the analytical derivatives of the objective function and of the constraints. In particular, this formulation of the problem is strongly influenced by the initial barrier parameter (γ_0) [28]. After some test runs, this value was set to 10^{-10}.

4.2.1. Objective Function

The problem is based on a fuel optimal formulation. Accordingly, the objective function $J(\mathbf{y})$ would be defined as the sum of the magnitude of each maneuver:

$$J(\mathbf{y}) = \sum_{j=1}^{N-1} ||\Delta\mathbf{v}_j|| + ||\Delta\mathbf{v}_0|| = \sum_{j=1}^{N-1} ||\mathbf{v}_1^{(j+1)} - \mathbf{v}_m^{(j)}|| + ||\mathbf{v}_1^{(1)} - \mathbf{v}_{park}|| \tag{4.17}$$

However, this form presents singular derivatives when $||\Delta\mathbf{v}_j|| = 0$:

$$\frac{\partial ||\Delta\mathbf{v}_j||}{\partial \mathbf{v}_1^{(j+1)}} = \frac{\Delta\mathbf{v}_j^T}{||\Delta\mathbf{v}_j||} \quad \text{and} \quad \frac{\partial ||\Delta\mathbf{v}_j||}{\partial \mathbf{v}_m^{(j)}} = -\frac{\Delta\mathbf{v}_j^T}{||\Delta\mathbf{v}_j||} \tag{4.18}$$

To avoid numerical instabilities in the Jacobian of the objective function, the problem is often mapped into an energy optimal formulation. To achieve this form, $J(\mathbf{y})$ is expressed as the sum of the squares of magnitudes of each maneuver $||\Delta\mathbf{v}_j||$. However, this does not ensure the minimization of the Δv required by the mission, which can be an issue for multiple shooting methods involving a large number of maneuvers and a tight budget.

For this reason, a set of regularized variables $\mathbf{U}_j = [u_j, w_j, s_j]^T$ is introduced to map the original fuel optimal problem into a singularity–free formulation. This method was presented recently in [28], with the aim of removing possible singularities associated with null thrust impulses. These regularized variables are based on the Kustaanheimo–Stiefel transformation, which is the three dimensional extension of the Levi–Civita transformation [6]. Accordingly, each impulse is mapped by the following equations:

$$\Delta\mathbf{v}_j = \begin{bmatrix} \Delta v_{xj} \\ \Delta v_{y,j} \\ \Delta v_{z,j} \end{bmatrix} = \begin{bmatrix} u_j^2 - w_j^2 - s_j^2 \\ 2u_j w_j \\ 2u_j s_j \end{bmatrix} \tag{4.19}$$

These equations can be used to determine the regularized variables (u_j, w_j, s_j) in every case except when $\Delta v_{xj} < 0$ & $\Delta v_{yj} = \Delta v_{zj} = 0$. By rearranging the terms, a second formulations is developed in this particular instance:

$$\Delta\mathbf{v}_j = \begin{bmatrix} \Delta v_{xj} \\ \Delta v_{yj} \\ \Delta v_{zj} \end{bmatrix} = \begin{bmatrix} 2u_j w_j \\ u_j^2 - w_j^2 - s_j^2 \\ 2u_j s_j \end{bmatrix} \tag{4.20}$$

This map can be inverted to retrieve the value of the regularized variables during the definition of the initial guess vector. As a result, it is possible to transform the objective function (Eq. 4.17) into a convex formulation:

$$J(\mathbf{y}) = \sum_{j=1}^{n-1}(u_j^2 + w_j^2 + s_j^2) + (u_0^2 + w_0^2 + s_0^2) = \sum_{j=1}^{n-1} ||\mathbf{U}_j||^2 + ||\mathbf{U}_0||^2 \tag{4.21}$$

This form is adopted in this thesis as it provides precise derivatives still minimizing the required Δv budget:

$$\frac{\partial J}{\partial \mathbf{U}_j} = 2\mathbf{U}_j^T \tag{4.22}$$

The rest of the terms of the Jacobian are null, thus the matrix is saved as sparse to improve the computational efficiency. Additional constraints are required to enforce the map between the two set of coordinates, otherwise the regularized variables do not represent the magnitude of the single impulse:

$$\mathbf{\Gamma}_j = \mathbf{v}_1^{(j+1)} - \mathbf{v}_m^{(j)} - \begin{bmatrix} u_j^2 - w_j^2 - s_j^2 \\ 2u_j w_j \\ 2u_j s_j \end{bmatrix} = \mathbf{0} \tag{4.23}$$

In the case in which Eq. (4.20) is adopted, the constraint becomes:

$$\mathbf{\Gamma}_j = \mathbf{v}_1^{(j+1)} - \mathbf{v}_m^{(j)} - \begin{bmatrix} 2u_j w_j \\ u_j^2 - w_j^2 - s_j^2 \\ 2u_j s_j \end{bmatrix} = \mathbf{0} \tag{4.24}$$

In particular for the departure maneuver, the equation becomes:

$$\mathbf{\Gamma}_0 = \mathbf{v}_1^{(1)} - \mathbf{v}_{park} - \begin{bmatrix} u_j^2 - w_j^2 - s_j^2 \\ 2u_j w_j \\ 2u_j s_j \end{bmatrix} = \mathbf{0} \tag{4.25}$$

or in the second formulation obtained by inverting the first and second row of the column vector, as reported in Eq. (4.24).

4.2.2. Constraints

The NLP problem is completed by a set of equality and inequality constraints. In particular, the upper and the lower bounds on the optimization variables are expressed as input vectors fed to the solver. In the current notation, they are denoted as (lb, ub). The bounds related to the orbital parameters are already stated in Table 4.2 and 4.3. After some test runs, it was evident that the maximum radius of pericenter was too large, leading to solutions where the parking orbit became an open trajectory. Therefore, the upper limit is scaled down to $ub(r_a) = (6 \cdot 10^4 + R_{B,m})$ km, where $R_{B,m}$ denotes the equatorial radius of the Moon.

The additional bounds are reported below:

	t_{park} [-]	t_{po} [-]	t_{sm} [-]
Lower bound	t_0	0	-18
Upper bound	$t_0 + 2\pi$	T	0

Table 4.5: Upper and lower bounds applied to the NLP

For the remaining variables ($\mathbf{x}_k^{(j)}$, $\mathbf{U}_j$, $\tau_f^{(1)}$, $\tau_0^{(l)}$, $\tau_f^{(l)}$), the bounds are set to large values $[-1000, +1000]$ in order to limit possible divergent behavior. Moreover, the bounds must be expressed in the same units as the associated optimization variables. As a results the angles reported in Table 4.2 and 4.3 are transformed in radians and the radii of pericenter and apocenter are computed in nondimensional units.

Inequality Constraints

The inequality constraints $\mathbf{h}$ arise from operational requirements. A minimum time difference between two consecutive maneuvers has to be guaranteed to conduct the orbit determination (OD) campaign and to recompute the maneuver on ground. Based on previous reports on the LUMIO mission, the minimum time between each nominal thrust impulse is set to be 3 days, which is denoted as $\Delta\tau_{min}$ in nondimensional units. In addition, a maximum transfer duration is imposed to avoid solutions requiring a long time of flight, which leads to a reduced lifespan once the spacecraft reaches the operational orbit. As a result, the vector containing all the inequality constrains is defined as:

$$\mathbf{h}(\mathbf{y}) = \begin{bmatrix} \tau_1^{(j)} - \tau_m^{(j)} + \Delta\tau_{min} \\ \tau_1^{(1)} - \tau_m^{(n)} - \Delta\tau_{max} \end{bmatrix} \qquad \text{with} \quad j = 1, ..., n \tag{4.26}$$

The derivatives of these linear constraints are omitted for brevity. The Jacobian matrix is sparse, containing only ± 1 terms in correspondence of the involved time coordinates.

An additional constraint is initially introduced to define the maximum cost of a single maneuver to ease a finite impulse mapping. This process is a common refinement step of an impulsive solution, which is not addressed in this thesis. According to the mission requirements listed in Table 2.2, the maximum value for a single $||\Delta\mathbf{v}_j||$ is set to 30 m/s.

However, this constraint significantly affects the ability of the solver to converge to a solution, therefore is not considered in the NLP problem. In addition, it seemed unnecessary to over–constrain the first step in the optimization process, thus possibly limiting the solutions determined in the higher–fidelity models. This constraint is applied a posteriori to the final results of the optimization process in the RnBP to rule out unfeasible solutions.

Equality Constraints

The equality constraints are divided into continuity conditions, boundary constraints and coordinate transformations introducing the map required by the regularized variables to maintain a fuel optimal formulation.

Full continuity within each arc

Each node represents the initial condition of a single segment propagated forward in time with the flow operator. Since each arc is a ballistic trajectory by definition, it is necessary to enforce a full continuity on position and velocity:

$$\boldsymbol{\zeta}_k^{(j)} = \varphi(\mathbf{x}_k^{(j)},\, \tau_k^{(j)};\, \tau_{k+1}^{(j)}) - \mathbf{x}_{k+1}^{(j)} = \mathbf{0} \qquad \text{with} \qquad \begin{array}{l} k = 1, ..., m-1 \\ j = 1, ..., n \end{array} \tag{4.27}$$

Position continuity between arcs

As maneuvers are located between different arcs, it is sufficient to apply a position continuity at the boundary nodes. This constraint paired with the previous one ensures a continuous trajectory if satisfied with the imposed tolerance.

$$\boldsymbol{\psi}_j = \mathbf{r}_m^{(j)} - \mathbf{r}_1^{(j+1)} = \mathbf{0} \qquad \text{with} \qquad j = 1, ..., n-1 \tag{4.28}$$

Time continuity between arcs

One additional constraint is required to enforce the time continuity between different arcs. This becomes more relevant in a time dependent system such as the RnBP. However, this is already introduced in the trajectory optimization based on the CRTBP to obtain continuous time coordinates. Therefore, they are easily mapped into the corresponding value in the higher–fidelity problem.

$$\sigma_j = \tau_m^{(j)} - \tau_1^{(j+1)} = 0 \qquad j = 1, ..., n-1 \tag{4.29}$$

Initial boundary constraint

The spacecraft is assumed to be located on a lunar parking orbit, expressed as a function of the keplerian parameters $\mathbf{y}_{park} = [r_p/DU,\, r_a/DU,\, i_0,\, \Omega_0,\, \omega_0,\, \theta_0]$ in the MCME2000 reference frame. In this formulation, the target condition is converted in cartesian coordinates expressed in the rotating frame $\mathbf{x}_{park} = [\mathbf{r}_{park},\, \mathbf{v}_{park}]^T$. Since an impulsive maneuver at departure is allowed, the initial boundary constraint is expressed as position continuity.

$$\boldsymbol{\psi}_0 = \mathbf{r}_{park}(\mathbf{y}_{park}) - \mathbf{r}_1^{(1)} = \mathbf{0} \tag{4.30}$$

where

$$\mathbf{r}_{park} = [(1-\mu), 0, 0]^T + R_{in\to rot}\,\frac{\mathbf{R}_{in}}{DU} \tag{4.31}$$

$$\mathbf{R}_{in} = R_z(\Omega_0) R_x(i_0) R_z(\omega_0)\,\frac{a(1-e^2)}{1+e\,cos(\theta_0)} \begin{bmatrix} cos(\theta_0) \\ sin(\theta_0) \\ 0 \end{bmatrix} \tag{4.32}$$

Final boundary constraint

The final condition is computed as a point belonging to the stable inner manifold emerging from the target halo orbit. This point is expressed as a function of two time coordinates $(t_{po},\, t_{sm})$, once the initial seed of the halo is determined $\mathbf{x}_{po,0}$. In this instance, the constraint is defined as full continuity over the position and velocity coordinates.

$$\boldsymbol{\psi}_f = \mathbf{x}_m^{(n)} - \varphi(\mathbf{x}_{sm,0},\, 0;\, t_{sm}) = 0 \qquad \text{where} \quad t_{sm} \leq 0 \tag{4.33}$$

with

$$\mathbf{x}_{sm,0} = \varphi(\mathbf{x}_{po,0},\, 0;\, t_{po}) - \varepsilon\, \boldsymbol{\nu}_s(t_{po}) \tag{4.34}$$

$$\boldsymbol{\nu}_s(t_{po}) = \frac{\Phi(\mathbf{x}_{po,0},\, 0;\, t_{po})\, \boldsymbol{\nu}_{s,0}}{||\Phi(\mathbf{x}_{po,0},\, 0;\, t_{po})\, \boldsymbol{\nu}_{s,0}||} \tag{4.35}$$

where $\mathbf{x}_{sm,0}$ is the initial position along the manifold; $\mathbf{x}_{po,0}$ is the initial position along the the halo, determined in Section 4.1; $\boldsymbol{\nu}_{s,0}$ is the stable eigen direction computed in correspondence of $\mathbf{x}_{po,0}$. It is worth noting that the STM is used to propagate the stable direction to the desired time t_{po}. However, this process does not preserve the unitary length of such vector, thus requiring a successive normalization (Eq. 4.35).

Mapping of the regularized variables

Lastly, a set of equations are used to map the coordinates of each $\Delta\mathbf{v}_j = [\Delta v_{x_j}, \Delta v_{y_j}, \Delta v_{z_j}]^T$ into the regularized variables $\mathbf{U}_j = [u_j,\, w_j,\, s_j]^T$, as reported in Eqs. (4.23), (4.24) and (4.25). To completely define $\boldsymbol{\Gamma}_0$ in Eq. (4.25), $\mathbf{v}_{park}$ is obtained with the following transformation:

$$\mathbf{v}_{park} = S([0,0,1]^T) R_{in\to rot} \frac{\mathbf{R}_{in}}{DU} + R_{in\to rot} \frac{\mathbf{V}_{in}}{VU} \tag{4.36}$$

$$\text{where} \quad \mathbf{V}_{in} = R_z(\Omega_0) R_x(i_0) R_z(\omega_0) \sqrt{\frac{\mu_m}{a(1-e^2)}} \begin{bmatrix} -sin(\theta_0) \\ e + cos(\theta_0) \\ 0 \end{bmatrix} \tag{4.37}$$

Complete set of equality constraint

The complete vector modeling the equality constraint is reported hereafter:

$$\mathbf{g}(\mathbf{y}) = (\boldsymbol{\zeta}_k^{(j)},\, \boldsymbol{\psi}_j,\, \sigma_j,\, \boldsymbol{\psi}_0,\, \boldsymbol{\psi}_f, \boldsymbol{\Gamma}_0,\, \boldsymbol{\Gamma}_i) = \mathbf{0} \qquad \text{with} \quad \begin{aligned} i &= 1, ..., n-1 \\ j &= 1, ..., n \\ k &= 1, ..., m-1 \end{aligned} \tag{4.38}$$

As the rest of the Jacobian matrices, the one related to the equality conditions is extremely sparse and modular:

$$\mathcal{G}_{eq} = \begin{bmatrix} \frac{\partial \boldsymbol{\zeta}_k^{(j)}}{\partial \mathbf{x}_k^{(j)}} & 0 & \frac{\partial \boldsymbol{\zeta}_k^{(j)}}{\partial \tau\tau} & 0 & 0 & 0 & 0 \\ \frac{\partial \boldsymbol{\psi}_j}{\partial \mathbf{x}_k^{(j)}} & 0 & 0 & 0 & 0 & 0 & 0 \\ 0 & 0 & \frac{\partial \sigma_j}{\partial \tau\tau} & 0 & 0 & 0 & 0 \\ \frac{\partial \boldsymbol{\psi}_0}{\partial \mathbf{x}_k^{(j)}} & 0 & 0 & \frac{\partial \boldsymbol{\psi}_0}{\partial \mathbf{y}_{park}} & \frac{\partial \boldsymbol{\psi}_0}{\partial t_{park}} & 0 & 0 \\ \frac{\partial \boldsymbol{\psi}_f}{\partial \mathbf{x}_k^{(j)}} & 0 & 0 & 0 & 0 & \frac{\partial \boldsymbol{\psi}_f}{\partial t_{po}} & \frac{\partial \boldsymbol{\psi}_f}{\partial t_{sm}} \\ \frac{\partial \boldsymbol{\Gamma}_0}{\partial \mathbf{x}_k^{(j)}} & \frac{\partial \boldsymbol{\Gamma}_0}{\partial \mathbf{U}_j} & 0 & 0 & 0 & 0 & 0 \\ \frac{\partial \boldsymbol{\Gamma}_i}{\partial \mathbf{x}_k^{(j)}} & \frac{\partial \boldsymbol{\Gamma}_i}{\partial \mathbf{U}_j} & 0 & 0 & 0 & 0 & 0 \end{bmatrix} \tag{4.39}$$

$$i = 1, ..., n-1$$
$$j = 1, ..., n$$
$$k = 1, ..., m-1$$

where the vector $\tau\tau = [\tau_m^{(1)}, \tau_1^{(j)}, \tau_m^{(j)}]^T$ is introduced to simplify the notation. A more detailed version of the derivatives is reported in Appendix A.

5 | Impulsive Trajectory Optimization in Higher Fidelity Models

In this chapter, the methodology adopted in the solution refinement process is introduced. A gradual increase in the model complexity has proven successful in refining trajectories, as described in [11]. In this article, several gravitational models are defined in a hierarchical order, from the CRTBP up to the RnBP. The aim is to exploit a successive refinement approach to find intermediate solutions, enabling an higher convergence rate in the optimization problem.

Similarly, the transfers determined in the CRTBP in this thesis are used as initial guesses for a second trajectory optimization carried out in the RnBP–RPF, which is then divided in the following steps:

1. The previous solution is extended considering the parking orbit and the trajectory along the manifold as additional arcs of the multiple shooting. Then, the nodes and time coordinates are mapped in the nondimensional units adopted in RnBP.
2. A first optimization in conducted in the RnBP–RPF, considering as a final boundary constraint the target halo computed in the CRTBP. As a result, a more precise estimate of the Halo Insertion Maneuver (HIM) in retrieved.
3. A quasi–halo is determined based on the epoch time and node corresponding to the HIM computed at the previous step.
4. A second optimization is carried out using the quasi–halo as final boundary constraint, starting from the solution achieved at the second step.
5. The final refinement is conducted propagating the parking orbit with the planetocentric –RnBP model to reduce the computation time. This was essential to achieve low integration tolerances required to reduce the constraint tolerances.

5.1. Mapping of the initial guesses

The initial guesses for the next optimization step are retrieved by modifying the solutions computed in the CRTBP. These variations depend on three main aspects: the validity of the keplerian assumption for the parking orbit, the lack of a manifold structure in the RnBP–RPF and the necessity to transform the coordinates of the nodes in the new model. These aspects are addressed in more detail in the next sections.

Parking Orbit Stability

In the previous chapter, the parking orbit is assumed to be a conic with constant keplerian parameters, thus eliminating the need for a numerical integration. To verify this approximation, a stability analysis is conducted on the optimized parking orbits. The departure point is propagated backwards in time to determine the variation in the keplerian elements. Due to the high nonlinearities, all the trajectories deviate significantly from a conic orbit is a few days, as reported in Figure 5.1.

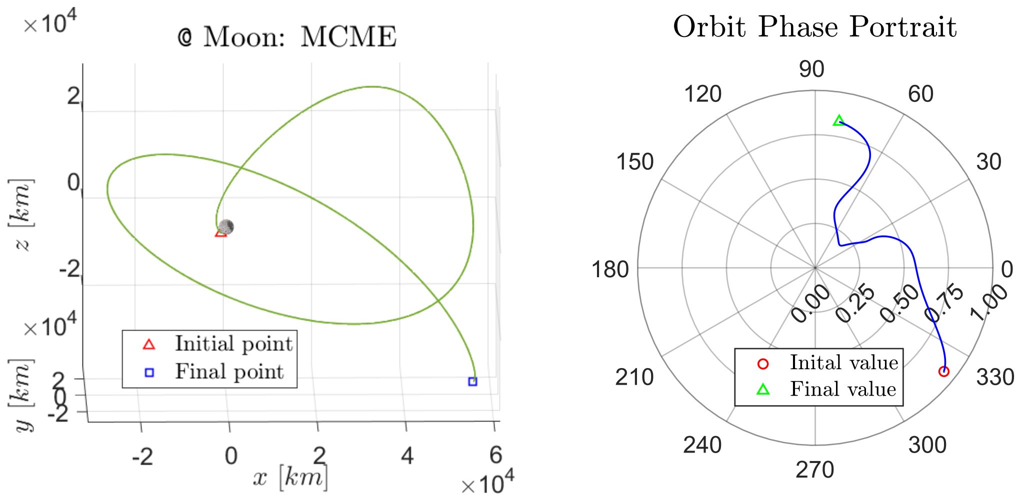

(a) View in the inertial frame.

(b) The eccentricity e and argument of pericenter $\omega(t)$ coincide with the radial and angular coordinates.

Figure 5.1: Example of a parking orbit propagated for 15 days

To solve this problem the Elliptic Lunar Frozen Orbits (ELFO) were considered as potential stable orbits. They are particular solutions determined with perturbation theory applied to lunar orbits, using the third body acceleration caused by Earth to stabilize the dynamics [16]. These orbits are expressed in the Earth Orbit (EO) frame, which is a convenient frame used to average the perturbing term [14], and are found only for specific values $\omega_{EO} = 90$ deg or 270 deg. The rotation between this frame and the MCME2000 determines small variations in the value of the argument of pericenter, thus they are assumed equal for simplicity ($\omega_{EO} \approx \omega_{MCME}$). However, these values are outside of the admissible intervals considered in this thesis, as reported in Table 4.3. Moreover, this theory is more suitable in case of smaller and less eccentric orbits with respect to the one considered in this optimization. For these reason, the ELFO were discarded.

As a result, it is not possible to model the initial boundary constraint without actually propagating the parking orbit as any other arc of the trajectory. Therefore, the solution computed in the CRTBP is augmented considering the parking orbit as an additional arc in the NLP problem. This is achieved by sampling the trajectory obtained by back–propagating the optimized departure point on the parking orbit over a time span of 7 days. This amount of time coincides with the minimum duration of this phase, according to mission requirements. In particular, this constraint depends on the maximum commissioning time of each subsystem, which has to take place before any scheduled maneuver.

Manifold Adaptation

The solutions in the CRTBP exploit the inner stable manifold to define the final boundary constraint. However, this structure does not exist in a strict sense outside the CRTBP. Therefore, the previous trajectory along the manifold is sampled and converted as the final arc in the new NLP problem. An additional Halo Injection Maneuver (HIM) is considered in the updated formulation. This is approximated to a null value in the guess vector, due to the small displacement ($\varepsilon = 10^{-6}$) introduced to compute the manifold in the first place.

Coordinate Transformation

Then, the augmented solution is directly mapped in the RnBP–RPF, due to the similarities in the definition of the rotating frames. Therefore, the position and velocity of the nodes are left unchanged:

$$\mathbf{x}_k^{(j)} = \begin{bmatrix} \mathbf{r}_k^{(j)} \\ \mathbf{v}_k^{(j)} \end{bmatrix} = \begin{bmatrix} \boldsymbol{\rho}_k^{(j)} \\ \boldsymbol{\eta}_k^{(j)} \end{bmatrix} \tag{5.1}$$

where $\boldsymbol{\rho}_k^{(j)}$ and $\boldsymbol{\eta}_k^{(j)}$ are the nondimensional position and velocity vectors defined in the RnBP–RPF. However, the time coordinates need a transformation to be mapped in the higher fidelity model. In the previous chapter, the nondimensional times ($\tau_k^{(j)}$) are measured starting from the first node, that is assumed as a reference $\tau_1^{(1)} = 0$. Consequently, the internal nodes are easily associated with a new time coordinate once the initial time is shifted properly. To determine such value, it is worth noting the chain of dependencies involving the time coordinates:

$$\tau_k^{(j)} \rightarrow \tau_1^{(1)} \rightarrow t_{park} \rightarrow t_0 \tag{5.2}$$

where $\tau_1^{(1)}$ represents the same time as t_{park}, simply translated to the origin on the time axis. Instead, t_{park} and t_0 are nondimensional times employed to model the relative rotation between the MCME2000 and the synodic frame, that is reported for clarity:

$$R_z(t_{park} - t_0)$$

This transformation is directly involved in the definition of the initial boundary condition $\boldsymbol{\psi}_0(t_{park})$, as reported in Eq. (4.30). As a result, it is sufficient to determine the value of t_0 in the time window of interest to compute all the other epoch times by following the chain dependencies in reverse order. Then, it is convenient to exploit the definition of t_0:

$$\alpha(t_0) = 0$$

where α is the angle formed by the projection of Earth–Moon direction on the xy–plane of the MCME2000, measured counterclockwise from its x–axis. This becomes a zero finding problem solved with the MATLAB function `fsolve`, in which the position of the celestial objects retrieved from the ephemerides. Considering the current mission development, the time window of interest for the LUMIO mission spans the entire year 2029. Lastly, the time coordinates are finally expressed as days past 1 January 2029 and later transformed in non dimensional units, as reported in Eq. (3.53).

5.2. Problem statement

The trajectory optimization in the higher fidelity model is transcribed in a NLP problem, as in the previous chapter. The notation is slightly different to introduce additional variables and constraints. Nevertheless, the core of the formulation is equal to the one utilized in Chapter 4. The problem is treated as a multiple shooting with multiple maneuvers, modeled with the aid of the Kustaanheimo–Stiefel regularized variables ($\mathbf{U}_j$) [28]. The trajectory is thus divided in n arcs each composed by m nodes, following the notation introduced in [13]. This allows to exploit the parallel computing to propagate the trajectories of multiple arcs at the same time, depending on the number of available cores.

Instead, the parking orbit is considered as a separate arc giving the possibility to select a different number of nodes m_{park}. This can be exploited to improve the computation time required to propagate the lunar orbit, which is the most demanding numerical integration. Indeed, the RnBP–RPF is not efficient in determining trajectories close to one of the primaries, since the dynamics becomes sensitive to small variations in the position of the spacecraft. As a result, the variable step integrator needs more intermediate evaluations to achieve an high degree of precision. By dividing the trajectory into multiple segments, it is possible to exploit parallel computing to determine them simultaneously, reducing the computation time.

After the initial conditions are correctly mapped in the new formulation, the optimization vector becomes:

$$\mathbf{y} = (\mathbf{x}_k^{(j)},\, \mathbf{U}_j,\, \tau_0^{(j)},\, \tau_f^{(j)},\, \mathbf{y}_{park},\, \mathbf{x}_{park}^{(l)},\, \tau_{park,0},\, t_{po}) \qquad \text{with} \quad \begin{array}{l} k = 1, ..., m \\ j = 1, ..., n \\ l = 1, ..., m_{park} \end{array} \tag{5.3}$$

where $\mathbf{x}_{park}^{(l)}$ denotes the generic node belonging to the parking orbit. Moreover, the times associated with the internal nodes of the parking orbit are determined on an equally spaced grid of m_{park} points, in continuity with the rest of the arcs:

$$\tau_{park}^{(l)} = \tau_{park,0} + \frac{l-1}{m_{park}-1}(\tau_1^{(1)} - \tau_{park,0}) \qquad \text{with} \quad \begin{array}{l} l = 1, ..., m_{park} \\ j = 1, ..., n \end{array} \tag{5.4}$$

The NLP problem is solved by determining the optimization variables $\mathbf{y}$ that minimize an objective function J, subject to a set of equality and inequality constraints, denoted respectively as $\mathbf{g}$ and $\mathbf{h}$. In continuity with the previous notation, the problem is expressed as:

$$\min_{\mathbf{y}} \; J(\mathbf{y}) \qquad \text{s.t.} \quad \begin{cases} \mathbf{g}(\mathbf{y}) = \mathbf{0} \\ \mathbf{h}(\mathbf{y}) \leq \mathbf{0} \end{cases} \tag{5.5}$$

where both the objective function and the constraints present variations with respect to the formulation expressed in Section 4.2. These differences are going to be presented in more detail in the following sections.

As in the previous chapter, the problem is solved with MATLAB `fmincon` with the interior point algorithm [5]. The optimization problem modeled in the RnBP–RPF is even more susceptible to initial value of the barrier parameter (γ_0). This value could be decreased if the solver struggles to converge given a certain initial condition. As a rule of thumb the barrier parameter should be lower than 10^{-4}, based on accumulated experience. Moreover, the analytical derivatives are provided to the solver to aid the convergence of the algorithm. This is done exploiting the variational equations to retrieve the STMs that are frequently involved in this Jacobian matrices.

Objective Function

The objective function is modified to account for the time variable nondimensionalization of the RnBP–RPF. Therefore, it is necessary to convert the magnitude of each impulsive maneuver into dimensional units to avoid adding terms scaled according to different time dependent quantities ($k(\tau_k^{(j)})$).

$$J(\mathbf{y}) = \sum_{j=1}^{n-1} \omega k(\tau_{\text{avg}}^{(j)}) \|\mathbf{U}_j\|^2 \ + \ \omega k(\tau_1^{(1)}) \|\mathbf{U}_0\|^2 \ + \ \omega k(\tau_m^{(n)}) \|\mathbf{U}_{\text{HIM}}\|^2 \tag{5.6}$$

$$\text{where} \quad \|\mathbf{U}_j\| = \left(u_j^2 + w_j^2 + s_j^2\right) \qquad \text{and} \quad \tau_{\text{avg}}^{(j)} = \frac{\tau_1^{(j+1)} + \tau_m^{(j)}}{2}$$

The average nondimensional time ($\tau_{\text{avg}}^{(j)}$) is introduced to aid the convergence of the solver, in case the time continuity between the different arcs is not strictly observed in an intermediate step of the algorithm.

The objective function is modeled with the regularized variables ($\mathbf{U}_j$), trying to extend the NLP formulation expressed in [28] to a higher fidelity model. In addition, the derivatives of the objective function J are provided in Appendix B.

Linear Boundary Constraints

The `fmincon` solver allows to define a set of upper and lower bounds on the optimization variables. In particular, they are slightly modified from the ones reported Section 4.2.2. Part of the variables of the previous notation are excluded from the updated optimization vector $\mathbf{y}$ with their relative constraints (t_{park}, t_{sm}) . Additional upper and lower bounds are defined for the nodes of the parking orbit $\mathbf{x}_{park}^{(l)}$. They are set to large values to avoid constraining the optimization. Instead, a upper and lower limit is imposed on the initial time along the parking orbit to restrict the search interval on the first few months of the year:

$$\tau_{park,0} \in [0, 15] \tag{5.7}$$

Inequality Constraints

Regarding the inequality constraints, the only variation consists in an additional condition, set to impose a minimum time span of the parking orbit. This limit is introduced to determine solutions which allow the commissioning of all subsystems before any maneuver can take place. This series of procedures must be completed within 7 days from the release of the CubeSat from the mothercraft, according to mission constraints. Assuming that LUMIO will be released directly into the parking orbit, this phase of the mission shall last at least the maximum required time by the commissioning process ($\Delta\tau_{park,min}$). The complete vector containing the inequality constraints is reported:

$$\mathbf{h}(\mathbf{y}) = \begin{bmatrix} \tau_1^{(j)} - \tau_m^{(j)} + \Delta\tau_{min} \\ \tau_1^{(1)} - \tau_m^{(n)} - \Delta\tau_{max} \\ \tau_{park,0} - \tau_1^{(1)} + \Delta\tau_{park,min} \end{bmatrix} \qquad \text{with} \quad j = 1, ..., n \tag{5.8}$$

This relations are linearly dependent on part of the optimization variables. Thus, the Jacobian of the inequality constraints can be easily derived.

Equality Constraints

The equality constraints are based on the formulation presented in Section 4.2.2. Therefore, they are going to be listed briefly to highlight the variations. Moreover, additional continuity constraints are introduced at parking orbit nodes.

Full continuity within each arc:
A full position and velocity continuity is imposed within each arc:

$$\boldsymbol{\zeta}_k^{(j)} = \varphi(\mathbf{x}_k^{(j)}, \tau_k^{(j)}; \tau_{k+1}^{(j)}) - \mathbf{x}_{k+1}^{(j)} = \mathbf{0} \qquad \text{with} \quad \begin{array}{l} k = 1, ..., m-1 \\ j = 1, ..., n \end{array} \tag{5.9}$$

The same constraint can be defined for the internal nodes of the parking orbit:

$$\boldsymbol{\zeta}_{park}^{(l)} = \varphi(\mathbf{x}_{park}^{(l)}, \tau_{park}^{(l)}; \tau_{park}^{(l+1)}) - \mathbf{x}_{park}^{(l+1)} = \mathbf{0} \qquad \text{with} \quad l = 1, ..., m_{park} - 1 \tag{5.10}$$

Position continuity between arcs:

$$\boldsymbol{\psi}_j = \boldsymbol{\rho}_m^{(j)} - \boldsymbol{\rho}_1^{(j+1)} = \mathbf{0} \qquad \text{with} \qquad j = 1, ..., n-1 \tag{5.11}$$

Time continuity between arcs:

$$\sigma_j = \tau_m^{(j)} - \tau_1^{(j+1)} = 0 \qquad j = 1, ..., n-1 \tag{5.12}$$

The time continuity between the parking orbit and the first arc of the transfer trajectory is enforced by definition. In fact the final time used to define the grid of equally spaced nodes in the parking orbit is exactly $\tau_1^{(1)}$, as reported in Eq. (5.4).

Initial boundary constraint:
The initial boundary constraint is shifted at the beginning of the parking orbit. To express this continuity condition, it is necessary to introduce a transformation to map the coordinates expressed in the MCME2000 to the RnBP–RPF.

Initially, the keplerian parameters are used to retrieve the initial position in the MCME2000 reference frame, as reported in Eq. (4.3) and (4.4). An additional rotation is required to transform the coordinates in the J2000 reference frame centered in the Moon [20]:

$$\mathbf{r}_{J2000} = T_2\,\mathbf{r}_{MCME} \qquad \text{and} \qquad \mathbf{v}_{J2000} = T_2\,\mathbf{v}_{MCME} \tag{5.13}$$

where

$$\mathbf{T}_2 = \begin{bmatrix} 1 & 0 & 0 \\ 0 & \cos(i_M) & -\sin(i_M) \\ 0 & \sin(i_M) & \cos(i_M) \end{bmatrix} \tag{5.14}$$

where i_M= 24 deg is inclination of the lunar axis with respect to Earth's equator [27].

Then, the initial condition can be expressed in the solar barycentric J2000 by translating the center of the frame from the Moon to the SSB. This coordinates are then mapped into the synodic frame inverting Eq. (3.51) and (3.52):

$$\boldsymbol{\rho}_{syn,0} = \frac{\mathbf{R}(t) - \mathbf{b}(t)}{k(t)}\,C(t)^T \tag{5.15}$$

$$\boldsymbol{\eta}_{syn,0} = \frac{\mathbf{V}(t) - \dot{\mathbf{b}}(t) - [k(t)\dot{C}(t) + \dot{k}(t)C(t)]\boldsymbol{\rho}_{syn,0}}{\omega k(t)} C(t)^T \tag{5.16}$$

where $\mathbf{R}$ and $\mathbf{V}$ represent the position and velocity at the initial condition expressed in the inertial frame centered at the SSB; and $\mathbf{x}_{syn,0} = [\boldsymbol{\rho}_{syn,0}, \boldsymbol{\eta}_{syn,0}]$ is the initial condition mapped into synodic coordinates. It is worth noting that the transformation process is time dependent.

The initial boundary condition is used to enforce a direct correspondence between the keplerian parameters and the first node of the parking orbit already expressed in the synodic frame:

$$\boldsymbol{\psi}_{park,0} = \mathbf{x}_{park}^{(1)} - \mathbf{x}_{syn,0}(r_p,\, r_a,\, i_0,\, \Omega_0,\, \omega_0,\, \theta_0, \tau_{park,0}) = \mathbf{0} \tag{5.17}$$

where $\tau_{park,0}$ is the nondimensional time related to the first node of the parking orbit, introduced in the time dependent coordinate transformation.

Continuity between Parking Orbit and Transfer Trajectory:
A position continuity must be enforced to link the parking orbit with the rest of the arcs:

$$\boldsymbol{\psi}_0 = \boldsymbol{\rho}_{park}^{m_{park}} - \boldsymbol{\rho}_1^{(1)} = \mathbf{0} \tag{5.18}$$

This constraint does not involve the velocities since an impulsive maneuver is admitted to depart from the parking orbit.

Final boundary constraint
The final boundary condition is modified to account for the lack of a manifold structure in the RnBP–RPF. The last node on the last arc is set to be coincident with a point belonging to the halo expressed in the CRTPB. The latter is function of one nondimensional time coordinate t_{po}, since the initial seed of the halo is fixed $\mathbf{x}_{po,0}$. The constraint is defined as position continuity:

$$\boldsymbol{\psi}_f = \boldsymbol{\rho}_m^{(n)} - \varphi_r(\mathbf{x}_{po,0},\, 0;\, t_{po}) = 0 \qquad \text{where} \quad t_{po} \geq 0 \tag{5.19}$$

where $\mathbf{x}_{po,0}$ is the initial position along the halo, determined in Section 4.1. It is worth noting that the halo is still computed with the right hand side of the CRTBP in this intermediate step of the optimization process. This constraint is going to be updated in the next step of the refinement.

Mapping of the regularized variables
The final set of constraints are used to map the components of the impulsive maneuvers into the regularized variables $\mathbf{U}_j = [u_j,\, w_j,\, s_j]^T$. This conversion has already been introduced in Eq. (4.23) and (4.24). Hereafter, the updated version is reported:

$$\boldsymbol{\Gamma}_0 = \boldsymbol{\eta}_1^{(j)} - \boldsymbol{\eta}_{park}^{(m_{park})} - \begin{bmatrix} u_0^2 - w_0^2 - s_0^2 \\ 2u_0 w_0 \\ 2u_0 s_0 \end{bmatrix} = \mathbf{0} \tag{5.20}$$

$$\boldsymbol{\Gamma}_j = \boldsymbol{\eta}_1^{(j+1)} - \boldsymbol{\eta}_m^{(j)} - \begin{bmatrix} u_j^2 - w_j^2 - s_j^2 \\ 2u_j w_j \\ 2u_j s_j \end{bmatrix} = \mathbf{0} \tag{5.21}$$

$$\boldsymbol{\Gamma}_n = \varphi_v(\mathbf{x}_{po,0},\, 0;\, t_{po}) - \boldsymbol{\eta}_m^{(n)} - \begin{bmatrix} u_n^2 - w_n^2 - s_n^2 \\ 2u_n w_n \\ 2u_n s_n \end{bmatrix} = \mathbf{0} \tag{5.22}$$

where $\varphi_v(\mathbf{x}_{po,0},\, 0;\, t_{po})$ corresponds to the velocity vector along the halo orbit at time t_{po}. It is worth reminding that in this step the halo is computed exploiting the dynamics of CRTBP. Accordingly, its velocity is normalized with a slightly different factor, thus introducing a small error. This approximation is acceptable because it provides initial estimates for the insertion coordinates and time on the halo orbit. This guess is then utilized to retrieve the corresponding quasi–halo as reported in Section 3.2.3.

These equations can be used except when $\Delta\eta_x^{(j)} < 0 \;\;\&\;\; \Delta\eta_y^{(j)} = \Delta\eta_z^{(j)} = 0$. By switching the first and second row in the column vector, a second formulations is developed, as explained in more detail in Eq. (4.20).

Complete set of equality constraint

The complete vector modeling the equality constraint is reported hereafter:

$$\mathbf{g}(\mathbf{y}) = (\boldsymbol{\zeta}_k^{(j)},\, \boldsymbol{\zeta}_{park}^{(l)},\, \boldsymbol{\psi}_j,\, \sigma_j,\, \boldsymbol{\psi}_{park,0},\, \boldsymbol{\psi}_0,\, \boldsymbol{\psi}_f,\, \boldsymbol{\Gamma}_0, \boldsymbol{\Gamma}_j) = \mathbf{0} \tag{5.23}$$

$$\text{with} \quad \begin{aligned} k &= 1, ..., m-1 \\ j &= 1, ..., n \\ l &= 1, ..., m_{park} - 1 \end{aligned}$$

In particular, the derivatives of the equality constraints differing from those reported in the previous formulation are presented in Appendix B.

5.3. Refinement process

In the refinement process each solution of a previous optimization is utilized as an initial guess for the successive NLP problem, as reported schematically below:

$$\begin{matrix} \text{Opt. with the} \\ \text{CRTBP halo} \end{matrix} \Rightarrow \begin{matrix} \text{Quasi–Halo} \\ \text{evaluation} \end{matrix} \Rightarrow \begin{matrix} \text{Opt. with the} \\ \text{quasi–halo} \end{matrix} \Rightarrow \begin{matrix} \text{Final refinement with} \\ \text{the planetocentric–RnBP} \end{matrix}$$

Quasi–Halo

A quasi–halo is determined based on the solution of the previous step. This periodic orbit is constructed to deviate the least from the target halo, according to the methodology introduced in Section 3.2.3. To set up this additional multiple shooting problem, the point along the periodic orbit where the optimized HIM takes place is considered as the the central node:

$$\tilde{\mathbf{x}}_{po}(\tilde{t}_{po}) = \varphi(\mathbf{x}_{po,0},\, 0;\, \tilde{t}_{po}) \tag{5.24}$$

where the notation $(\tilde{\cdot})$ is used to denote the quantities extracted from the previous optimization vector. Moreover, the final boundary constraint $\boldsymbol{\psi}_f$ depends on the nondimensional time $\tilde{\tau}_m^{(n)}$, used as reference to map the time coordinates of the nodes sampled along the periodic solution into the higher fidelity model.

To populate the initial guess vector, it is sufficient to propagate the central node $\tilde{\mathbf{x}}_{po}(\tilde{t}_{po})$ forward and backward in time by an arbitrary number of periods. In this thesis, the nodes are determined over a time window that spans 2 full periods ahead and 2 full periods backwards with respect to the initial guess. Within each period 5 nodes are sampled on equally spaced time grids. The time of each node in then shifted with respect to $\tilde{\tau}_m^{(n)}$. Then, the multiple shooting is carried out as described in Section 3.2.3. It is sufficient to store the coordinates of the optimized central node $\mathbf{x}_{QH,0}$ as the seed of the quasi periodic orbit. This, in turn, can be propagated forward or backward in time to find each point belonging to the quasi–halo, within the time window set at the beginning.

Optimization with the quasi–halo

In the successive step, this newly computed quasi–halo is adopted to rewrite the final boundary constraint:

$$\boldsymbol{\psi}_f = \boldsymbol{\rho}_m^{(n)} - \varphi_r(\mathbf{x}_{QH,0},\, \tau_{QH,0};\, \tau_m^{(n)}) = 0 \tag{5.25}$$

where $\mathbf{x}_{QH,0}$ represent the new seed of the quasi–halo computed in the previous step at a time $\tau_{QH,0} = \tilde{\tau}_m^{(n)}$. Then, it is simply possible to propagate this initial value to a desired time $\tau_m^{(n)}$ to retrieve an arbitrary point on the quasi–halo. In addition, the constraint used to map the regularized variable associated to the HIM can be rewritten as:

$$\boldsymbol{\Gamma}_n = \varphi_v(\mathbf{x}_{QH,0},\, \tau_{QH,0};\, \tau_m^{(n)}) - \boldsymbol{\eta}_m^{(n)} - \begin{bmatrix} u_n^2 - w_n^2 - s_n^2 \\ 2u_n w_n \\ 2u_n s_n \end{bmatrix} = \mathbf{0} \tag{5.26}$$

Therefore, the time coordinate t_{po} used to model the 1D periodic solution in the CRTPB is neglected in the updated formulation of the NLP problem. Considering this changes in the notation and constraints, a further optimization is carried out, the second exploiting the RnBP–RPF.

Final refinement

Lastly, a final optimization is performed by propagating the parking orbit in a planetocentic –RnBP, centered at the Moon. Therefore, all the nodes of this arc are transformed in the J2000 reference frame with Eq. (3.51) and (3.52). Then, a shift in the center of the reference frame is applied to express the coordinate in the J2000 centered at the Moon. The coordinates are then transformed in nondimensional units exploiting the scale length and velocity of the CRTPB (DU, VU). However, the scale used in the equation of motion is different, as reported in Section 3.3.1. As a result, the nodes of the parking orbit have to be dimensionalized again to be correctly normalized within the functions determining the objective and the constraints:

$$\mathbf{r}^* = \mathbf{r}_k^{(j)} \frac{DU}{R_{B,m}} \quad \text{and} \quad \mathbf{v}^* = \mathbf{v}_k^{(j)} \frac{VU}{\sqrt{\mu_m / R_{B,m}}} \tag{5.27}$$

The main reason behind this seemingly unnecessary transformation it to achieve a similar scale in the optimization variables to aid the convergence of the solver. In fact, if some quantities are orders of magnitude greater than others, the algorithm is not able to apply significant corrections to the larger ones.

This final refinement is carried out to impose strict integration tolerances, since the planetocentric–RnBP is computationally more efficient. This, in turn, is required to lower the constraint tolerances, thus achieving a better conditioned solution.

Initially, this method was considered even for earlier steps in the refinement process, however the precision of the STM after the renormalization of the units degrades. In fact, the nondimensional step taken by the solver between iterations corresponds to a much larger variation in the units of the planetocentric equations.

$$k(t) \approx DU \approx 222 R_{B,m} \tag{5.28}$$

where $k(t)$ is the scale length of the RnBP–RPF; DU is the scale length of the CRTBP; and $R_{B,m}$ is the equatorial radius of the Moon which is the scale length of the planetocentric –RnBP. Thus, this technique struggles to achieve continuity given ill–conditioned initial guesses. Therefore, it is adopted only as a final refinement step.

5.3.1. Validation with GMAT

To validate the planetocetric–RnBP formulation a comparative analysis is conducted exploiting the NASA GMAT software. During this test the same initial condition is propagated for 10 days using two methods:

- MATLAB implementation: the planetocentric equations from Section 3.3 are integrated using the `ode113` solver.
- GMAT implementation: a Moon–centered Perturbed Two Body Problem is solved including the gravitational perturbations from the Sun, planets and Pluto. Additionally, the SRP is considered along with the J_2 term of the lunar gravitational field to recreate a similar force model to the one implemented in MATLAB.

GMAT allows to specify the characteristics of an artificial object to retrieve a more accurate representation of the acceleration introduced by the solar radiation pressure. The physical properties, introduced in Section 3.2, are reported in Table 5.1 for reference.

m [kg]	A_{SRP} [m^2]	c_r [-]
28.7	0.23	0.3

Table 5.1: Assumed physical properties of the LUMIO CubeSat

A solution obtained after the third step of the refinement process (Section 5.3) is utilized in this analysis. In particular, the initial condition along the parking orbit is employed as the starting point of both simulations. The keplerian parameters are reported in Table 5.2 for completeness. This intermediate solution was later refined to determine Solution 1, presented in Section 6.2.

r_p [km]	r_a [km]	i_0 [deg]	Ω_0 [deg]	ω_0 [deg]	θ_0 [deg]	Initial Epoch [UTC]
1788.26	49742.62	94.99	186.28	321.13	351.16	2029 JAN 31 23:20:45

Table 5.2: Initial condition propagated in the validation process

This Keplerian set of parameters expressed in the MCME2000 frame is transformed in cartesian coordinates according to Eq. (4.32) and Eq. (4.37). Then, a simple rotation is adopted to retrieve the initial condition in the J2000 reference frame (Eq. 5.13), utilized in both implementations. A further non–dimensionalization is applied to determine the correct form of the initial condition expressed in the planetocentric–RnBP.

Then, the initial condition is propagated both in GMAT and MATLAB with a time step of 60 seconds and with an integration tolerance of $2.5 \cdot 10^{-14}$, to keep track of the differences. However, GMAT does not provide an equivalent solver to the one utilized in MATLAB, thus a Runge–Kutta 78 method is employed.

The resulting ballistic trajectories are represented in Figure 5.2.

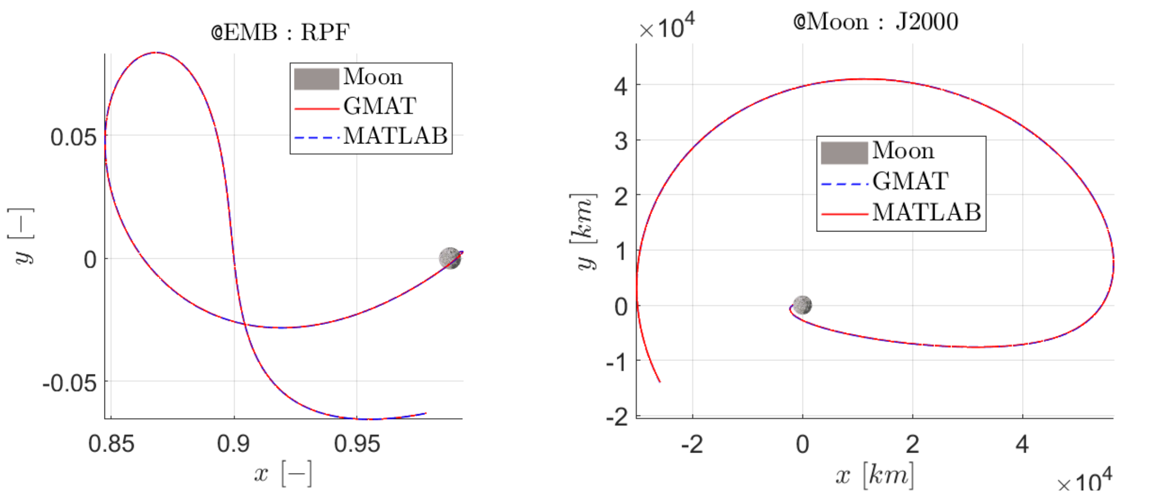

(a) View in the RPF.

(b) View in the J2000 reference frame centered at the Moon.

Figure 5.2: Comparison between GMAT and MATLAB propagation

At this scale the two trajectories seem to be coincident. To appreciate the differences, the discrepancy between the GMAT propagation and the solution evaluated with MATLAB is reported in logarithmic scale in Figure 5.3.

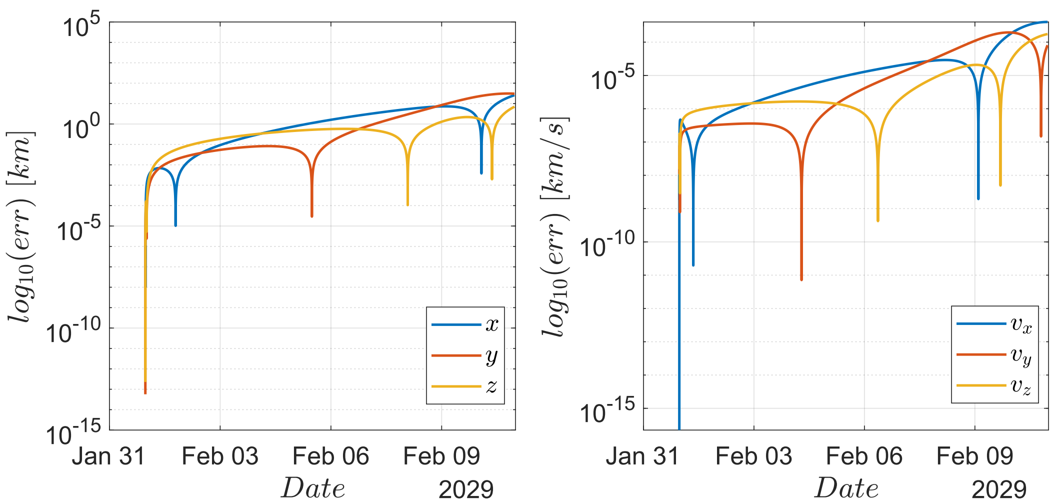

Figure 5.3: Error committed with respect to the simulation in GMAT

The error increases rapidly at the beginning due to possible differences in the first integration steps. As the simulation starts close to the pericenter of an highly elliptical orbit, the dynamics in proximity of the main attractor is extremely non–linear. This influences the first steps of the propagation that are handled differently by the two models which employ adaptive integration steps to compute the solution. The results are then interpolated on a common time grid to allow for a direct comparison.

The error grows steadily with time, due to the nonlinearities present in the equation of motion, reaching final values in the order of km and m/s. This discrepancy is expected in a comparison between different implementation methods, especially in chaotic environments such as the cislunar region.

6 | Results

In this chapter the results of the optimization process are introduced. Initially, ten initial guesses are determined by sampling the inner stable manifold and the possible parking orbits, as stated in Chapter 4. In particular, each candidate is utilized to solve four different NLP formulations defined by considering every permutation of the upper and lower bounds on (Ω_0, ω_0), as reported in Table 6.1.

	Ω_0 [deg]	ω_0 [deg]
Set # 1	[80, 100]	[140,150]
Set # 2	[170,190]	[320,330]
Set # 3	[80, 100]	[320,330]
Set # 4	[170,190]	[140,150]

Table 6.1: Different sets of solutions classified based on keplerian parameters

A first trajectory optimization is carried out in the CRTBP exploiting the free transport mechanism offered by the stable inner manifold emerging from the target halo orbit. The solutions obtained in this simplified dynamical model become a set of good initial candidates for the successive refinement process, according to the extensive formulation introduced in Chapter 5. This process exploits a series of intermediate steps to compute the final transfer trajectory in the RnBP–RPF.

The most promising results are presented in the following sections. To validate these solutions, the trajectories are propagated as a continuous arc. The integration is interrupted only in correspondence of a feasible impulsive maneuver. This process is adopted to verify that the multiple shooting solution is physically consistent when propagated independently of the solver. In addition, an eclipse analysis combined with a conjunction and opposition detection is conducted to rule out unfeasible solutions.

6.1. Transfer trajectory in the CRTBP

Considering all permutations of the initial conditions and bounds on (Ω_0, ω_0), a set of 40 solutions are computed in the CRTPB. The number of arcs and segments is selected as a tradeoff between convergence performance and computation time of each single iteration.

A formulation with a large number of nodes allows the solver more freedom to test the solution space, however it requires propagating more segments and computing larger Jacobian matrices, slowing down the algorithm. Instead, a multiple shooting problem with less optimization variables has generally a faster convergence rate due to a lower number of constraints being enforced. However, by increasing the duration of each arc and segment, the STM loses precision in determining a displaced trajectory.

After a few test runs to verify the convergence performance, the multiple shooting problem is solved for $n = 6$ and $m = 2$. The former represents the number of arcs and the latter the number of nodes for each single arc. Similar values are adopted in literature [13].

The NLP problem in the CRTPB is then solved exploiting the analytical derivatives of the objective function and of the constraints. In more detail, the equations of motion and variational equations are solved with MATLAB solver `ode113`, with an absolute and relative tolerances set to 10^{-12}.

To simplify the convergence in the successive refinement steps, it is necessary to determine a good initial guess. This is achieved by selecting constraint tolerance of 10^{-10} in the first optimization problem. However, the vast majority of solutions do not reach convergence before the maximum allowed number of iterations is met $(3 \cdot 10^3)$. This behavior is consistent with the results mentioned in [28]. This could be partially attributed to the selection of the objective function (Eq. 4.21), that requires strict constraint tolerances to be satisfied to correctly impose the map between the regularized variables and the components of each impulsive maneuver (Eqs. 4.23, 4.24).

This is not a concern, as the solutions still achieve an acceptable level of feasibility ($O(10^{-6})$ or lower), defined as the sum of all discrepancies in the enforced equality and inequality constraints. A more demanding tolerance is imposed in the following steps of the refinement process.

The best solution for each set of (Ω_0, ω_0) bounds is reported in Figure 6.1.

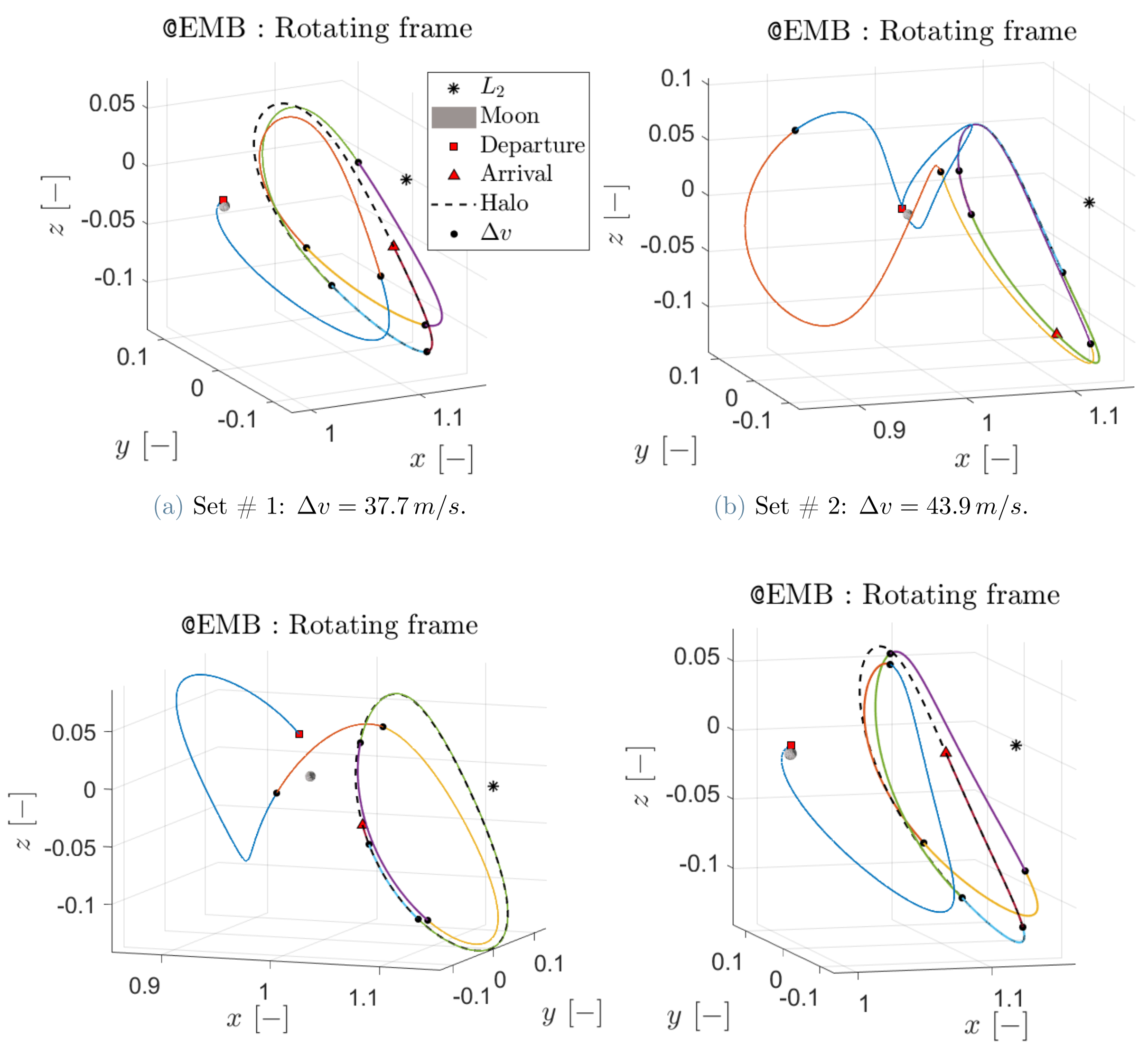

(a) Set # 1: $\Delta v = 37.7\,m/s$.

(b) Set # 2: $\Delta v = 43.9\,m/s$.

(c) Set # 3: $\Delta v = 72.7\,m/s$.

(d) Set # 4: $\Delta v = 38.1\,m/s$.

Figure 6.1: Best result for each set of solutions

This formulation reduces the unnecessary impulses to negligible values, as the regularized variables remove the singularities associated with null maneuvers in the derivatives of the objective function. This is shown in Figure 6.2, where the costs of each impulse is reported to stress the difference between null maneuvers and larger impulses.

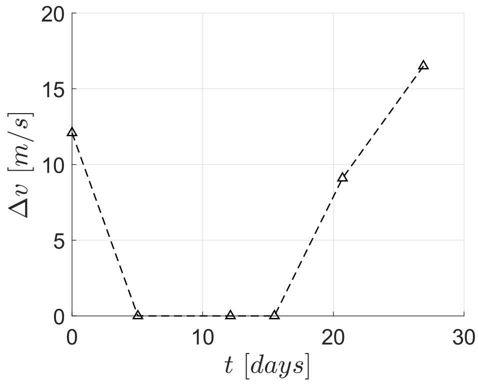

(a) Set # 1: $\Delta v = 37.7\,m/s$.

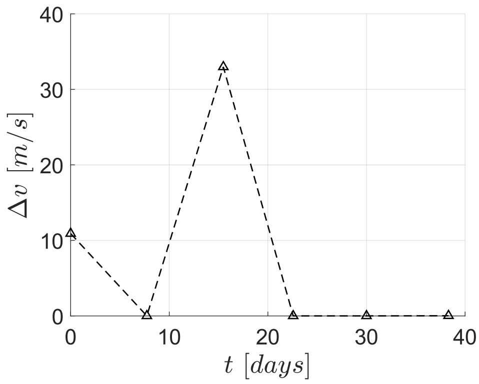

(b) Set # 2: $\Delta v = 43.9\,m/s$.

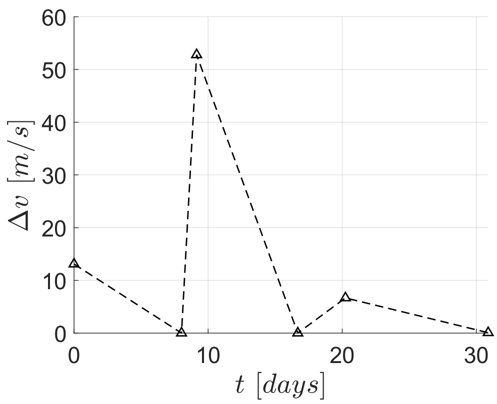

(c) Set # 3: $\Delta v = 72.7\,m/s$.

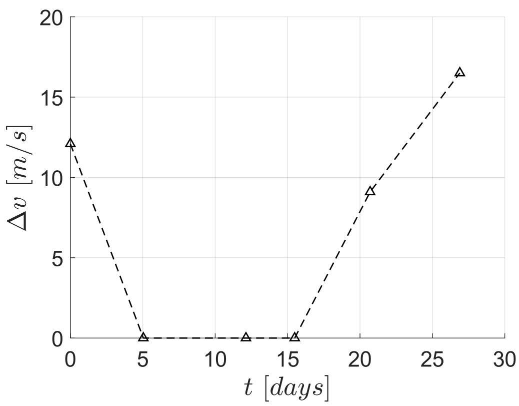

(d) Set # 4: $\Delta v = 38.1\,m/s$.

Figure 6.2: Time history of the magnitude of impulsive thrusts

In these solutions, the parking orbit is considered as a conic orbit, modeled with a set of keplerian parameters. However, this is not an accurate assumption, as the trajectory is disturbed by the Earth's gravitational attraction in a short period of time. As a result, it is considered as an additional arc of the multiple shooting problem in the successive refinement steps in the RnBP–RPF. This variation allows the solver to exploit the non–linear dynamics of the parking orbit, leading to transfer trajectories which deviate from the initial guesses determined in this section.

6.2. Refined solutions

The solutions retrieved in the CRTPB are then used as initial guesses for the trajectory optimization step in the RnBP–RPF. This refinement process introduces a more complex dynamical model that impacts the convergence performance of the solver. As expected, the number of steps required to achieve a feasible solution grows and the computation time for each iteration is increased. In particular, previous solutions exploiting multiple close encounters with the Moon often fail to converge. Still, the majority of initial guesses are able to converge to feasible solutions, with only a small fraction being actually compliant with the requirements listed in Table 2.2.

	Initial guesses	Compliant solutions
Set # 1	10	0
Set # 2	10	2
Set # 3	10	1
Set # 4	10	0

Table 6.2: Solutions compliant with the problem requirements

It is worth noting that n is increased in this problem by considering the trajectories described by the stable manifold and the parking orbit as additional arcs. Since the parking orbit is treated separately, the NLP problem is solved for $n = 7$. This allows to increase the number of segments composing the parking orbit to $m_{park} = 7$, without varying the number of nodes in the rest of the trajectory. This finer discretization improves the precision of the STM in the first part of the trajectory, leading to a better convergence performance. In addition, a larger number of segments is utilized to exploit parallel computing capabilities to lower the computation time of the parking orbit, that is the most demanding arc due to the proximity to the Moon.

As in the previous optimization, the NLP problem is solved exploiting MATLAB `fmincon` using the interior point algorithm, still providing the analytical derivatives. In addition, the hessians are approximated internally by the solver with the `bfgs` method. The relative and absolute integration tolerance are reduced only at the final step of the refinement to $2.5 \cdot 10^{-13}$, to avoid slowing down the previous optimizations mentioned in Section 5.3. An higher precision in the integration leads to more accurate STMs, which determine a lower discrepancy in the imposed equality and inequality constraints. This allows to lower the maximum constraint tolerance to $1 \cdot 10^{-12}$.

Hereafter, the three compliant solutions are reported along with a complete breakdown of the cost of each maneuver. Additionally, the validation process is applied to each of the following solutions to assess their feasibility along with an eclipse analysis. Lastly, a brief conjunction and opposition analysis is conducted to determine if the nominal maneuvers are planned in correspondence of these challenging communication conditions.

Solution 1:

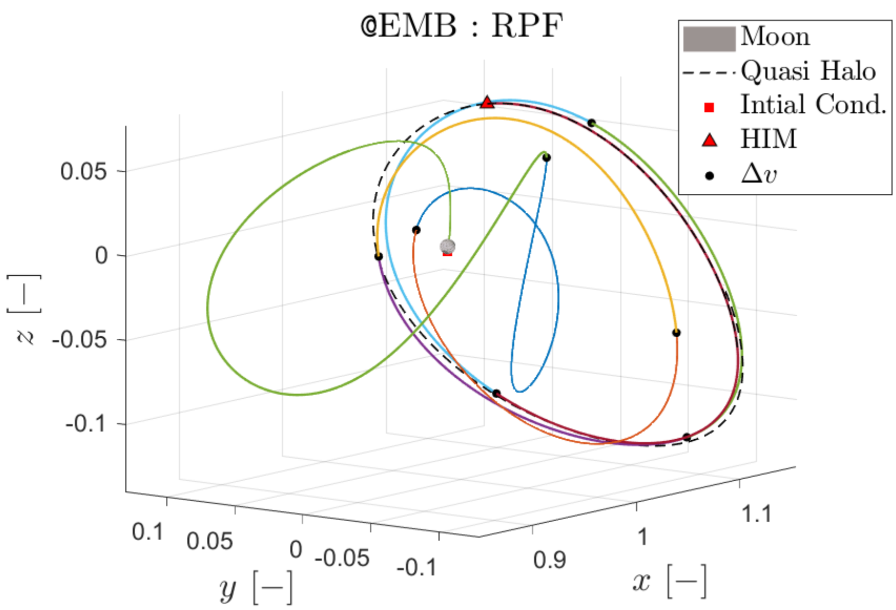

Figure 6.3: Graphical representation of the first transfer

r_p [km]	r_a [km]	i_0 [deg]	Ω_0 [deg]	ω_0 [deg]	θ_0 [deg]
1788.26	49642.97	94.99	186.28	321.13	351.16

Table 6.3: Optimized initial keplerian parameters (Solution 1)

	Epoch [UTC]	Time after t_0 [d]	Magnitude [m/s]
Initial cond.	2029 JAN 31 23:20:45	0	-
Δv_{park}	2029 FEB 11 12:02:48	10.52	7.20e-10
Δv_1	2029 FEB 21 05:24:13	20.25	2.05e+01
Δv_2	2029 FEB 25 19:03:38	24.82	7.90e-10
Δv_3	2029 MAR 02 11:34:52	29.50	3.10e-10
Δv_4	2029 MAR 07 11:08:26	34.49	6.09e-10
Δv_5	2029 MAR 12 20:58:37	39.90	1.18e-09
Δv_6	2029 MAR 19 06:12:43	46.28	2.03e-10
Δv_{HIM}	2029 MAR 28 06:34:23	55.30	4.76e-04
Total			**2.05e+01**

Table 6.4: Maneuvers of the first solution

As expected, the formulation is able to minimize the unnecessary thrust impulses thanks to the regularized variables. The maneuvers with a magnitude below 5 mm/s are considered unfeasible based on the specifics of the propulsion system, thus they are neglected in the following validation process. After a single impulse is applied (Δv_1), the transfer can be considered as a ballistic trajectory during the validation. Since Δv_{park} is negligible, the first arc acts as an extension to the parking orbit, thus exploiting the highly non–linear dynamics to find an optimal departure condition.

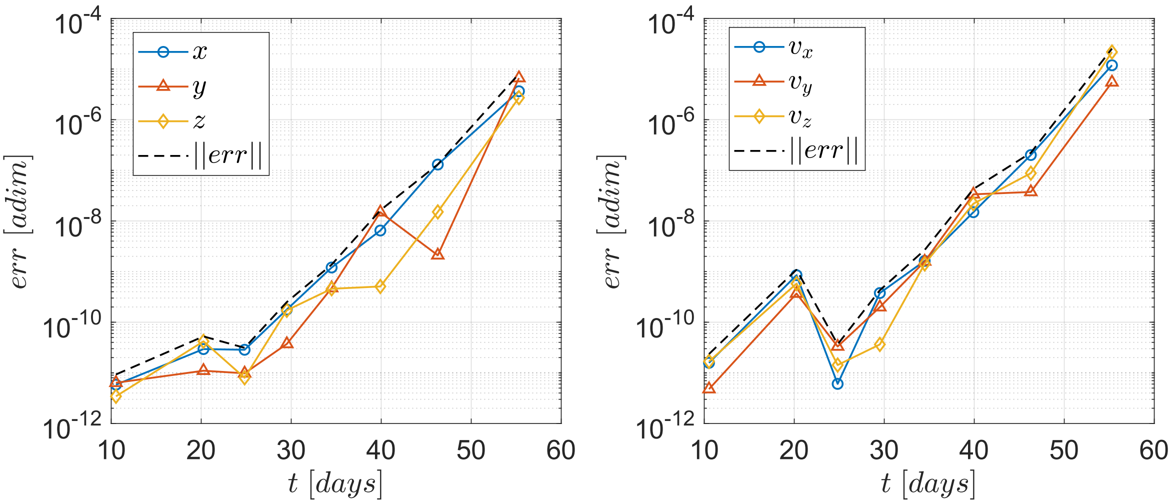

Figure 6.4: Error committed in the validation process of the first solution, evaluated at the maneuver points. The time in days past the initial condition reported in Table 6.4.

In this process, the error introduced by the numerical integration and by neglecting the unfeasible maneuvers grows with time. After the parking orbit, this discrepancy is considerably small, however it accumulates rapidly due to the high–nonlinearity of the equation of motion. This is partially expected, as the trajectory outside the solver cannot distribute errors among different arcs. This is not a concern, as the error can be limited with trajectory correction maneuvers in future analyses.

It is worth noting that the total cost of this transfer is a small fraction of the overall budget (25.62%), leaving large margins for the Station Keeping (SK) and Navigation maneuvers. In addition, the initial point in the simulation is located close to the lunar surface, possibly subject to perturbations due to higher order terms of the lunar gravitational model. Therefore, the trajectory should be tested in a higher fidelity model comprehensive of these additional terms to verify its feasibility.

In addition, the parking orbit deviates significantly from a conic, with large variations in the keplerian elements. Therefore, the same initial position in the inertial frame cannot be recovered after one complete orbit. This can be said also for the following solutions presented in the next sections. In case of a significant delay in the first feasible maneuver, the transfer would require a complete new analysis.

Solution 2:

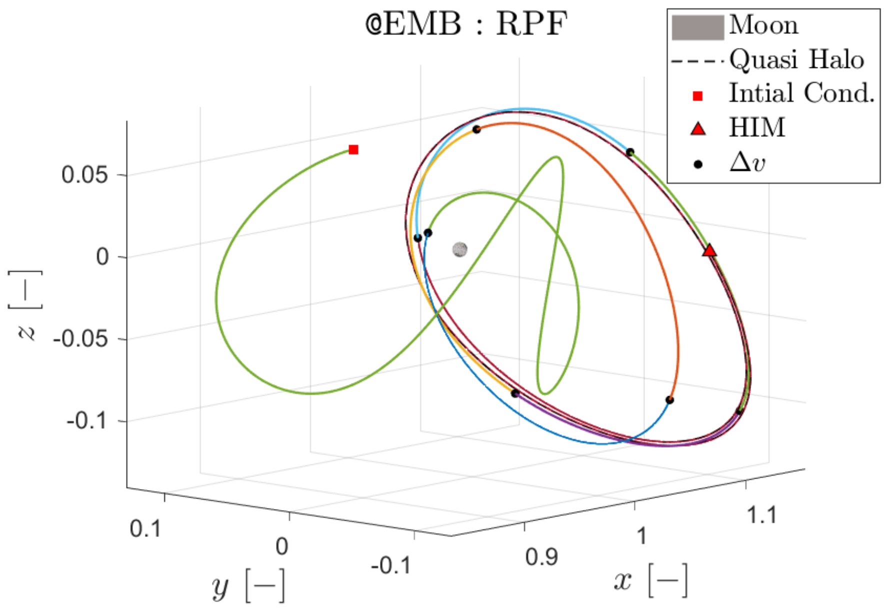

Figure 6.5: Graphical representation of the second transfer

r_p [km]	r_a [km]	i_0 [deg]	Ω_0 [deg]	ω_0 [deg]	θ_0 [deg]
1787.41	61737.40	93.60	170.00	325.47	179.48

Table 6.5: Optimized initial keplerian parameters (Solution 2)

The initial condition of the second solution is almost at the apocenter. The parking orbit is larger than in the previous solution allowing the solver to exploit a more disturbed region of space, influenced mostly by Earth's gravity and in a minor amount by the Sun. The first optimization in the CRTPB provided a good initial guess, resulting in a transfer that exploits the natural motion ruled by the dynamics of the RnBP–RPF.

The majority of the impulses are reduced approximately to zero, demonstrating the advantages of the formulation based on the regularized variables. A more detailed description of the maneuvers is reported in Table 6.6.

	Epoch [UTC]	Time after t_0 [d]	Magnitude $[m/s]$
Initial cond.	2029 JAN 04 19:27:10	0	-
Δv_{park}	2029 JAN 23 15:04:40	18.8177	2.10e+01
Δv_1	2029 JAN 27 08:02:36	22.5246	1.29e-12
Δv_2	2029 JAN 31 06:00:07	26.4396	8.54e-12
Δv_3	2029 FEB 04 03:19:23	30.3279	2.33e-12
Δv_4	2029 FEB 08 03:03:20	34.3168	3.15e-12
Δv_5	2029 FEB 12 00:57:22	38.2293	3.58e-12
Δv_6	2029 FEB 15 22:02:43	42.1080	4.51e-11
Δv_{HIM}	2029 MAR 10 17:09:41	64.9045	6.27e-06
Total			**2.09e+01**

Table 6.6: Maneuvers of the second solution

The second solution achieves a similar budget with respect to the first one. As in the previous case, a single maneuver is actually imposed in the validation test, since the rest of the impulses are below the minimum threshold (5 mm/s). However, in this case the largest neglected maneuver is two order of magnitude lower than in Solution 1.

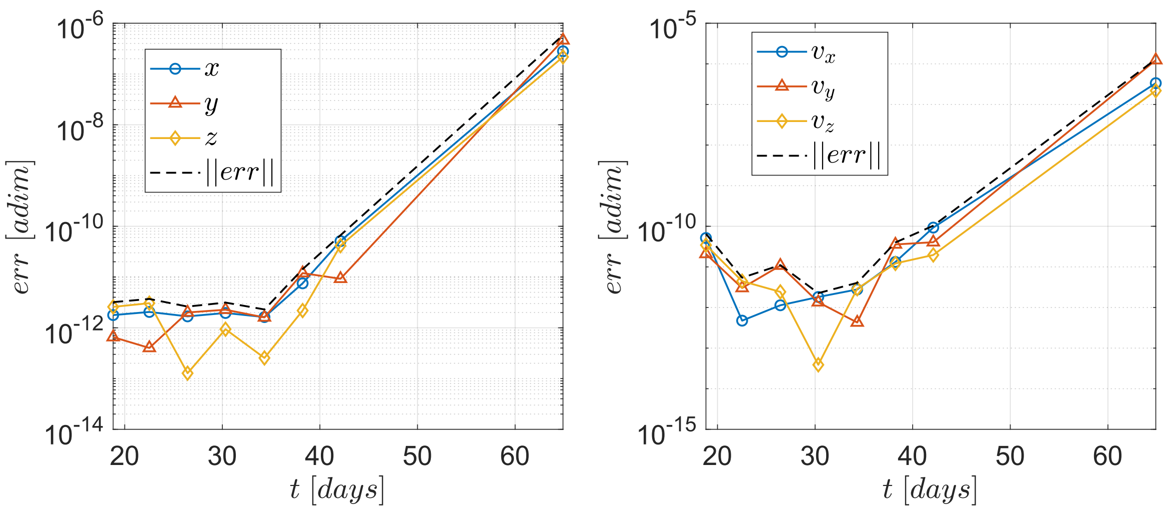

Figure 6.6: Error committed in the validation process of the first solution, evaluated at the maneuver points. The time in days past the initial condition reported in Table 6.6.

The estimated errors in the validation process are lower compared to the previous analysis. This can be attributed to the larger relative distance from the Moon during the initial arcs of the transfer. Therefore, this trajectory is a more numerically stable solution.

It is worth noting that no additional maneuver is applied after the departure from the parking orbit. As a result, this transfer can be considered as a ballistic trajectory. In addition, the last arcs are almost coincident with the quasi–halo orbit, which is naturally unstable. This explains the rapid amplification of the errors during the last portion of the transfer, following an exponential growth, as reported in Figure 6.6. This phenomenon can be reduced by performing Trajectory Correction Maneuvers (TCM), during the dedicated time slots between nominal impulses, and eventually Station Keeping Maneuvers once the target orbit is reached.

Solution 3:

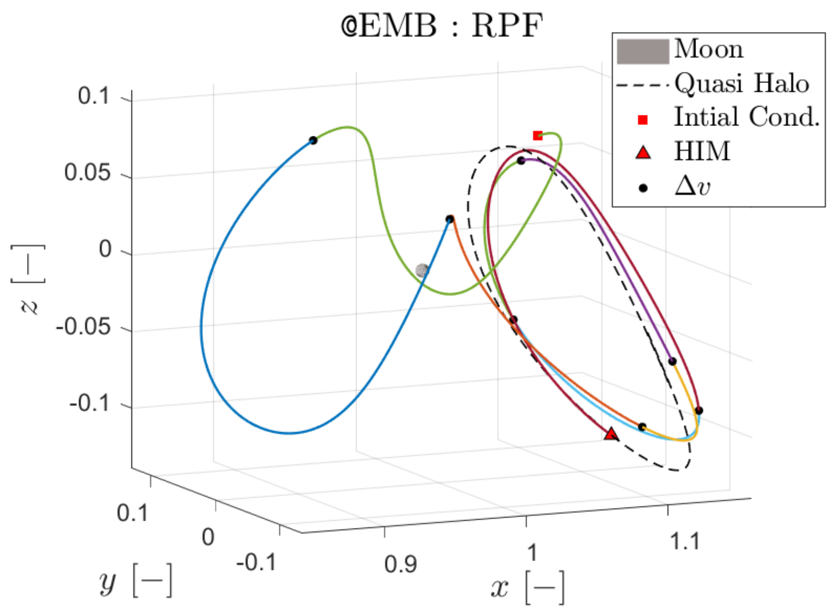

Figure 6.7: Graphical representation of the third transfer

r_p [km]	r_a [km]	i_0 [deg]	Ω_0 [deg]	ω_0 [deg]	θ_0 [deg]
1887.40	59293.31	91.35	94.97	320.00	170.58

Table 6.7: Optimized initial keplerian parameters (Solution 3)

The last solution presents a parking orbit with high eccentricity. As a result, a small departure maneuver is sufficient to initiate the transfer (Δv_1). However, this can be interpreted as a more unstable solution, that requires a precise targeting of the initial conditions. In Table 6.8, a detailed breakdown of the nominal maneuvers is presented.

	Epoch [UTC]	Time after t_0 [d]	Magnitude $[m/s]$
Initial cond.	2029 JAN 17 12:48:24	0	-
Δv_{park}	2029 JAN 23 15:04:40	7.00	9.2393e-07
Δv_1	2029 FEB 01 03:51:35	14.6272	8.20e+00
Δv_2	2029 FEB 05 08:59:17	18.8409	3.43e-06
Δv_3	2029 FEB 09 09:38:04	22.8678	1.81e-06
Δv_4	2029 FEB 13 12:04:05	26.9692	1.31e-05
Δv_5	2029 FEB 16 22:05:51	30.3871	8.40e-05
Δv_6	2029 FEB 23 00:51:39	36.5023	1.24e-06
Δv_{HIM}	2029 MAR 04 20:41:49	46.3288	2.46e+01
Total			**3.28e+01**

Table 6.8: Maneuvers of the third solution

In this case, the trajectory consists of two main maneuvers (Δv_1, Δv_{HIM}). However, it is unusual to have a HIM of this magnitude. As the region surrounding the quasi–halo is unstable, a costly final impulse could lead to a difficult mapping into a continuous maneuver in a future study.

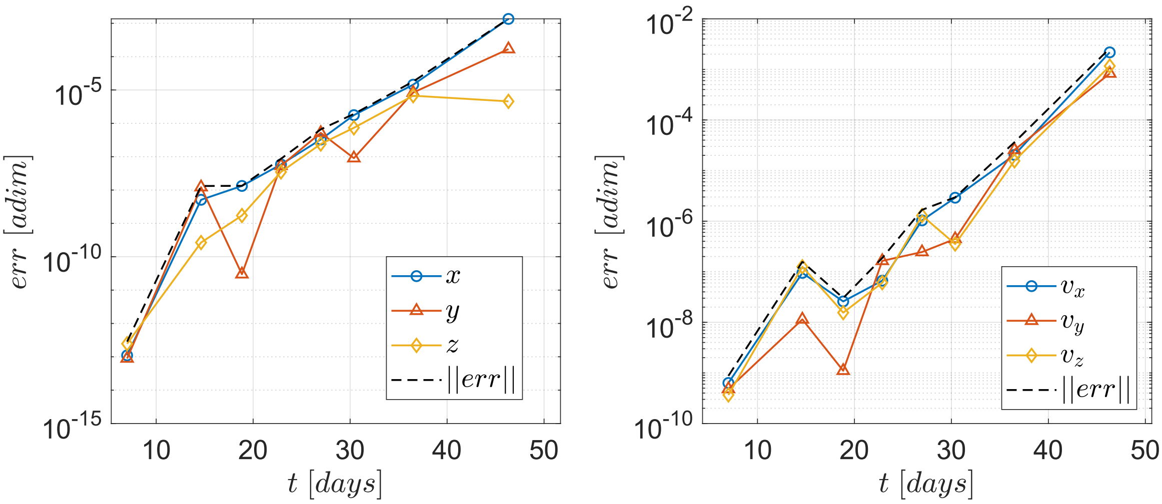

Figure 6.8: Error committed in the validation process of the third solution, evaluated at the maneuver points. The time in days past the initial condition reported in Table 6.4.

This is the most expensive solution presented so far and it is the least stable from the validation stand point, as reported in Figure 6.8. In fact, the error achieved in this process is the largest among the three transfers. A further refinement could reduce the unnecessary impulses, leading to a better conditioned solution.

6.2.1. Compliance to Geometrical Constraints

A preliminary analysis on the eclipse conditions is carried out in this section. The umbra and penumbra regions are computed geometrically, following the conical model introduced in [33]. This method confronts the distance of the spacecraft from the Sun–Moon and Sun–Earth lines with the umbra and penumbra distances. It is worth noting that the time reported on the x–axis in the following graphs is expressed as days past the initial condition.

The first solution is located in the umbra projected by the Moon at the initial condition, during the parking orbit. This can potentially influence the commissioning of the subsystems, requiring a further verification. This can be simply avoided by starting the operations after the eclipse, as the parking orbit is longer (10.52 d) than the maximum commissioning time (7 d). Moreover, the spacecraft rapidly leaves the umbra region, as reported in Table 6.9.

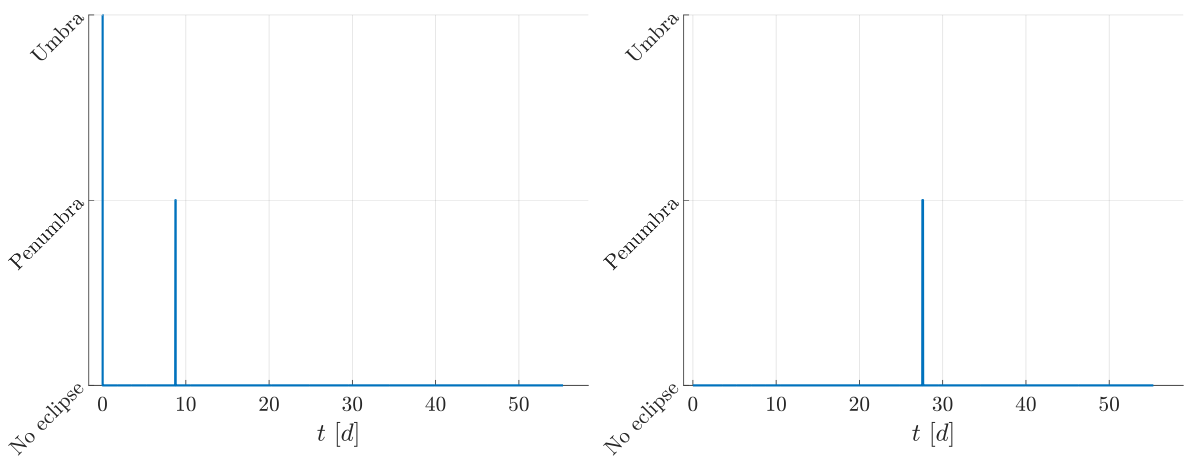

(a) Moon eclipse (M). (b) Earth eclipse (E).

Figure 6.9: Eclipse analysis for the first solution (UTC_0 = 2029 JAN 31 23:20:45)

Condition	Penumbra span [h]	Umbra span [h]	Event Start [UTC]	Event End [UTC]
Umb.(M)	-	0.24	2029 JAN 31 23:20	2029 JAN 31 23:35
Pen.(M)	0.66	-	2029 FEB 09 17:22	2029 FEB 09 18:02
Pen.(E)	1.74	-	2029 FEB 28 12:51	2029 FEB 28 14:36

Table 6.9: Eclipse analysis on the first solution, reported in Figure 6.3

This is a preliminary analysis based on the propagated solution with absolute and relative tolerance set to $2.5 \cdot 10^{-13}$. As a result, the exact transition between illuminated region, penumbra and umbra is not detected with an event function. This explains the missing transition from umbra to penumbra in Figure 6.9a. Therefore, the duration of this event could be slightly underestimated.

Instead, the second solution is the least influenced by the illumination conditions as it presents only a brief crossing of the Earth's penumbra region (Figure 6.10b). This analysis paired with the validation step presented earlier (Figure 6.6) determine the second transfer to be the better candidate.

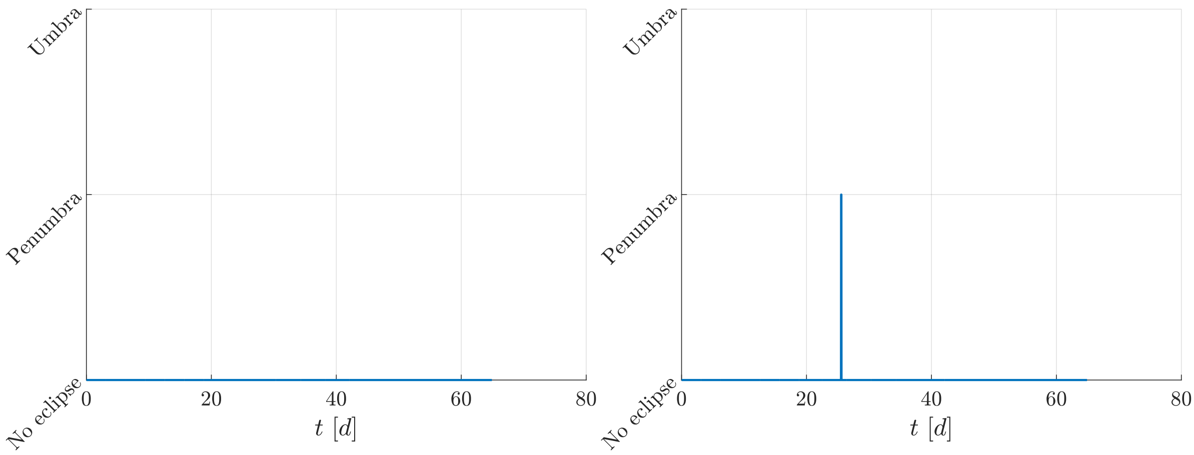

(a) Moon eclipse (M).

(b) Earth eclipse (E).

Figure 6.10: Eclipse analysis for the second solution (UTC_0 = 2029 JAN 04 19:27:10)

Eclipse	Penumbra span [h]	Umbra span [h]	Event Start [UTC]	Event End [UTC]
Pen.(E)	1.02	-	2029 JAN 30 08:26	2029 JAN 30 09:28

Table 6.10: Eclipse analysis on the second solution, reported in Figure 6.5

Lastly, the third solution crosses the umbra region of the Moon once during the parking orbit (Figure 6.11). However, in this case the scarce illumination condition is located approximately in the middle of the commissioning phase, assumed to be carried out during the coasting along the parking orbit. Moreover, this is the most expensive solution in terms or required deterministic Δv, therefore it can be considered as the least ideal transfer compliant with the mission requirements.

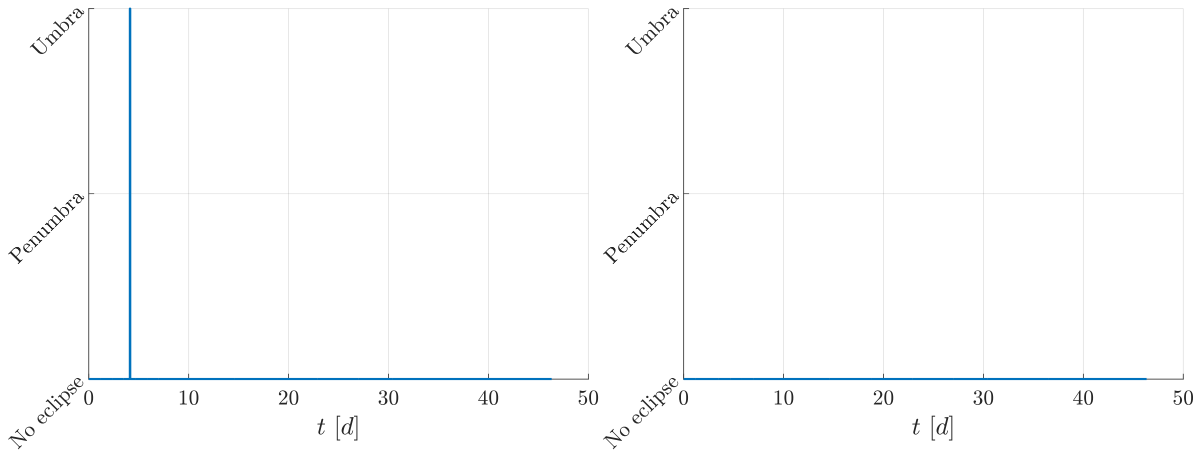

(a) Moon eclipse (M). (b) Earth eclipse (E).

Figure 6.11: Eclipse analysis for the third solution (UTC_0 = 2029 JAN 17 12:48:24)

Eclipse	Penumbra span [h]	Umbra span [h]	Event Start [UTC]	Event End [UTC]
Umb.(M)	-	0.83	2029 JAN 21 15:33	2029 JAN 21 16:23

Table 6.11: Eclipse analysis on the third solution, reported in Figure 6.7

It is important to state that each eclipse event satisfies a criteria on the energy consumed during eclipse. This is computed with the following formula:

$$A\,t_p + B\,t_e \leq 86.8 \text{ Wh} \tag{6.1}$$

where t_p and t_e are the times spent in umbra and penumbra expressed in hours, $A = 42\,W$ and $B = 71\,W$ are respectively the power demand in those conditions.

Lastly, a conjunction and opposition analysis is carried out by measuring the spacecraft–Earth–Sun angle denoted as η. These events take place when η is 0 and 180 degrees, respectively. In this conditions the communications between a spacecraft and Earth become difficult due to the radio emissions coming from the Sun, which affect either the down–link or the up–link segment. Therefore, high risk operations requiring constant communication with a ground station are usually avoided during these events. In the case of the transfer trajectory, the impulse maneuvers are considered as crucial phases of the mission and thus they shall not be performed during a conjunction or an opposition.

The evolution of the spacecraft–Earth–Sun angle for each of the three transfers is reported in Figure 6.12. The shaded areas represent conditions where the communications are degraded. This regions are extended to values of η above 175 deg and below 5 deg as a contingency margin. As in previous graphs, the time is expressed as days past the initial condition along the parking orbit.

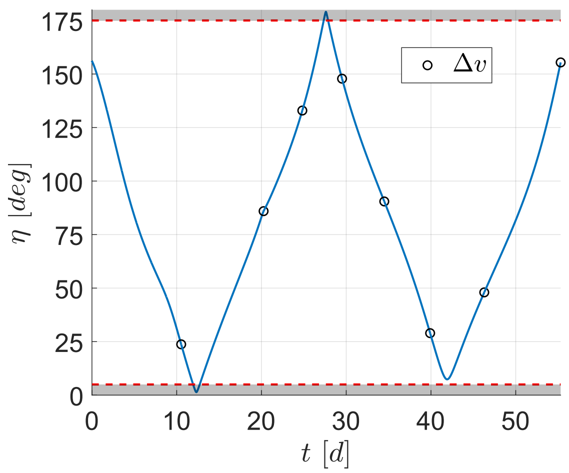

(a) Solution 1.

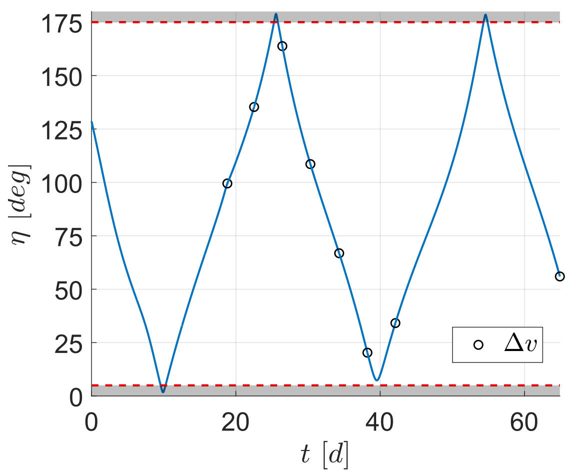

(b) Solution 2.

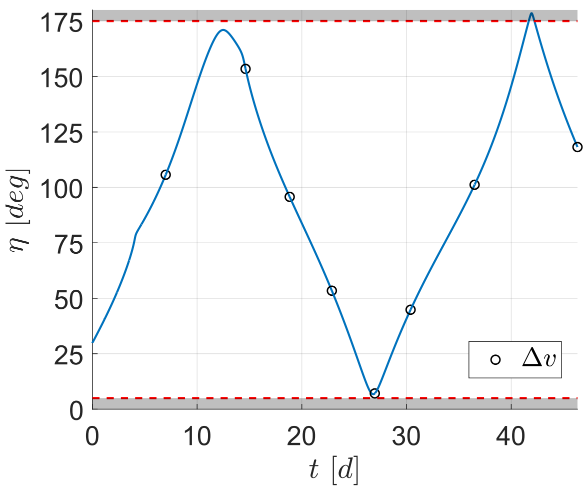

(c) Solution 3.

Figure 6.12: Conjunction and Opposition Analysis

In each solution the nominal impulses are planned outside the shaded region, thus avoiding difficulties in the communications that could complicate or even prevent the maneuver.

7 | Conclusions

In this thesis, an alternative transfer trajectory for the LUMIO mission is investigated and optimized through a series of refinement steps by gradually increasing the model complexity. LUMIO aims to detect meteoroid impacts on the lunar far side to gather valuable data improving the lunar situational awareness for manned and unmanned missions. The spacecraft is assumed to be injected by a carrier in a highly elliptical lunar parking orbit, where the commissioning operations are going to take place. The transfer is designed to reach the operational orbit, represented by a quasi–halo about the L_2 point of the Earth–Moon system. In this work a preliminary analysis is conducted to assess the feasibility of this alternative transfer strategy, given the limited Δv budget and thrust authority of the LUMIO CubeSat.

The trajectory optimization is transcribed into a NLP problem assuming impulsive maneuvers at the boundary of each arc in a multiple–burn multiple–shooting formulation. In particular, a set of regularized variables based on the Kustaanheimo–Stiefel transformation are introduced, allowing to remove the singularities in the derivatives of a fuel–optimal problem. As a result, the unnecessary impulses are reduced to negligible values. This methodology is applied to each step of the refinement process with variations in the definition of the objective function and constraints.

The transfer is initially sought in the Circular Restricted Three Body Problem to exploit the free transport mechanism offered by the stable branch of the manifold emerging from the target orbit. Moreover, the final boundary constraint is conveniently represented by a periodic halo orbit, thus simplifying the formulation. The initial guesses are retrieved performing a sampling of the feasible parking orbits and by retaining the closest approaches of the stable inner manifold to the Moon' surface. The pair of points belonging to the two datasets satisfying certain thresholds on relative position and velocity are then clustered with a k–medoids method to determine the set of the most representative initial conditions. A total of 40 optimized transfer trajectories are computed in the CRTPB and are utilized as the initial guesses for a successive refinement in higher–fidelity models.

Based on the geometry of the Earth–Moon system, the Restricted n–Body Problem in a Roto–Pulsating Frame is selected as a suitable dynamical model to capture and to exploit the complex dynamics of the cislunar environment. This formulation includes the gravitational accelerations introduced by the main bodies of the Solar system, whose position is retrieved from real ephemerides. The set of forces is completed considering the effect of the SRP along with the J_2 term of the lunar gravitational field.

A series of sequential optimizations are then carried out to determine the transfer trajectories in the RnBP–RPF. First, the NLP problem is solved considering the target halo, still computed according to the CRTBP, as final constraint. Then, the corresponding quasi–halo is determined with a separate multiple shooting problem aimed at minimizing the quadratic form of the continuity constraints. The quasi periodic orbit is sought on a time window centered at the halo injection conditions evaluated in the previous step of the optimization. Accordingly, the result of this additional problem consists in a trajectory deviating the least possible amount from the original halo. In this way phasing problems with the initial guess are mitigated in correspondence of the HIM point.

Subsequently, this quasi–halo is adopted as a final boundary condition in a successive optimization in which the trajectory is entirely computed in the RnBP–RPF. Lastly, the solution is evaluated in a modified formulation adopting the planetocentric–RnBP to propagate the parking orbit. In this way it is possible to lower the integration tolerances to the required precision level still maintaining an acceptable computation time.

In total, 40 transfer trajectories have been computed in the the high fidelity model. The multiple shooting implementation is capable of computing a wide variety of possible solutions both in term of Δv and parking orbit duration. In this way, it is possible to determine an optimal departure condition to exploit few maneuvers to reach the target quasi–halo orbit.

The majority of these transfers are not compliant with the fuel budget $\Delta v_{\mathrm{MAX}} = 80$ m/s, with only three satisfying all the mission constraints listed in Table 2.2. These solutions exploit one or two impulses to reach the intended target, whereas the rest of the maneuvers are reduced to negligible values. This highlights the ability of the formulation to nullify unnecessary impulses and to leverage the highly nonlinear dynamics in the RnBP–RPF.

The total cost of the compliant trajectories represents $25.62 - 41\%$ of the overall budget Δv, leaving large margins for the Station Keeping (SK) and Navigation Maneuvers. These three trajectories are then compared to determine the most suitable transfer based on a validation processes aimed to assess their feasibility. In particular, the solutions are propagated as a continuous arc interrupted only by feasible impulsive maneuvers, whose magnitude is grater or equal to 5 mm/s. The impulses that do not satisfy this minimum threshold are considered unfeasible and are not applied in this process. They error accumulated with respect to the nominal solution are measured at the maneuver points to determine the behavior of the trajectories outside the solver. Based on this metric and on the overall cost, the trajectory denoted as Solution 2 is considered the most promising result. In fact, its cost is the second lowest (20.9 m/s), nearly matching the cheaper alternative (20.5 m/s), while remaining the most robust in the validation.

Lastly, an eclipse analysis is conducted on the compliant transfers to verify that the energy consumed in scarcely illuminated conditions is below a maximum threshold. It is worth noting that all the detected events in the different solutions satisfy this requirement. Additionally, a conjunction and opposition analysis confirms that all nominal maneuvers are planned outside these events, where communications are degraded.

Overall, the results presented in this thesis demonstrate that transfers can be determined from a lunar parking orbit to LUMIO's target operational orbit respecting the limited Δv budget. This opens the possibility to consider an alternative transfer design, providing greater redundancy in case external factors compromise the nominal mission plan.

7.1. Future developments

In future works this methodology can be applied on a larger set of initial conditions to determine an increased number of compliant solution to the mission requirements. It is likely that there could be cheaper transfer trajectories represented by local minima spread in the highly irregular solution space, that are not reached by the solver starting from the limited set of initial conditions. It is worth noting that the process is computationally heavy, therefore a parallelization of the optimization process is suggested to manage the run time. In addition, it is possible to extend the solutions found is a specific month of the year to a date in which the relative geometry of the Earth–Moon system repeats itself, to assess variability during the launch window. Lastly, this work accounts only for deterministic impulses, therefore a further navigation problem must be developed to evaluate the non–deterministic costs paired with a station keeping analysis and a final mapping of the impulses to continuous maneuvers.

Bibliography

[1] C. Acton, N. Bachman, B. Semenov, and E. Wright. A look towards the future in the handling of space science mission geometry. *Planetary and Space Science*, 150: 9–12, 2018.

[2] C. H. Acton. Ancillary data services of nasa's navigation and ancillary information facility. *Planetary and Space Science*, 44(1):65–70, 1996.

[3] R. H. Battin. *An introduction to the mathematics and methods of astrodynamics*. Aiaa, 1999.

[4] J. T. Betts. Survey of numerical methods for trajectory optimization. *Journal of guidance, control, and dynamics*, 21(2):193–207, 1998.

[5] R. H. Byrd, M. E. Hribar, and J. Nocedal. An interior point algorithm for large-scale nonlinear programming. *SIAM Journal on Optimization*, 9(4):877–900, 1999.

[6] A. Celletti. Basics of regularization theory. In *Chaotic worlds: from order to disorder in gravitational N-body dynamical systems*, pages 203–230. Springer, 2003.

[7] A. Cervone, F. Topputo, S. Speretta, A. Menicucci, E. Turan, P. Di Lizia, M. Massari, V. Franzese, C. Giordano, G. Merisio, et al. Lumio: A cubesat for observing and characterizing micro-meteoroid impacts on the lunar far side. *Acta Astronautica*, 195: 309–317, 2022.

[8] A. M. Cipriano, D. A. Dei Tos, and F. Topputo. Orbit design for lumio: The lunar meteoroid impacts observer. *Frontiers in Astronomy and Space Sciences*, 5:29, 2018.

[9] S. Creech, J. Guidi, and D. Elburn. Artemis: An overview of nasa's activities to return humans to the moon. In *2022 IEEE Aerospace Conference (AERO)*, pages 1–7, 2022. doi: 10.1109/AERO53065.2022.9843277.

[10] D. A. Dei Tos. Automated trajectory refinement of three-body orbits in the real solar system model. Master's thesis, Politecnico di Milano, 2013.

[11] D. A. Dei Tos and F. Topputo. On the advantages of exploiting the hierarchical structure of astrodynamical models. *Acta Astronautica*, 136:236–247, 2017.

[12] D. A. Dei Tos and F. Topputo. Trajectory refinement of three-body orbits in the real solar system model. *Advances in Space Research*, 59(8):2117–2132, 2017.

[13] D. A. Dei Tos and F. Topputo. High-fidelity trajectory optimization with application to saddle-point transfers. *Journal of Guidance, Control, and Dynamics*, 42(6):1343–1352, 2019.

[14] T. A. Ely and E. Lieb. Constellations of elliptical inclined lunar orbits providing polar and global coverage. *the Journal of the Astronautical Sciences*, 54(1):53–67, 2006.

[15] R. W. Farquhar. The flight of isee-3/ice: origins, mission history, and a legacy. *The Journal of the astronautical sciences*, 49(1):23–73, 2001.

[16] D. Folta and D. Quinn. Lunar frozen orbits. In *AIAA/AAS Astrodynamics Specialist Conference and Exhibit*, 2006.

[17] S. Fuller, E. Lehnhardt, C. Zaid, and K. Halloran. Gateway program status and overview. *Journal of Space Safety Engineering*, 9(4):625–628, 2022.

[18] R. Funase, S. Nakajima, Y. Kawabata, R. Fuse, H. Sekine, and H. Koizumi. Equuleus: Initial operation results of an artemis-1 cubesat to the earth—moon lagrange point. *Small Satellite Conference*, 2023.

[19] T. Gardner, B. Cheetham, A. Forsman, C. Meek, E. Kayser, J. Parker, M. Thompson, T. Latchu, R. Rogers, B. Bryant, et al. Capstone: A cubesat pathfinder for the lunar gateway ecosystem. *Small Satellite Conference*, 2021.

[20] C. Giordano and F. Topputo. Analysis, design, and optimization of robust trajectories in cislunar environment for limited-capability spacecraft. *The Journal of the Astronautical Sciences*, 70(6):53, 2023.

[21] C. Giordano, C. Buonagura, A. Martinelli, G. Merisio, V. Franzese, and F. Topputo. Trajectory design and analysis of the lumio cubesat. In *AIAA Scitech 2024 Forum*, page 1271, 2024.

[22] G. Gomez, A. Jorba, J. Masdemont, and C. Simó. A dynamical systems approach for the analysis of the soho mission. *ESA, Spacecraft Flight Dynamics (SEE N 92-24719 15-12)*, pages 449–454, 1991.

[23] G. Gómez, J. Llibre, R. Martínez, and C. Simó. *Dynamics and Mission Design*

Near Libration Points-Vol I: Fundamentals: The Case of Collinear Libration Points, volume 2. World Scientific, 2001.

[24] K. C. Howell and H. J. Pernicka. Numerical determination of lissajous trajectories in the restricted three-body problem. *Celestial mechanics*, 41(1-4):107–124, 1987.

[25] K. C. Howell, B. T. Barden, and M. W. Lo. Application of dynamical systems theory to trajectory design for a libration point mission. *The Journal of the Astronautical Sciences*, 45(2):161–178, 1997.

[26] L. Kaufman and P. J. Rousseeuw. *Finding groups in data: an introduction to cluster analysis*. John Wiley & Sons, 2009.

[27] M. W. Makemson. Determination of selenographic positions. *The moon*, 2(3):293–308, 1971.

[28] K. Oshima. Regularizing fuel-optimal multi-impulse trajectories. *Astrodynamics*, 8 (1):97–119, 2024.

[29] G. D. Racca and P. W. McNamara. The lisa pathfinder mission: Tracing einstein's geodesics in space. *Space science reviews*, 151(1):159–181, 2010.

[30] D. L. Richardson. Analytic construction of periodic orbits about the collinear points. *Celestial mechanics*, 22(3):241–253, 1980.

[31] V. Szebehely. *Theory of Orbits-The Restricted Problem of Three Bodies*. Accademic Press, 1967.

[32] F. Topputo. Fast numerical approximation of invariant manifolds in the circular restricted three-body problem. *Communications in Nonlinear Science and Numerical Simulation*, 32:89–98, 2016.

[33] D. A. Vallado. *Fundamentals of astrodynamics and applications*, volume 12. Springer Science & Business Media, 2001.

[34] E. Veruari. Space trajectory optimisation in high fidelity models. Master's thesis, Politecnico di Milano, 2015.

[35] A. Zanzottera, G. Mingotti, R. Castelli, and M. Dellnitz. Intersecting invariant manifolds in spatial restricted three-body problems: design and optimization of earth-to-halo transfers in the sun–earth–moon scenario. *Communications in Nonlinear Science and Numerical Simulation*, 17(2):832–843, 2012.

A | Appendix A

In this appendix the analytical derivatives of the constraint of the NLP problem introduced in Section 4.2.2 are reported. To make the notation easier, the superscript related to a specific arc is dropped in the continuity constraints $\boldsymbol{\zeta}_k^{(j)}$. These derivatives determine a repetitive structure, which can be exploited in algorithmic loops.

$$\frac{\partial \boldsymbol{\zeta}_k}{\partial \mathbf{x}_k} = \Phi(\mathbf{x}_k, \tau_k; \tau_{k+1}) \quad \text{and} \quad \frac{\partial \boldsymbol{\zeta}_k}{\partial \mathbf{x}_{k+1}} = -I_{6x6} \qquad \text{for} \quad k = 1, ..., m-1 \tag{A.1}$$

where Φ is the State Transition Matrix (STM) computed by solving the variational equations. The partial derivative with respect to the initial and final times of each segment are expressed as:

$$\frac{\partial \boldsymbol{\zeta}_k}{\partial \tau_1} = -\frac{m-k}{m-1}\Phi(\mathbf{x}_k, \tau_k; \tau_{k+1})\boldsymbol{f}(\mathbf{x}_k, \tau_k) + \frac{m-k-1}{m-1}\boldsymbol{f}(\varphi(\mathbf{x}_k, \tau_k; \tau_{k+1}), \tau_{k+1}) \tag{A.2}$$

$$\frac{\partial \boldsymbol{\zeta}_k}{\partial \tau_m} = -\frac{k+1}{m-1}\Phi(\mathbf{x}_k, \tau_k; \tau_{k+1})\boldsymbol{f}(\mathbf{x}_k, \tau_k) + \frac{k}{m-1}\boldsymbol{f}(\varphi(\mathbf{x}_k, \tau_k; \tau_{k+1}), \tau_{k+1}) \tag{A.3}$$

where φ is the flow operator and $\boldsymbol{f}$ correspond to the vector field evaluated according to Eq.(3.7). Additionally, the derivatives on the continuity constraints $(\boldsymbol{\psi_j}, \sigma_j)$ are reported:

$$\frac{\partial \boldsymbol{\psi}_j}{\partial \mathbf{x}_m^{(j)}} = \begin{bmatrix} I_{3x3} & 0_{3x3} \\ 0_{3x3} & 0_{3x3} \end{bmatrix} \qquad \frac{\partial \boldsymbol{\psi}_j}{\partial \mathbf{x}_1^{(j+1)}} = \begin{bmatrix} -I_{3x3} & 0_{3x3} \\ 0_{3x3} & 0_{3x3} \end{bmatrix} \tag{A.4}$$

$$\frac{\partial \sigma_j}{\partial \tau_m^{(j)}} = 1 \qquad \frac{\partial \sigma_j}{\partial \tau_1^{(j+1)}} = -1 \quad \text{for} \quad j = 1, ..., n \tag{A.5}$$

Then, the derivatives of the initial boundary constraint $\boldsymbol{\psi}_0$ are computed:

$$\frac{\partial \boldsymbol{\psi}_0}{\partial \mathbf{x}_1^{(1)}} = \begin{bmatrix} -I_{3x3} & 0_{3x3} \\ 0_{3x3} & 0_{3x3} \end{bmatrix} \tag{A.6}$$

Instead, the partial derivatives involving the initial boundary constraint and the keplerian parameters are omitted for brevity ($\partial\boldsymbol{\psi}_0/\partial\mathbf{y}_{park}$). They are lengthy expressions simply derived applying the chain rule to Eq.(4.9). The same can be said for $\partial\boldsymbol{\psi}_0/\partial t_{park}$.

The derivatives of the final constraint are reported in the following equations:

$$\frac{\partial\boldsymbol{\psi}_f}{\partial\mathbf{x}_m^{(n)}} = I_{6x6} \qquad \frac{\partial\boldsymbol{\psi}_f}{\partial t_{sm}} = -\boldsymbol{f}_{sm} \tag{A.7}$$

where $\boldsymbol{f}_{sm}$ is the vector field in correspondence of the point along the manifold at time t_{sm}, as reported below:

$$\frac{\partial\boldsymbol{\psi}_f}{\partial t_{po}} = -\Phi_{sm}\left[\boldsymbol{f}_{po} - \frac{\varepsilon}{||\Phi_{po}\boldsymbol{\nu}_0||}(I_{6x6} - \boldsymbol{\nu}(t_{po})\boldsymbol{\nu}(t_{po})^T)\right][A\,\Phi_{po}\,\boldsymbol{\nu}_0] \tag{A.8}$$

$$\boldsymbol{f}_{po} = \boldsymbol{f}(\,\varphi(\mathbf{x}_{po,0}, 0; t_{po}),\, t_{po}) \tag{A.9}$$

$$\boldsymbol{f}_{sm} = \boldsymbol{f}(\,\varphi(\mathbf{x}_{sm,0}, 0; t_{sm}),\, t_{sm}) \tag{A.10}$$

$$\Phi_{po} = \Phi(\varphi(\mathbf{x}_{po,0}, 0; t_{po}), 0; t_{po}) \tag{A.11}$$

$$\Phi_{sm} = \Phi(\mathbf{x}_{sm,0}, 0; t_{sm}) \tag{A.12}$$

$$\mathbf{x}_{sm,0} = \varphi(\mathbf{x}_{po,0}, 0; t_{po}) - \varepsilon\,\boldsymbol{\nu}(t_{po}) \tag{A.13}$$

$$\boldsymbol{\nu}(t_{po}) = \frac{\Phi_{po}\boldsymbol{\nu}_0}{||\Phi_{po}\boldsymbol{\nu}_0||} \tag{A.14}$$

where A is the Jacobian of the dynamics computed in Section 3.1.2.

The partial derivative of $\boldsymbol{\Gamma}_0$ with respect to $\mathbf{v}_{park}$ is omitted as in the previews case, since it involves basic geometric transformations. It is sufficient to apply the chain rule to Eq.(4.36) to determine its value.

Lastly, the partial derivatives involving the map of the regularized variables are reported:

$$\frac{\partial\boldsymbol{\Gamma}_i}{\partial\mathbf{x}_m^{(j)}} = \begin{bmatrix} 0_{3x3} & 0_{3x3} \\ 0_{3x3} & -I_{3x3} \end{bmatrix} \qquad \frac{\partial\boldsymbol{\Gamma}_i}{\partial\mathbf{x}_1^{(j+1)}} = \begin{bmatrix} 0_{3x3} & 0_{3x3} \\ 0_{3x3} & I_{3x3} \end{bmatrix} \tag{A.15}$$

$$\frac{\partial\boldsymbol{\Gamma}_i}{\partial\mathbf{U}_j} = \begin{bmatrix} 2u_j & -2w_j & -2s_j \\ 2w_j & 2u_j & 0 \\ 2s_j & 0 & 2u_j \end{bmatrix} \quad \text{or} \quad \frac{\partial\boldsymbol{\Gamma}_i}{\partial\mathbf{U}_j} = \begin{bmatrix} 2w_j & 2u_j & 0 \\ 2u_j & -2w_j & -2s_j \\ 2s_j & 0 & 2u_j \end{bmatrix} \tag{A.16}$$

depending of which of the two formulations presented in Eq.(4.23) and (4.23) is adopted.

B | Appendix B

In this appendix, the derivatives of the NLP formulation presented in Chapter 5 are going to be introduced. Due to the similarities with the previous notation, only the terms that present variations are going to be highlighted for simplicity. Starting with the derivatives of the objective function:

$$\frac{\partial J}{\partial \mathbf{U}_j} = 2\,\omega\,k(\tau_{\text{avg}}^{(j)})\mathbf{U}_j^T \qquad \text{for} \quad j = 1, ..., n-1 \tag{B.1}$$

$$\frac{\partial J}{\partial \mathbf{U}_0} = 2\,\omega\,k({\tau_1}^{(1)})\mathbf{U}_0^T \tag{B.2}$$

$$\frac{\partial J}{\partial \mathbf{U}_{\text{HIM}}} = 2\,\omega\,k({\tau_m}^{(n)})\mathbf{U}_{\text{HIM}}^T \tag{B.3}$$

$$\frac{\partial J}{\partial {\tau_1}^{(j+1)}} = \frac{\partial J}{\partial {\tau_m}^{(j)}} = 0.5\,\dot{k}\left(\tau_{\text{avg}}^{(j)}\right)\|\mathbf{U}_j\|^2 \qquad \text{for} \quad j = 1, ..., n-1 \tag{B.4}$$

$$\frac{\partial J}{\partial {\tau_1}^{(1)}} = \dot{k}({\tau_1}^{(1)})\|\mathbf{U}_0\|^2 \tag{B.5}$$

$$\frac{\partial J}{\partial {\tau_m}^{(n)}} = \dot{k}({\tau_m}^{(n)})\|\mathbf{U}_{\text{HIM}}\|^2 \tag{B.6}$$

$$\text{where} \quad \dot{k} = \frac{(\mathbf{R}_p - \mathbf{R}_s)^T\,(\mathbf{V}_p - \mathbf{V}_s)}{k} \qquad \text{and} \quad \tau_{\text{avg}}^{(j)} = \frac{{\tau_1}^{(j+1)} + {\tau_m}^{(j)}}{2}$$

with the subscript p and s denoting the primary and the secondary of the roto–pulsating frame, respectively Earth and Moon in this thesis. It is worth noting that these position and velocity vectors are reported in capital letters as they are expressed in dimensional units with respect to the SSB J2000 reference frame.

The inequality constraints are a series of linear inequalities, therefore the non–zero derivatives are easily determined as a ± 1 values in correspondence of the involved optimization variables.

The equality constraints instead feature multiple variations which are briefly presented hereafter, starting from the introduction of the continuity constraint within the parking orbit. The following relations are derived in analogy the formulation presented in Appendix B:

$$\frac{\partial \boldsymbol{\zeta}_{park}^{(l)}}{\partial \mathbf{x}_{park}^{(l)}} = \Phi(\mathbf{x}_{park}^{(l)}, \tau_{park}^{(l)}; \tau_{park}^{(l+1)}) , \qquad \frac{\partial \boldsymbol{\zeta}_{park}^{(l)}}{\partial \mathbf{x}_{park}^{(l+1)}} = -I_{6x6} \qquad \text{for} \quad l = 1, ..., m_{park} - 1 \tag{B.7}$$

$$\frac{\partial \boldsymbol{\zeta}_{park}^{(l)}}{\partial \tau_{park}^{(1)}} = -\frac{m_{park} - l}{m_{park} - 1} \Phi(\mathbf{x}_{park}^{(l)}, \tau_{park}^{(l)}; \tau_{park}^{(l+1)}) \boldsymbol{f}(\mathbf{x}_{park}^{(l)}, \tau_{park}^{(l)}) \tag{B.8}$$

$$+ \frac{m_{park} - l - 1}{m_{park} - 1} \boldsymbol{f}(\varphi(\mathbf{x}_{park}^{(l)}, \tau_{park}^{(l)}; \tau_{park}^{(l+1)}), \tau_{park}^{(l+1)}) \tag{B.9}$$

$$\frac{\partial \boldsymbol{\zeta}_{park}^{(l)}}{\partial \tau_{park}^{(m_{park})}} = -\frac{l + 1}{m_{park} - 1} \Phi(\mathbf{x}_{park}^{(l)}, \tau_{park}^{(l)}; \tau_{park}^{(l+1)}) \boldsymbol{f}(\mathbf{x}_{park}^{(l)}, \tau_{park}^{(l)}) \tag{B.10}$$

$$+ \frac{l}{m - 1} \boldsymbol{f}(\varphi(\mathbf{x}_{park}^{(l)}, \tau_{park}^{(l)}; \tau_{park}^{(l+1)}), \tau_{park}^{(l+1)}) \tag{B.11}$$

Instead, the derivatives of the continuity between parking orbit and the first arc of the transfer can be rewritten in the following form, as they do not depend on the keplerian parameters in this formulation:

$$\frac{\partial \boldsymbol{\psi}_0}{\partial \boldsymbol{\rho}_{park}^{(m_{park})}} = \begin{bmatrix} I_{3x3} & 0_{3x3} \\ 0_{3x3} & 0_{3x3} \end{bmatrix} \qquad \frac{\partial \boldsymbol{\psi}_0}{\partial \boldsymbol{\rho}_1^{(1)}} = \begin{bmatrix} -I_{3x3} & 0_{3x3} \\ 0_{3x3} & 0_{3x3} \end{bmatrix} \tag{B.12}$$

Moreover, in the first optimization in the RnBP–RPF the final boundary constraint is still computed as a periodic halo. As a result the derivatives with respect to the time along the halo can be expressed as:

$$\frac{\partial \boldsymbol{\psi}_f}{\partial t_{po}} = -\boldsymbol{f}_{CRTBP}(\, \varphi_{CRTBP}(\mathbf{x}_{po,0}, 0; t_{po}),\, t_{po}) \tag{B.13}$$

where the subscript CRTBP highlights the dynamics involved in the computation and $\boldsymbol{f}_{CRTBP}$ is the vector field in correspondence of the point along the halo at time t_{po}.

In the successive refinement step the quasi–halo is adopted to define the final boundary condition, thus the following partial derivative can be determined:

$$\frac{\partial \boldsymbol{\psi}_f}{\partial \tau_m^{(n)}} = -\boldsymbol{f}(\,\varphi(\mathbf{x}_{QH,0}, \tau_{QH,0}; \tau_m^{(n)}),\, \tau_m^{(n)}) \tag{B.14}$$

where $\tau_{QH,0}$ is the halo injection time determined at the previous optimization step and $\mathbf{x}_{QH,0}$ is the node on the quasi–halo is correspondence of that time coordinate, which is computed with the multiple shooting method introduced in Section 3.2.3.

As in the previous appendix, the partial derivatives of the initial boundary constraint with respect to the orbital parameters ($\partial\boldsymbol{\psi}_{park,0}/\partial\mathbf{y}_{park}$) are omitted for brevity. It is sufficient to develop the chain rule applied to Eq.(5.15) and (5.16). Instead, the partial derivative with respect to the initial time ($\partial\boldsymbol{\psi}_{park,0}/\partial\tau_{park}^{(1)}$) is obtained with finite differences to avoid complicated and lengthy computations.

Lastly, the partial derivatives of the equations mapping the initial and final impulse in the regularized variables are reported, as they present some variations:

$$\frac{\partial \boldsymbol{\Gamma}_0}{\partial \mathbf{x}_{park}^{(m_{park})}} = \begin{bmatrix} 0_{3x3} & 0_{3x3} \\ 0_{3x3} & -I_{3x3} \end{bmatrix} \qquad \frac{\partial \boldsymbol{\Gamma}_0}{\partial \mathbf{x}_1^{(1)}} = \begin{bmatrix} 0_{3x3} & 0_{3x3} \\ 0_{3x3} & I_{3x3} \end{bmatrix} \tag{B.15}$$

$$\frac{\partial \boldsymbol{\Gamma}_{\text{HIM}}}{\partial \mathbf{x}_m^{(n)}} = \begin{bmatrix} 0_{3x3} & 0_{3x3} \\ 0_{3x3} & -I_{3x3} \end{bmatrix} \qquad \frac{\partial \boldsymbol{\Gamma}_{\text{HIM}}}{\partial \mathbf{x}_1^{(1)}} = \begin{bmatrix} 0_{3x3} & 0_{3x3} \\ 0_{3x3} & \boldsymbol{f}_\eta(\mathbf{x}_{QH}) \end{bmatrix} \tag{B.16}$$

where $\boldsymbol{f}_\eta$ is the velocity vector field described by the equations of the RnBP–RPF. These equations are evaluated in correspondence of the halo injection point, which is computed with the flow operator starting from the seed of the halo or quasi–halo depending on the optimization step:

$$\boldsymbol{f}_\eta(\mathbf{x}_{QH}) = \boldsymbol{f}_v^{CRTBP}(\,\varphi_{CRTBP}(\mathbf{x}_{po,0}, 0; t_{po}),\, t_{po}) \tag{B.17}$$

$$\boldsymbol{f}_\eta(\mathbf{x}_{QH}) = \boldsymbol{f}_\eta(\,\varphi(\mathbf{x}_{QH,0}, \tau_{QH,0}; \tau_m^{(n)}),\, \tau_m^{(n)}) \tag{B.18}$$

where 'CRTPB' is introduced to denote the flow and the vector field computed in the Circular Restricted Three Body Problem.

List of Figures

List of Tables

List of Symbols

Variable	**Description**	**SI unit**
a	Semj–Major Axis	m
$\overline{a}$	Primaries Mean Distance	
a_{SRP}	Acceleration caused by the SRP	$m\,s^{-2}$
$\mathbf{a}^*_{SRP}$	Nondimensional Acceleration caused by the SRP	–
$\mathbf{a}_{J_2}$	Acceleration caused by the J_2 term	$m\,s^{-2}$
$\mathbf{a}^*_{J_2}$	Nondimensional Acceleration caused by the J_2 term	–
A	Jacobian of the Dynamics	–
A_z	Out of plane amplitude of the Halo Orbit	m
α	Auxiliary Angle	rad
$\mathbf{b}(\mathrm{t})$	Barycenter of the synodic frame	m
B	Rotation Matrix	–
c	Speed of Light	$m\,s^{-1}$
$\mathbf{c}$	Constraint Vector	–
c_r	Reflective Coefficient	–
$\mathrm{C}(\mathrm{t})$	Rotation Matrix	–
C_j	Jacobi Constant	–
DU	Distance unit	m
$\boldsymbol{\delta}_j$	Nondimensional relative position to the primaries	–
$\boldsymbol{\delta}_m$	Nondimensional relative position to the Moon	–
$\boldsymbol{\delta}_s$	Nondimensional relative position to the Sun	–
Δv	Magnitude of an Impulsive Maneuver	$m\,s^{-1}$
e	Eccentricity	–

$\mathbf{e}_j$	Unit Vectors of the RPF	–
et	Epoch time in seconds past J2000	s
E	Specific Mechanical Energy	$J\,kg^{-1}$
ε	Perturbation	–
$\boldsymbol{\eta}$	Nondimensional velocity of the spacecraft	–
$\boldsymbol{f}$	Right–Hand Side of the Dynamics	–
f	Auxiliary Function	–
φ	Flow of the Equation of Motion	–
Φ	State Transition Matrix	–
$\boldsymbol{\psi}_j$	Position Continuity Constraint	–
$\mathbf{g}$	Equality Constraint Vector	–
G	Gravitational Constant	$m^3\,kg^{-1}\,s^{-2}$
$\mathcal{G}_{eq}$	Jacobian of the Equality Constraints	–
γ_0	Initial Barrier Parameter	–
$\boldsymbol{\Gamma}_j$	Mapping of the Regularized Coordinates	–
$\mathbf{h}$	Inequality Constraint Vector	–
h_a	Height at the Apocenter	m
h_p	Height at the Pericenter	m
i_0	Initial Inclination	rad
I	Identity Matrix	–
J	Objective Function	–
$J_{2,m}$	Moon' Second Order Gravitational Coefficient	–
$k(t)$	Distance between the Primaries	m
$\mathbf{L}_j$	Position of the Lagrangian Points	–
m	Spacecraft Mass	kg
m_j	Mass of the j–th Primary	kg
μ	Mass–Ratio	–
μ_m	Gravitational Parameter of the Earth–Moon System	–
M	Monodromy matrix	–
$\hat{\mu}_j$	Modified Gravitational Parameter	–
$\boldsymbol{\nu}$	Eigenvector of the Monodromy Matrix	–

$\boldsymbol{\omega}$	Angular Velocity of the Primaries	$-$
ω_0	Initial Argument of Pericenter	rad
Ω	Pseudo–Potential	$-$
Ω_0	Initial Right Ascension of the Ascending Node	rad
$\mathbf{P}_j$	Position the j–th primary	m
Ψ_0	Reference Radiation Pressure	$N\,m^{-2}$
q_j	Auxiliary function	$-$
$\mathbf{r}$	Nondimensional Position of the Spacecraft	m
$\mathbf{r}_a$	Apocenter Radius	m
$\mathbf{r}_j$	Nondimensional Position of j–th Body	$-$
$\mathbf{r}_p$	Pericenter Radius	m
$\mathbf{r}^*$	Nondimesional Position in the planetocentric–RnBP	$-$
$\mathbf{r}_{PA}$	Position in the Moon_PA reference frame	m
$\mathbf{r}^*_{PA}$	Nondimensional Position in the Moon_PA frame	$-$
$\mathbf{R}$	Position in the SSB–J2000	m
$\mathbf{R}_j$	Position of the j–th body	m
$\mathbf{R}_m$	Position of the Moon in the SSB–J2000	m
$\mathbf{R}_s$	Position of the Sun in the SSB–J2000	m
$\mathrm{R}_{B,m}$	Moon Equatorial Radius	m
$R_{J2000\rightarrow Moon\_PA}$	Rotation from J2000 to Moon_PA frame	$-$
$\boldsymbol{\rho}$	Nondimensional position of the spacecraft	$-$
$\mathbf{s}_k$	Node on the Quasi–Halo	$-$
S	Skew Matrix	$-$
σ_j	Time Continuity Constraint	$-$
t_e	Time spent in Eclipse	s
t_p	Time spent in Penumbra	s
t_{po}	Time along a Periodic Orbit	$-$
t_{sm}	Time along a Stable Manifold	$-$
T	Halo Orbit Period	$-$
T_2	Rotation Matrix	$-$
TU	Time unit	s

τ	Nondimensional time	$-$
θ_0	Initial True Anomaly	rad
$\mathbf{U}_j$	Regularized Variables	$-$
V	Gravitational Potential	$-$
$\mathbf{V}$	Velocity in the SSB–J2000	ms^{-1}
$\mathbf{V}_j$	Velocity of the j–th body in the SSB–J2000	ms^{-1}
VU	Velocity unit	$m\,s^{-1}$
$\mathbf{x}_s$	Point on the Stable Manifold	$-$
$\mathbf{x}_u$	Point on the Unstable Manifold	$-$
$\mathbf{y}$	Optimization Vector	$-$
$\boldsymbol{\zeta}_j$	Continuity Constraint	$-$

Ringraziamenti

Vorrei ringraziare il mio relatore, il Professor Topputo, per avere accolto le mie preferenze nella scelta del soggetto della tesi e per avermi supportato durante il suo sviluppo. Vorrei ringraziare anche i miei correlatori, Carmine ed Alessandro, per la loro disponibilità nel chiarire eventuali dubbi e per i preziosi consigli offerti.

Ringrazio la mia famiglia per essermi stata vicina anche nei momenti più duri in cui la fatica del percorso è stata compresa e condivisa. Sono grato ai miei genitori, Marcello e Cristina, per avermi trasmesso valori autentici e per avermi dato l'opportunità di inseguire un sogno con incondizionato sostegno e affetto. In particolare, vorrei ringraziare mia mamma per essere sempre stata un punto di riferimento e per avermi insegnato con l'esempio il valore della resilienza nei momenti più difficili.

Un particolare grazie a mia sorella Matilde che mi ha supportato e sopportato in questo percorso. Durante questo periodo che mi ha allontanato da casa ti ho vista crescere e maturare in una persona forte e determinata. Ti auguro di inseguire i tuoi sogni e di affrontare la nuova avventura universitaria con uno sguardo volto all'obiettivo, senza però dimenticare di vivere appieno il percorso.

Ringrazio i miei cari amici Matteo, Lorenzo, Anna e Luca per essere stati presenti in questi anni in cui l'università ci ha portato in città diverse senza però allontanarci. Siete per me una seconda famiglia acquisita. Ogni volta che passo del tempo insieme a voi il mondo frentico in cui siamo immersi sembra fermarsi, riprendere colore e significato. Mi date la possibilità di essere me stesso senza la paura di essere giudicato e la sensazione che nessun argomento sia troppo difficile da affrontare apertamente.

Vorrei ringraziare anche i miei compagni di università Pietro, Andrea, Jimmy, Matteo e Marcello, con cui ho condiviso lunghe giornate in aula studio per concludere progetti interminabili. Il percorso è stato lungo, arduo ma arricchito da questi legami umani che lo hanno reso unico e per questo impossibile da dimenticare.

Ringrazio i miei coinquilini che mi hanno sopportato nella quotidianità, con i quali ho condiviso un ambiente sereno e di sostegno reciproco durante questo percorso intenso.

Infine, non potrei dimenticare di ringraziare i miei compagni di PoliSpace con cui ho condiviso l'ultimo anno di questo percorso universitario. Seppur in un tempo limitato si è creato un grande senso di appartenenza e un clima familiare disteso in cui è stato possibile condividere una passione comune per lo spazio, con l'obiettivo collettivo di portare avanti un progetto ambizioso.

Per concludere vorrei ringraziare me stesso per non avere mollato mai, neppure nei momenti in cui tutto sembrava andare per il verso sbagliato e aver reso fiero il me bambino, che aveva sognato un giorno di raggiungere questo traguardo.